Master Thesis

The Effects of Electron Heating on the Magnetorotational Instability in Protoplanetary Disks

Shoji Mori

Okuzumi Laboratory

Department of Earth and Planetary Science

Tokyo Institute of Technology

October 28, 2016

Abstract

To elucidate mysterious planet formation, understanding protoplanetary disks is essential. Especially, turbulence in the disk greatly affects dynamics of solid particles whose size is from sub-micron to kilometers. Magnetorotaional instability (MRI) is thought to be the most plausible mechanism generating the vigorous turbulence. However, although many studies of MRI have addressed the turbulence strength, the strength remains debatable mainly because of the uncertainty of MRI in the low ionization fraction. Thus, the role of MRI in planet formation is still a puzzle.

So far we have investigated the effect of electron heating on protoplanetary disks. The electron heating takes place when the electric field induced by the magnetic turbulence heats up electrons. The heated electrons frequently collide with and stick to dust grains, which in turn decreases the ionization fraction. MRI is stabilized under the sufficiently low ionization faction, which indicates high resistivity. Our previous work showed that the electron heating might quench the magnetic turbulence in extensive regions. However, how much the electron heating suppresses the turbulence is unknown.

To answer the question, we first numerically investigate the effect of electron heating on the nonlinear evolution of MRI. We perform magnetohydrodynamical simulations including increase of resistivity by electron heating. We introduce a simple analytic resistivity model that enables us to treat the increasing resistivity.

Our simulations confirm the electron heating suppresses magnetic turbulence. We find a clear relation between magnetic turbulence strength and its current density. This relation means that a lower current leads to lower turbulence strength.. We find that when turbulence completely dies away, laminar accretion flow is caused by ordered magnetic field. By solving the dispersion relation, we find an analytical expression of the laminar state that exactly gives the physical quantities. Based on the simulation results and the scaling relation between the accretion stress and current density, we obtain a formula that successfully predicts the accretion stress in the presence of electron heating once current density is given. In a protoplanetary disk, the current density can be estimated by using the current-dependent resistivity and the saturated resistivity. Thus, we can predict the accretion stress in extensive regions where the electron heating occur. This helps us to construct realistic planet formation theory.

The simulations presented in this thesis are based on the simple resistivity model. In future work, we will employ the more realistic resistivity model.

Contents

Chapter 1

Introduction

Many exoplanets have been discovered since Mayor & Queloz have discovered the first exoplanet. At October 28, 2016, 2049 exoplanets including candidates have been found (`http://exoplanet.eu`). As exoplanets had been discovered, the diversity of exoplanets was revealed. The first exoplanet is a typical jupiter-like planet. However, the discovery was surprised because the planet is much closer to the central star than researchers had expected, and thus such planets are called a hot jupiter. In addition, hot Neptune, a neptune-like planet orbiting close to the central star, and a super earth, which consists mainly of rock but has too larger mass than the Earth, were discovered.

Although many exoplanets have been discovered, how the diversity of exoplanets originates is vague. In order to understand the diversity, the process of planet formation have to be revealed. Planets forms in protoplanetary disks consisting of gas and dust. The outline of dust coagulation model of classical planet formation theory is the following. First of all interstellar molecular cloud collapses with own self-gravity in the star formation region, and then a protester and a disk surrounding the star are formed. In the disk, the dust particles grow via collisions and sticking. The micron sized dust particles grow up into planetesimals of which size is approximately 1 km. After the disk disperses owing to accretion into the central star, a system of the protoplanet become unstable, and then their orbit cross. Via the impacts between protoplanets, they become rocky planets. When mass of protoplanets excesses a critical mass, gas in the disk accrete into the protoplanet, and then the gas planet is formed.

However, the classical scenario has serious difficulties in the formation of planetesimals from dust particles. One of the dificulties is the "meter size barrier". When dust particles aerodynamically coupling with the gas grows into meter size rocks, the dust particles feel a headwind and drift radially inward because of the gas drag. The infall time scale is the order of 10^2 years (Adachi et al., 1976; Weidenschilling, 1977). Thus, the most solid particles fall into the central star before they grow up into planetesimals. Moreover, the turbulence in the disk significantly hinders also the growth of meter size rocks. The disk turbulence excites the relative velocity of dust particles. Although the increase of collisional frequency leads to the rapid growth under the perfect sticking, but when the collisional speed is higher than several cm/s, the silicate solid particles bounce or disrupt (Blum & Wurm, 2008; Zsom et al., 2010).

The other classical planet formation scenario using gravitational instability is recognized as a way to avoid the meter size barrier (Safronov, 1969; Goldreich & Ward, 1973). If the disk turbulence absent, the dust particles settles on the midplane and forms a dust layer. When dust density sufficiently increases, the self-gravitational instability of the dust layer occurs, and eventually planetesimals forms. However, dust layers do not form in the turbulent because the disk turbulence stir up the dust layer (Weidenschilling & Cuzzi, 1993). Thus, from the dust coagulation model, in order to build a successful planet formation model, the disk turbulence should be more specified.

Magnetorotational instability (MRI; Balbus & Hawley, 1991), which is an instability between magnetic fields and ionized gas, is thought to be a most plausible mechanism of generating the disk turbulence. If the MRI grows, the vigorous magnetic turbulence is generated with complex magnetic fields (e.g., Hawley et al., 1995). The magnetic fields lead to Maxwell stress, an accretion stress which is caused by the magnetic tension. Maxwell stress of vigorous MRI turbulence provides an effective disk viscosity that allows the disk lifetime consistent with disk observations (Hawley et al., 1995; Fromang & Nelson, 2006; Simon et al., 2009; Flock et al., 2011). In the fully developed MRI turbulence, the kinetic energy of the turbulence is also enough high to prevent dust settling (Carballido et al., 2005) and disrupt particles by collisions (Carballido et al., 2010).

Since MRI turbulence greatly affects both the disk evolution and planet formation, the MRI has been studied long time, but the role of MRI in protoplanetary disks is still not obvious. The awkward problem is that MRI closely links to the ionization fraction of the disk. Since thermal ionization is relevant only close to the central star (Umebayashi, 1983), the dominant part of the disks is ionized only by high-energy sources such as stellar X-rays (Glassgold et al., 1997) and galactic cosmic rays (Umebayashi & Nakano, 1981). Deep inside the disks, the ionization fraction is significantly low because these ionizing radiations are attenuated and because recombination proceeds fast. The low ionization fraction gives rise to fast Ohmic dissipation that stabilizes the MRI (Sano & Miyama, 1999). Such a region is called the “dead zone” (Gammie, 1996; Sano et al., 2000). The MRI is also suppressed by ambipolar diffusion near the surface of the disks (Desch, 2004; Bai & Stone, 2011; Dzyurkevich et al., 2013). The Hall effect can either stabilize or destabilize the MRI depending on the orientation of the magnetic field relative to the disk rotation axis (Wardle, 1999; Wardle & Salmeron, 2012; Bai, 2014). Thus, activity of MRI in the disks is closely linked to ionization fraction and its distribution.

All the previous studies of MRI had neglected the ionization process caused by MRI itself until Inutsuka & Sano (2005) investigated the possibility of ionization by electric field in MRI turbulence with a simple estimation. They found heating of electron by electric fields in MRI turbulence, which is called the “electron heating” and focused in our work. The heating mechanism is the following. The vigorous MRI turbulence generates strong electric fields associated with the growth of magnetic fields. Plasma particles are accelerated by the strong electric fields and are scattered isotropically by collisions with neutral gas particles, leading to increase of their thermal velocity. In particular, electrons are more easily heated compared to ions because light particles are easily scattered. Therefore, the sufficiently developed electric fields of MRI turbulence increase electron temperature in a weakly ionized gas. The heated electrons can become sufficiently high temperature for collisional ionization, which is known as a phenomenon of electron discharge. If this process works, MRI turbulence sustains (Muranushi et al., 2012).

However, the estimation does not consider balance between ionization and recombination. Okuzumi & Inutsuka (2015, henceforth OI15) investigated ionization balance varying electric field strength. They found reduction of ionization fraction by heated electrons sticking to dust grains before the collisional ionization occurs. The heated electrons frequently collide with and stick to dust grains. As a result, the electron heating decreases the ionization fraction. They also suggested that a region where MRI is suppressed enlarges in the dusty disk.

Our previous work (Mori & Okuzumi, 2016, henceforce MO16) investigated where the electron heating takes place and, moreover, might suppress MRI. We found the electron heating occurs in large regions of protoplanetary disks, which is called "e-heating zone." Especially, because the region locates outside the dead zones, electron heating would effectively enlarge dead zones. In addition, we estimated the strength of magnetic turbulence in e-heating zones with a simple scaling relation between the Maxwell stress and current density. In e-heating zone, the current density was suggested to be much less than that in fully developed MRI turbulence. Thus, the previous concluded that electron heating would suppress the MRI turbulence. However, the existence of the scaling relation is not clear because many previous studies have not focused the relation of current density to the Maxwell stress. Moreover, the estimation has assumed a current density where MRI is saturated. Thus, actually, the possibility of suppressing MRI by electron heating has been debatable.

In this work, we first investigate the effect of electron heating on the nonlinear evolution of MRI using local three-dimensional MHD simulations. The goal in this work is to show the clear relation between the Maxwell stress and current density and, moreover, to demonstrate the potential of electron heating to greatly suppress MRI . We introduce a resistivity model in which resistivity increases with electric field strength in order to mimic the realistic resistivity of electron heating. If the stress-current relation exists, it appears by varying parameters of current density which begin to cause electron heating to show the relation.

We denote the following contents with the following order. In Section 2, we present some fundamental background. The mechanism of MRI and electron heating is included there. In Section 3, we present our previous study investigating e-heating zone. The study also describes the implication for dust dynamics. In Section 4, we experimentally investigate the effect of electron heating on the magnetic turbulence by performing MHD simulations including the increase of resistivity. Finally, in Section 5, we present the summary and conclusion. We also present the future work. In this work, we do not use consistent notation occasionally. Thus, we define every variables in each chapter for clarity.

Chapter 2

Background

2.1 Magnetohydrodynamics (MHD) and Magnetorotaional Instability (MRI)

In this section, we briefly denote the fundamentals of magnetohydrodynamics (MHD) and magnetorotational instability (MRI), with referring to Chen (1977) and Johansen (2009). Magnetorotational instability (MRI) is an instability which takes place in differentially rotating ionized disk. MRI is the most plausible mechanism of driving mass accretion by turbulent viscosity in protoplanetary disks. MRI, which is first discovered in the context of general accretion disks by Velikhov (1959), is rediscovered in the context of protoplanetary disks by Balbus & Hawley (1991).

2.1.1 Ideal MHD

MHD deals with a motion of ionized gas holding a magnetic field, by solving the equations of both the fluid and field. In magnetic fields, neutral gas particles receives a force via collisions with ionized particles which receives the Lorentz force from the fields. Conversely, magnetic fields is affected by the motion of ionized gas as contribution of the current density. An electric conductivity, which is an important physical quantity in MHD, express the ease with which electric current flows thorough a medium. MHD based on a limit that the electric conductivity reaches to infinity is called "ideal MHD".

In this subsection, we describe in the ideal MHD for first understanding of MRI. In this pager, we consistently adopt the Gaussian-cgs units and write magnetic flux density as magnetic fields.

Fundamental Equations

In protoplanetary disks, contribution of molecular viscosity is much less than of induction and thereby is negligible [1]. It allows us to use the Euler equation, which neglects the viscosity term in the Navier-Stokes equation, to express the motion of equation of fluid. In MHD, the fluid receives a force from an electromagnetic field in addition to gravity and pressure-gradient force. The electromagnetic force in an electric field E and a magnetic field B per unit volume is generally written as

$$F_{\mathrm{E.M.}} = \rho_e \boldsymbol{E} + \frac{1}{c} \boldsymbol{J} \times \boldsymbol{B}, \tag{2.3}$$

where c is light speed, $\rho_e \equiv \sum_\alpha q_\alpha n_\alpha$ is electric charge density, and $\boldsymbol{J} \equiv q_\alpha n_\alpha \boldsymbol{u}_\alpha$ is current density. Under the first MHD approximation, which holds in an electrically neutral state , the first term is neglected. Thus, we have a equation of motion of MHD fluid,

$$\frac{\partial \boldsymbol{u}}{\partial t} + (\boldsymbol{u} \cdot \nabla)\boldsymbol{u} = -\frac{1}{\rho}\nabla P - \frac{GM_*}{r^2}\boldsymbol{e}_R + \frac{1}{\rho c}(\boldsymbol{J} \times \boldsymbol{B}) \tag{2.4}$$

where $\boldsymbol{u}$ is the fluid velocity, P is the gas pressure, $\boldsymbol{e}_R$ is the radial unit vector of cylindrical coordinate system.

---

[1]A ratio of the advection term to the diffusion term of molecular viscosity is approximately written as

$$\frac{(v \cdot \nabla)v}{\nu_{\mathrm{mol}} \Delta v} \approx \frac{Lv}{\nu_{\mathrm{mol}}} = \mathrm{Re}, \tag{2.1}$$

where ν_{mol}, v, and L are , respectively, the molecular viscosity, fluid velocity, and scale length. The value is called Reynolds number Re. To estimate the typical value, we take $\nu_{\mathrm{mol}} = c_{\mathrm{s}}/n_n \sigma_{nn}$, $L = H$, and $v = c_{\mathrm{s}}$, and then

$$\mathrm{Re} = \frac{c_{\mathrm{s}} n_n \sigma_{nn}}{\Omega} = 10^{12} \left(\frac{T}{280\,\mathrm{K}}\right)^{-1/2} \left(\frac{n_n}{10^{15}\,\mathrm{cm}^{-3}}\right) \left(\frac{r}{1\,\mathrm{AU}}\right)^{-3/2} \tag{2.2}$$

where we take $\sigma_{nn} = 10^{-15}\,\mathrm{cm}^2$. That's why the typical value in protoplanetary disks is much larger than unity and thereby viscosity term can be neglected.

The equation of continuity is written as

$$\frac{\partial \rho}{\partial t} + (\boldsymbol{u} \cdot \nabla)\rho = -\rho \ \nabla \cdot \boldsymbol{u}. \tag{2.5}$$

Assuming the isothermal change, we express the equation of state as,

$$P = c_{\mathrm{s}}^2 \rho. \tag{2.6}$$

In the MHD equations, the evolution equation of a magnetic field, the induction equation, should be solved. The Maxwell-Faraday equation is

$$\frac{\partial \boldsymbol{B}}{\partial t} = -c\nabla \times \boldsymbol{E}, \tag{2.7}$$

which express the time evolution of magnetic fields. The relation between an electric field and current density, which is called "the Ohm's law", in a comoving frame (which moves with fluid) is written as

$$\boldsymbol{J}' = \sigma_c \boldsymbol{E}' \tag{2.8}$$

where we express an electric conductivity as σ_c and values in the comoving frame with the superscript " ′ " only in this section. Under the Lorentz transformation in $u \ll c$, $\boldsymbol{E}'$ and $\boldsymbol{J}'$ are related with $\boldsymbol{E}$ and $\boldsymbol{J}$ as

$$\boldsymbol{E}' = \boldsymbol{E} + \frac{1}{c}\boldsymbol{u} \times \boldsymbol{B}, \tag{2.9}$$

$$\boldsymbol{J}' = \boldsymbol{J}. \tag{2.10}$$

Using Equations (2.7), (2.8), (2.9), and (2.10), we obtain

$$\frac{\partial \boldsymbol{B}}{\partial t} \quad = \quad -c\nabla \times \left(\frac{\boldsymbol{J}}{\sigma_c} - \frac{1}{c}\boldsymbol{u} \times \boldsymbol{B} \right). \tag{2.11}$$

Under the ideal MHD approximation which means $\sigma_c \to \infty$, we obtain the induction equation in ideal MHD,

$$\frac{\partial \boldsymbol{B}}{\partial t} = \nabla \times (\boldsymbol{u} \times \boldsymbol{B}). \tag{2.12}$$

Maxwell equations except for the Faraday's equation include Gauss' equation, equation of conservation of magnetic flux, and Maxwell-Ampére equation, respectively,

$$\boldsymbol{\nabla} \cdot \boldsymbol{E} = 4\pi\rho_e, \tag{2.13}$$

$$\boldsymbol{\nabla} \cdot \boldsymbol{B} = 0, \tag{2.14}$$

$$4\pi\boldsymbol{J} + \frac{\partial \boldsymbol{E}}{\partial t} = c\nabla \times \boldsymbol{B}. \tag{2.15}$$

Under the second MHD approximation, which holds when variation of electric fields is small, the displacement current term is dropped, and then we obtain the Ampére's equation,

$$4\pi\boldsymbol{J} = c\nabla \times \boldsymbol{B} \tag{2.16}$$

Usually, when the fluid velocity is much less than the speed of light [2] , the approximation is justified.

The force in Euler's equation 2.4 is transformed, using Ampére 's equation (2.16), into

$$\begin{aligned} \frac{1}{c}\boldsymbol{J} \times \boldsymbol{B} &= \frac{1}{4\pi}\left((\nabla \times \boldsymbol{B}) \times \boldsymbol{B}\right), & (2.19)\\ &= \frac{1}{4\pi}\left(\boldsymbol{B} \cdot \nabla\right)\boldsymbol{B} - \nabla\left(\frac{B^2}{8\pi}\right), & (2.20) \end{aligned}$$

where the first term is called the magnetic tension while the second is called the magnetic pressure. The importance of the magnetic force [3] represents a non dimensional number, plasma beta which is defined by the ratio of gas pressure to magnetic pressure as

$$\beta = \frac{8\pi P}{B^2}. \tag{2.21}$$

[2] Let us derive the approximation condition from comparing two terms. The condition is approximately written as

$$\frac{E}{T} \ll c\frac{B}{L}. \tag{2.17}$$

Using approximated Maxwell-Faraday Equation (2.7), $B/T = cE/L$, the equation can be translated into

$$\frac{L^2}{T^2} \ll c^2. \tag{2.18}$$

That's why when the representative-velocity scale, which is fluid velocity in many cases of MHD, is much less than light speed, we can neglect the term.

[3] Strictly speaking, the value expresses the unimportance of the magnetic force.

The transformation leads to the equation of motion of MHD,

$$\frac{\partial \boldsymbol{u}}{\partial t} + (\boldsymbol{u}\cdot\nabla)\boldsymbol{u} = -\frac{1}{\rho}\nabla P - \frac{GM_*}{r^2}\boldsymbol{e}_R + \frac{1}{4\pi\rho}\left(\boldsymbol{B}\cdot\nabla\right)\boldsymbol{B} - \frac{1}{\rho}\nabla\left(\frac{B^2}{8\pi}\right) \tag{2.22}$$

In summary, the system of equation of MHD consists of Equations (2.4), (2.5), (2.6), (2.12), and (2.16). This system does not explicitly include the electric fields E because the infinite current streams because of the infinite conductivity and then the fields disappeares.

Ohm's Law

Here we denote the electric conductivity σ_c in Ohm's law (2.8). In this work, we derive the Ohm's law in the comoving frame, but note that it is not necessarily and some books or papers is written in the rest frame. The reason that we adopt the comoving frame is to simply derive the nonlinear Ohm's law which we will denote in Section 2.2.

In the comoving frame, the current density is expressed from the definition,

$$\boldsymbol{J}' \equiv \sum_\alpha q_\alpha n_\alpha \left\langle \boldsymbol{v}_\alpha \right\rangle', \tag{2.23}$$

where $\langle \boldsymbol{v}_\alpha \rangle'$ is the mean velocity of α-particles. $\langle \boldsymbol{v}_\alpha \rangle'$ is derived by the kinetics as follows. When the charged particles having mass m_α and charge q_α receive the electric force in the electric field E' and then accelerate into $\langle \boldsymbol{v}_\alpha \rangle'$ during mean collisional time Δt_α, using the approximated equation of motion $m_\alpha \langle \boldsymbol{v}_\alpha \rangle' / \Delta t_\alpha = q_\alpha \boldsymbol{E}'$,the velocity is expressed as

$$\langle \boldsymbol{v}_\alpha \rangle' = \frac{q_\alpha \boldsymbol{E}' \Delta t_\alpha}{m_\alpha}. \tag{2.24}$$

Substitution for $\langle \boldsymbol{v}_\alpha \rangle'$ into Equation (2.23) leads to

$$\boldsymbol{J}' = \left(\sum_\alpha \frac{q_\alpha^2 n_\alpha \Delta t_\alpha}{m_\alpha}\right)\boldsymbol{E}' = \sigma_c \boldsymbol{E}'. \tag{2.25}$$

The equation in the parenthesis is the electric conductivity σ_c. As is evident from the equation, σ_c is proportional to $n_\alpha \Delta t_\alpha$ $(= n_\alpha/(n_n \langle \sigma_{\alpha n} v_{\alpha n}\rangle))$. Therefore, we can say that the ideal MHD approximation means the limit of the ionization fraction n_α/n_n.

σ_c is commonly treated as constant, but, strictly speaking, that is just assumption. Okuzumi & Inutsuka (2015) get rid of the assumption and focus that the ionization balance can be changed when electric fields are strong. The more detail is described in Section 2.2.

Alfvén Velocity

Here we denote the Alfvén velocity which is the propagation speed of a magnetic field displacement. Let us consider the propagation of the displacement $\boldsymbol{B}_1$ in the uniform magnetic field $\boldsymbol{B}_0(= B_0\boldsymbol{e}_z)$ with zero initial velocity ($\boldsymbol{u}_0 = 0$). Moreover, for simplicity, we assume constant density, which leads to no pressure gradient($\nabla P = 0$) and incompressible fluid($\nabla \cdot \boldsymbol{u} = 0$), and $\boldsymbol{B}_1$ to be perpendicular to $\boldsymbol{B}_0$, $\boldsymbol{B}_1 = B_{1x}\boldsymbol{e}_x + B_{1y}\boldsymbol{e}_y$. The equation of motion can be written as

$$\begin{aligned} \frac{\partial \boldsymbol{u}_1}{\partial t} &= -\frac{1}{4\pi\rho}\left(\boldsymbol{B}_0 \times (\nabla \times \boldsymbol{B}_1)\right), \\ &= \frac{1}{4\pi\rho}\left(B_0 \nabla_z \boldsymbol{B}_1\right), \end{aligned} \tag{2.26}$$

which have been derived from Equation (2.19). The induction equation is written as

$$\begin{aligned} \frac{\partial \boldsymbol{B}_1}{\partial t} &= \nabla \times (\boldsymbol{u}_1 \times \boldsymbol{B}_0), \\ &= (\boldsymbol{B}_0 \cdot \nabla)\boldsymbol{u}_1 - \boldsymbol{B}_0(\nabla \cdot \boldsymbol{u}_1), \\ &= B_0 \nabla_z \boldsymbol{u}_1. \end{aligned} \tag{2.27}$$

We then have the wave equation of $\boldsymbol{B}_1$ toward the z-direction,

$$\begin{aligned} \frac{\partial^2 \boldsymbol{B}_1}{\partial t^2} &= B_0 \nabla_z \left(\frac{1}{4\pi\rho} B_0 \nabla_z \boldsymbol{B}_1\right), \\ &= \frac{B_0^2}{4\pi\rho}\frac{\partial^2}{\partial z^2}\boldsymbol{B}_1. \end{aligned} \tag{2.28}$$

This equation expresses that the magnetic displacement is propagated with a velocity

$$v_A = \frac{B_0}{\sqrt{4\pi\rho}}, \tag{2.29}$$

which is called "Alfvén velocity."

2.1.2 Linear Stability Analysis of MRI

MRI appears by the linear stability analysis of ideal MHD in differentially rotating disks in magnetic fields.

Let us consider the Kepler disk in the presence of an initially uniform magnetic field in z direction ($\boldsymbol{B}_0 = (0, 0, B_0)$). The angular velocity Ω at a distance r from the central star is expressed as

$$\Omega(r) = \sqrt{\frac{GM_*}{r^3}}. \tag{2.30}$$

In the cylindrical coordinate (r, ϕ, z), the equation of motion is written as

$$\frac{\partial u_r}{\partial t} - \frac{u_\phi^2}{r} + (\boldsymbol{u} \cdot \nabla) u_r = -\frac{1}{\rho}\frac{\partial P}{\partial r} - \frac{GM_*}{r^2}\boldsymbol{e}_r + \frac{1}{\rho c}(\boldsymbol{J} \times \boldsymbol{B})_r, \tag{2.31a}$$

$$\frac{\partial u_\phi}{\partial t} + \frac{u_r u_\phi}{r} + (\boldsymbol{u} \cdot \nabla) u_\phi = -\frac{1}{\rho r}\frac{\partial P}{\partial \phi} + \frac{1}{\rho c}(\boldsymbol{J} \times \boldsymbol{B})_\phi, \tag{2.31b}$$

$$\frac{\partial u_z}{\partial t} + (\boldsymbol{u} \cdot \nabla) u_z = -\frac{1}{\rho}\frac{\partial P}{\partial z} - \frac{GM_*}{r^2}\boldsymbol{e}_z + \frac{1}{\rho c}(\boldsymbol{J} \times \boldsymbol{B})_z. \tag{2.31c}$$

Local Shearing Sheet Approximation

Some proper approximations help to simply derive the linear stability analysis of MRI. Here let us adopt the local coordinate (x, y, z), where x-axis is toward r-axis and y is perpendicular to x. The coordinate rotates with the angular velocity $\Omega_0 = \Omega(r_0)$, where r_0 is the center of the coordinate and much larger than x and y, $r_0 \ll x$ and $r_0 \ll y$. x and y are, respectively, expressed as

$$(x, y) = (r - r_0, r_0(\phi - \Omega_0 t)), \tag{2.32}$$

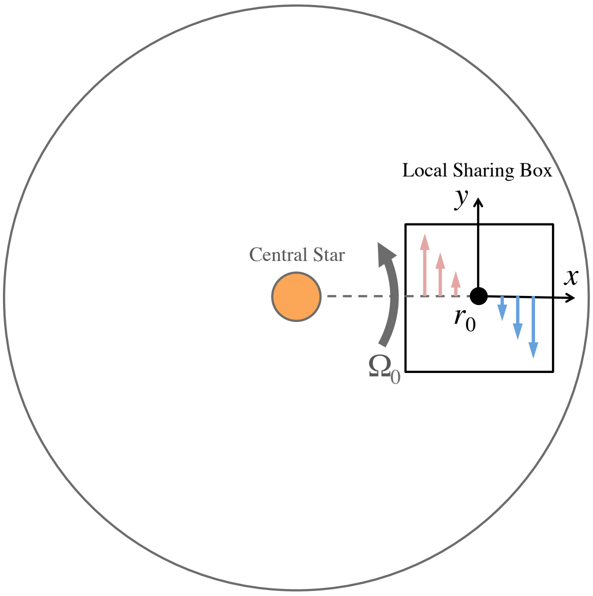

Figure 2.1: Schematic diagram expressing the local sharing coordinate. The origin is located at a distance r_0 from the central star and rotates with an angular velocity $\Omega(r_0)$. In differentially rotating disks, an observer in the coordinate observes a shear flow.

and the velocity in the local coordinate, (u_x, u_y), is related to the one in the cylindrical coordinate, (u_r, u_ϕ), as

$$(u_x, u_y) = (u_r, r_0 (\Omega(r) - \Omega_0)) . \tag{2.33}$$

where $\Omega(r) = \frac{\partial \phi}{\partial t}$. To know the background velocity field (unperturbed velocity) in the local coordinate, we consider the steady flow and then have the velocity field,

$$(u_{x,\mathrm{steady}}, u_{y,\mathrm{steady}}) = \left(0, -\frac{3}{2}\Omega_0 x\right), \tag{2.34}$$

where we use

$$\begin{aligned} \Omega(r_0 + x) - \Omega(r_0) &= \sqrt{\frac{GM_*}{r_0^3}} \left(1 + \frac{x}{r_0}\right)^{-3/2} - \Omega(r_0) \\ &\approx \Omega_0 \left(1 - \frac{3}{2}\frac{x}{r_0}\right) - \Omega(r_0) \\ &\approx -\frac{3}{2}\Omega_0 \frac{x}{r_0}. \end{aligned} \tag{2.35}$$

The tidal force (a centrifugal force − −a gravitational force) in Equation (2.31a) can be written as

$$
\begin{aligned}
\frac{u_\phi^2}{r} - \frac{GM_*}{r^2} &= (r_0 + x)\left(\frac{\partial \phi}{\partial t}\right)^2 - \frac{GM_*}{(r_0+x)^2} \\
&= (r_0 + x)\left(\frac{u_y}{r_0} + \Omega_0\right)^2 - \frac{GM_*}{r_0^2}\left(1 + \frac{x}{r_0}\right)^{-2} \\
&\approx r_0(1 + \frac{x}{r_0})\left(\Omega_0^2 + 2\frac{u_y \Omega_0}{r_0}\right) - r_0 \Omega_0^2 \left(1 - 2\frac{x}{r_0}\right) \\
&\approx 3\Omega_0^2 x + 2u_y \Omega_0,
\end{aligned}
\tag{2.36}
$$

while $\frac{\partial u_\phi}{\partial t}$ can be written as

$$
\begin{aligned}
\frac{\partial u_\phi}{\partial t} &= \frac{\partial}{\partial t}\left(r\left(\frac{u_y}{r_0} + \Omega_0\right)\right) \\
&= \frac{u_x u_y}{r_0} + u_x \Omega_0 + \frac{r}{r_0}\frac{\partial u_y}{\partial t} \\
&\approx u_x \Omega_0 + \frac{\partial u_y}{\partial t}.
\end{aligned}
\tag{2.37}
$$

$u_r u_\phi / r$ can be written as

$$
\begin{aligned}
\frac{u_r u_\phi}{r} &= u_x \left(\frac{u_y}{r_0} + \Omega_0\right) \\
&\approx u_x \Omega_0.
\end{aligned}
\tag{2.38}
$$

For the simplicity of the derivation, we here use the shearing sheet approximation which neglects the vertical velocity and the equation of motion with respect to z direction. In addition, we impose the incompressibility, $\rho = \rho_0$(constant), and isothermality, $c_\mathrm{s} =$ constant, and then also have $P =$ constant. Thus, we obtain the equations to be solved,

$$
\frac{\partial u_x}{\partial t} + (\boldsymbol{u}\cdot\nabla)u_x = 2\Omega_0 u_y + 3\Omega_0^2 x + \frac{1}{\rho c}(\boldsymbol{J}\times\boldsymbol{B})_x, \tag{2.39a}
$$

$$
\frac{\partial u_y}{\partial t} + (\boldsymbol{u}\cdot\nabla)u_y = -2\Omega_0 u_x + \frac{1}{\rho c}(\boldsymbol{J}\times\boldsymbol{B})_y, \tag{2.39b}
$$

$$
\frac{\partial \boldsymbol{B}}{\partial t} + (\boldsymbol{u}\cdot\nabla)\boldsymbol{B} = (\boldsymbol{B}\cdot\nabla)\boldsymbol{u} \quad , \tag{2.39c}
$$

where we use $\nabla \cdot u = 0$.

To investigate the growth of given perturbations, we perform a linear stability analysis. We express values as a sum of the unperturbed value and perturbed value, and then transform the above equations into the ones of the first-order vales. We consider that the unperturbed magnetic field is vertically uniform and the perturbed magnetic field is only perpendicular to z direction. The values are expressed as

$$u_x = u_{x1} \ , \tag{2.40a}$$

$$u_y = -\frac{3}{2}\Omega_0 x + u_{y1} \ , \tag{2.40b}$$

$$B_x = B_{x1} \ , \tag{2.40c}$$

$$B_y = B_{y1} \ , \tag{2.40d}$$

$$B_z = B_0, \tag{2.40e}$$

$$\boldsymbol{J} = \frac{1}{4\pi c}\nabla \times \boldsymbol{B}_1 = \boldsymbol{J}_1 \ . \tag{2.40f}$$

Using these equations and neglecting the second-order values, we obtain

$$\frac{\partial u_{x1}}{\partial t} = 2\Omega_0 u_{y1} + \frac{1}{\rho_0 c}(\boldsymbol{J}_1 \times \boldsymbol{B}_0)_x \tag{2.41a}$$

$$\frac{\partial u_{y1}}{\partial t} - \frac{3}{2}\Omega_0 u_{x1} = -2\Omega_0 u_{x1} + \frac{1}{\rho_0 c}(\boldsymbol{J}_1 \times \boldsymbol{B}_0)_y \tag{2.41b}$$

$$\frac{\partial B_{x1}}{\partial t} = B_0 \frac{\partial u_{x1}}{\partial z} \tag{2.41c}$$

$$\frac{\partial B_{y1}}{\partial t} = B_0 \frac{\partial u_{y1}}{\partial z} + B_{x1}\left(-\frac{3}{2}\Omega_0\right). \tag{2.41d}$$

The Lorentz force can be written as

$$\begin{aligned}
\frac{1}{\rho_0 c}(\boldsymbol{J}' \times \boldsymbol{B}_0) &= \frac{1}{\rho_0 c}\left(\left(\frac{c}{4\pi}\nabla \times \boldsymbol{B}_1\right) \times \boldsymbol{B}_0\right) \\
&= \frac{1}{4\pi\rho_0}\left(\left(\boldsymbol{B}_0 \cdot \nabla\right)\boldsymbol{B}_1 - \nabla\left(\boldsymbol{B}_0 \cdot \boldsymbol{B}_1\right)\right) \\
&= \frac{1}{4\pi\rho_0} B_0 \frac{\partial \boldsymbol{B}_1}{\partial z}.
\end{aligned} \tag{2.42}$$

Thus, we obtain

$$\frac{\partial u_{x1}}{\partial t} = 2\Omega_0 u_{y1} + \frac{B_0}{4\pi\rho_0}\frac{\partial B_{x1}}{\partial z} \tag{2.43a}$$
$$\frac{\partial u_{y1}}{\partial t} = -\frac{1}{2}\Omega_0 u_{x1} + \frac{B_0}{4\pi\rho_0}\frac{\partial B_{y1}}{\partial z} \tag{2.43b}$$
$$\frac{\partial B_{x1}}{\partial t} = B_0\frac{\partial u_{x1}}{\partial z} \tag{2.43c}$$
$$\frac{\partial B_{y1}}{\partial t} = B_0\frac{\partial u_{y1}}{\partial z} - \frac{3}{2}\Omega_0 B_{x1}. \tag{2.43d}$$

Let us investigate an unstable mode in z direction, k_z, by the Fourier analysis. The any given perturbation can be expressed by a superposition of plane waves. We assume an arbitrary perturbed value q_1 to be

$$q_1 \propto \exp\left[i(k_z z - \omega t)\right]. \tag{2.44}$$

Thus, we obtain

$$-i\omega u_{x1} = 2\Omega_0 u_{y1} + ik_z\frac{B_0}{4\pi\rho_0}B_{x1} \tag{2.45a}$$
$$-i\omega u_{y1} = -\frac{1}{2}\Omega_0 u_{x1} + ik_z\frac{B_0}{4\pi\rho_0}B_{y1} \tag{2.45b}$$
$$-i\omega B_{x1} = ik_z B_0 u_{x1} \tag{2.45c}$$
$$-i\omega B_{y1} = ik_z B_0 u_{y1} - \frac{3}{2}\Omega_0 B_{x1}. \tag{2.45d}$$

Thus, by arranging this equations, we obtain the dispersion relation with respect to k_z,

$$\omega^4 - 2\omega^2(2v_A^2k_z^2 + \Omega_0^2) + v_A^2k_z^2(v_A^2k_z^2 - 3\Omega_0^2) = 0. \tag{2.46}$$

Equation (2.46) can be easily solved. Finally, we obtain the solution of the dispersion relation,

$$\frac{\omega_\pm^2}{\Omega_0^2} = \frac{v_A^2k_z^2}{\Omega_0^2} + \frac{1}{2} \pm \sqrt{4\frac{v_A^2k_z^2}{\Omega_0^2} + \frac{1}{4}} \tag{2.47}$$

In Figure 2.2, we plot ω^2 as a function of k_z. Since ω is given in Equation (2.44), the perturbation is unstable when $\omega^2(k_z) < 0$, while the perturbation is stable when

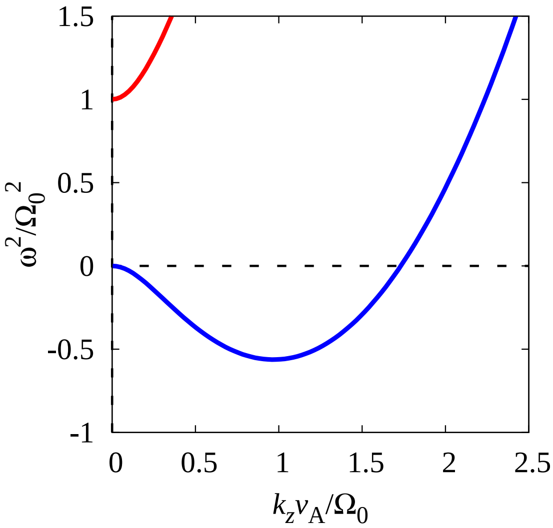

Figure 2.2: Dispersion relation of MRI in ideal MHD. The frequency in the vertical axis is normalized by Ω_0, and the perturbation wavenumber in the horizontal axis is normalized by Ω_0/v_A. Blue line shows ω_-^2/Ω_0^2, and red line ω_+^2/Ω_0^2. When $\omega^2 < 0$, the perturbation is unstable, while when $\omega^2 > 0$, the perturbation is stable and propagate as a MHD wave.

$\omega^2(k_z) > 0$. Thus, the unstable wave number is

$$0 < k_z < \sqrt{3}\Omega_0/v_A, \tag{2.48}$$

where $\sqrt{3}\Omega_0/v_A$ is the largest wavenumber in the wavenumber which trigger MRI. The shortest unstable wavelength $\lambda_{\rm crit}$ which corresponds to the largest unstable wavenumber is

$$\lambda = 2\pi \frac{v_A}{\sqrt{3}\Omega_0}. \tag{2.49}$$

The unstable wavelength in which MRI growth is fastest is the one of $\min(\omega^2)$, and thereby we obtain the most unstable growth rate,

$$\lambda = 2\pi \sqrt{\frac{16}{15}} \frac{v_A}{\Omega_0} \tag{2.50}$$

when the wavelength is the most unstable wavelength,

$$\mathrm{Im}(\omega)_{\rm max} = \frac{3}{4}\Omega_0. \tag{2.51}$$

The timescale of MRI growth is $\sim 1/\Omega_0$. This means that the instability grows during an orbital period, and the growth rate is relatively fast in global effects of protoplanetary disks. Moreover, in ideal MHD, the growth rate does note depend on the vertical magnetic field strength. In other words, MRI would appear even if the initial magnetic fields is very weak. That's why it has been thought that MRI should play an important role in protoplanetary disks.

2.1.3 Nonideal MHD Effects

Ideal MHD approximation assumes infinite conductivity, whereas "nonideal MHD" have finite conductivity.

In nonideal MHD, using Equations (2.16) and (2.14), the induction equation is expressed as

$$\begin{aligned}\frac{\partial \boldsymbol{B}}{\partial t} &= \nabla \times (\boldsymbol{u} \times \boldsymbol{B}) - \frac{c^2}{4\pi\sigma_c}\nabla \times (\nabla \times \boldsymbol{B}) \\ &= \nabla \times (\boldsymbol{u} \times \boldsymbol{B}) - \frac{c^2}{4\pi\sigma_c}(\nabla(\nabla \cdot \boldsymbol{B}) - \nabla^2 \boldsymbol{B}) \\ &= \nabla \times (\boldsymbol{u} \times \boldsymbol{B}) + \eta \nabla^2 \boldsymbol{B}, \end{aligned} \tag{2.52}$$

where η is magnetic resistivity which is related to electric conductivity as

$$\eta = \frac{c^2}{4\pi\sigma_c}. \tag{2.53}$$

The right-hand side first term in Equation (2.52) , which is the same as in ideal MHD, expresses the amplification of magnetic fields by gas motion coupling with the fields. The second term expresses the diffusion of magnetic fields. When the first term is negligible, the equation is expressed as a diffusion equation. Therefore, when η is effective, the magnetic fields grow slowly or decrease. Thus the dissipation of magnetic field by high resistivity or low conductivity is called the ohmic dissipation.

We can obtain a criterion which expresses whether the magnetic field is induced or diffused, by taking a ratio of the induction term in Equation (2.52) to the diffusion term. If we consider partial derivatives to be the most unstable wavenumber Ω/v_A and characteristic velocity to be v_A, we obtain the criterion, which is called the Elsasser number Λ,

$$\Lambda = \frac{|\nabla \times (\boldsymbol{u} \times \boldsymbol{B})|}{\eta \nabla^2 \boldsymbol{B}} \sim \frac{v_A^2}{\eta \Omega}. \tag{2.54}$$

When $\Lambda \gg 1$, the ohmic dissipation is negligible and thereby we can assume ideal MHD. In contrast, when $\Lambda \lesssim 1$, the ohmic dissipation is not negligible and thereby we should consider nonideal MHD.

2.2 Nonlinear Ohm's Law

In this subsection, we summarize the nonlinear Ohm's law in OI15. The nonlinear Ohm's law is a relation between electric field and current density including heating of electron by strong electric field. So far, previous studies assumes that electric conductivity (electric resistivity) does not depend on the electric field strength. However, actually, MRI turbulence generates strong electric field after besides magnetic field growth. Thus, the possibility that the electric field heat up electrons was suggested in Inutsuka & Sano (2005). After that, in weakly ionized gas including dust, Okuzumi & Inutsuka (2015) found that an increase of electron energy leads to increase of electron's dust adsorption rate. Since the reduction rate of electron abundance is increased, the electron abundance is decreased in a gas-phase. Thus, the conductivity depend on the electric field because electric conductivity depends on the ionization fraction. For MRI to grow, the ionization fraction should be sufficiently high (see Section 2.1.3). Thus, because MRI might be suppressed if this effect sufficiently work, this effect will be important.

2.2.1 Outline of Calculation

Here, we present the outline of derivation of the nonlinear Ohm's law. The keys of the nonlinear Ohm's law are heating of electron by electric field and the the ionization balance. In electric fields, electron velocity distribution is changed from the thermal velocity distribution, Maxwell distribution. The change of the velocity distribution leads to change mean drift velocity $\langle \boldsymbol{v}_\alpha \rangle$ and mean energy $\langle \epsilon_\alpha \rangle$ of plasma particles in turn. Because the mean plasma energy is closely related to ionization fraction,

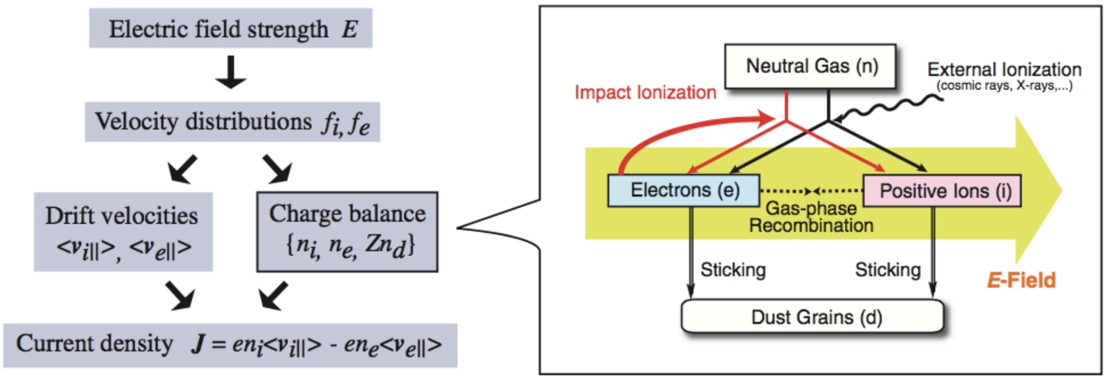

Figure 2.3: Sketch of the derivation procedure and the charge reaction model presented in OI15. The model gives the electric current density $\boldsymbol{J}$ as a function of the electric field strength $\boldsymbol{E}$. The plasma velocity distribution functions f_e and f_i take into account heating by the electric field, and therefore the resulting J is nonlinear in E.

ionization balance is affected and therefore number density of plasma particle n_α is changed. Current density is defined as $\boldsymbol{J} = \sum_{\alpha=e,i} q_\alpha n_\alpha \langle \boldsymbol{v}_\alpha \rangle$, where q is charge and α express a value of plasma particle. Thus, current density including dependence of the conductivity on electric fields can be calculated, and then the relation between electric fields and current density is obtained.

The order of the derivation is as follows:

1. Calculate electron and ion velocity distribution function f_e and f_i.

2. From the velocity distribution, calculate electron and ion mean velocity, $\langle \boldsymbol{v}_e \rangle$ and $\langle \boldsymbol{v}_i \rangle$, and mean energy ,$\langle \epsilon_e \rangle$ and $\langle \epsilon_i \rangle$.

3. Calculate electron and ion number density, n_e and n_i, from ionization balance.

4. Obtain the J–E relation from $J = \sum_\alpha q_\alpha n_\alpha \langle \boldsymbol{v}_\alpha \rangle$.

We show the schematic diagram of the derivation procedure in Figure 2.3. In their paper, they focus also a collisional ionization of electrons by strong electric field besides dust adsorption. However, because our work focus the nonlinearity by dust adsorption of heated electron, we does not treat the collisional ionization here. In addition, because the collisional ionization occurs in $E \sim 10^3 E_{\rm crit}$, the neglecting it is reasonable in $E \lesssim 10^2 E_{\rm crit}$. Actually, as we see Section 3.2 of our work, we confirm the electric fields does not increase so much in a large region of the disk.

2.2.2 Plasma Heating

Here we briefly present a derivation of heating of plasma particles by electric field (plasma heating) in OI15.

A mean velocity $\langle \boldsymbol{v}_\alpha \rangle$ and energy $\langle \epsilon_\alpha \rangle$ of charged particles having a velocity distribution function f_α is expressed as

$$\langle \boldsymbol{v}_\alpha \rangle = \int \boldsymbol{v}_\alpha f_\alpha(\boldsymbol{E}, \boldsymbol{v_\alpha})\ d^3 v_\alpha, \tag{2.55}$$

$$\langle \epsilon_\alpha \rangle = \int \epsilon_\alpha f_\alpha(\boldsymbol{E}, \boldsymbol{v_\alpha})\ d^3 v_\alpha. \tag{2.56}$$

where $\epsilon_\alpha = m_\alpha v_\alpha^2/2$. Using $\langle \epsilon_\alpha \rangle$, the temperature of charged particles is defined as $\langle \epsilon_\alpha \rangle \equiv 3k_{\rm B}T_\alpha/2$ when the random (thermal) energy dominates the kinetic energy. The kinetic energy of electrons exceeds the one of neutral particles when electric field strength exceeds the threshold $E_{\rm crit}$, (Landau & Lifshitz, 1953),

$$E_{\rm crit} = \sqrt{\frac{6m_e}{m_n}} \frac{k_{\rm B}T}{el_e}, \tag{2.57}$$

where m_e and m_i are, respectively, the mass of electron and neutral particles, $k_{\rm B}$ is the Boltzmann constant, T is the neutral gas temperature, e is the elementary charge, and l_e is the mean free path of electron.

The velocity distribution function of electrons depending on electric field strength is derived by Davydov (1935). OI15 used the distribution although here the specific formula is skipped for simplicity. Figure 2.4 shows the E dependent energy distribution of electrons in the case of $E = 0$ and $100E_{\rm crit}$. When $E \approx 0$, the energy distribution is approximately the Maxwell distribution. From $E = 0$ to $100E_{\rm crit}$, the top of the energy distribution which corresponds to $\langle \epsilon_e \rangle$ shifted to the right. Thus, electric field increases the mean kinetic energy. The velocity distribution function of ions f_i are approximately expressed as a Maxwell distribution that is shifted by ion mean drift energy $m_i \langle \boldsymbol{v}_i \rangle^2 /2$ (Hershey, 1939). The drifted velocity can be derived from the kinetics (e.g., see Appendix in OI15).

Figure 2.5 shows the dependence of electron and ion mean energy on electric field

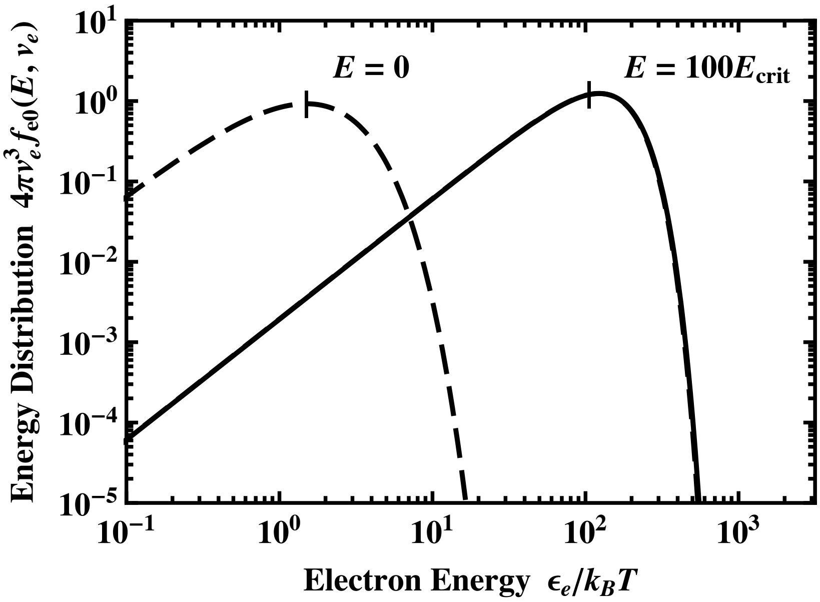

Figure 2.4: Energy distribution of electrons depending on electric field strength in the case of $E = 0$ (dashed line) and $100E_{\rm crit}$ (solid line). The vertical ticks on the distributions indicate $\langle\epsilon_e\rangle$.

strength. When $E \lesssim E_{\rm crit}$, the mean kinetic energy is constant and equal to the neutral gas temperature. When $E > E_{\rm crit}$, the electron mean kinetic energy increases with increase of E. Likewise, when E is larger than $E_{{\rm crit},i}$, an electric field strength which starts to heat ions, the ion kinetic energy increases with increase of E. Thus, strong electric field heat up plasma particles.

The critical $E_{\rm crit}$ and $E_{{\rm crit},i}$ are different by ~ 300. Actually, mean free time of electrons and ions are the same order, because polarization of ion increases the cross section although electrons move faster than ions.

2.2.3 Charge Reactions

Ionization fraction can be obtained by solving the rate equation including ionization and reduction reactions. OI15 consider ionization, recombination, and dust adsorption. In addition, OI15 adopted an analytical method for solving the rate equation presented in Okuzumi et al. (2009). They assume the equilibrium state and the ions represented

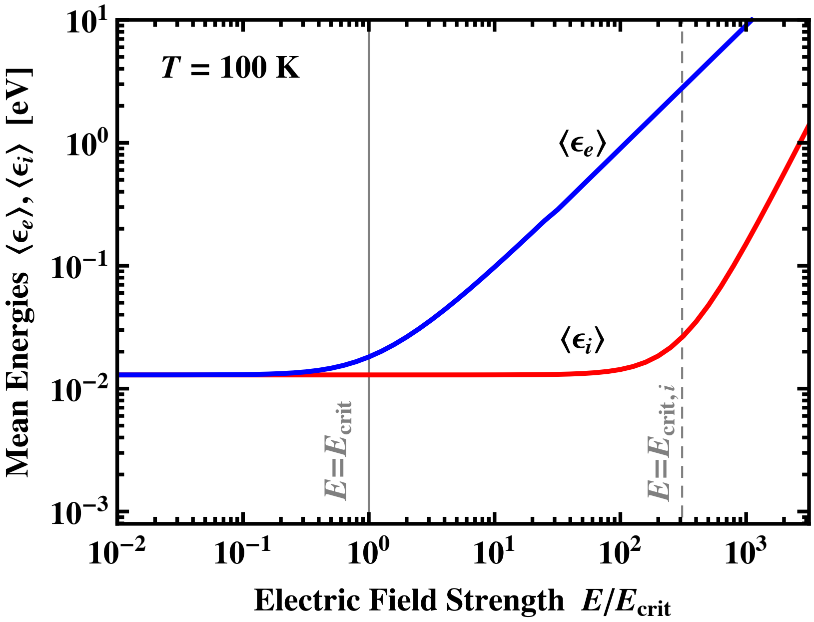

Figure 2.5: Dependence of mean plasma energy on electric field strength. They took here gas temperature to be 100 K. Vertical axis shows mean kinetic energy of electrons (blue) and ions (red), and horizontal axis shows the electric field strength notarized $E_{\rm crit}$. $E_{\rm crit}$ and $E_{{\rm crit},i}$ shows the electric fields where electron and ion heating starts up, respectively.

by a single dominant species. The rate equations to be solved are

$$0 = \zeta n_n - K_{\rm rec} n_i n_e - K_{di} n_d n_i, \tag{2.58a}$$

$$0 = \zeta n_n - K_{\rm rec} n_i n_e - K_{de} n_d n_e, \tag{2.58b}$$

$$0 = Z n_d + n_i - n_e, \tag{2.58c}$$

where n_x (x=n(neutral particles), e(electrons), i(ions), d(dust particles)) is number density of x particle species, ζ is the ionization rate, $K_{d\alpha}$ is the dust adsorption rate of charged particles, $K_{\rm rec}$ is the recombination rate, and Z is the number of charges per a dust grain. Equation (2.58a) and (2.58b) can transform into a quadratic equation. Thus, the analytical solution $n_\alpha^{\rm (eq)}$ is given by

$$n_\alpha^{\rm (eq)} = \frac{\zeta n_n}{K_{d\alpha} n_d} \left(\frac{1}{2} + \sqrt{\frac{1}{4} + \frac{K_{\rm rec} \zeta n_n}{K_{di} K_{de} n_d^2}} \right)^{-1}. \tag{2.59}$$

$Z^{\rm (eq)}$ is given by

$$Z = \frac{1}{n_d} \left(n_e^{\rm (eq)} - n_i^{\rm (eq)} \right). \tag{2.60}$$

Dust adsorption rate $K_{d\alpha}$ is the ensemble averaged volume that passes through collisional cross section in the mean free time. $K_{d\alpha}$ is given by

$$K_{d\alpha} = S_\alpha \int \sigma_{d\alpha}(v_{d\alpha}) v_{d\alpha} f_\alpha(\boldsymbol{v_\alpha}) d^3 v_\alpha \tag{2.61}$$

where the cross section between a dust grain and a charged particle, $\sigma_{d\alpha}(v_{d\alpha}, Z)$, is given by Rutherford scattering (Spitzer, 1941) and S_α is the absorption probability. OI15 assumes $S_\alpha = 1$.

2.2.4 Examples

Figure 2.6 shows the ionization fraction depending on an electric field. In low electric fields, electrons and ions are in equilibrium. This means that gas-phase recombination process controls ionization fraction. While electric field strength exceeds E_{crit}, the electron abundance decreases with increase in electric field. At this time, ions and charges on dust grains are in equilibrium. The ion abundance is controlled by dust adsorption rate, whereas the electron abundance is controlled by collisional frequency to dust grains, i.e. electron temperature. While the electron fast sticks to dust grains, electron abundance is different from ion abundance.

The nonlinear Ohm's law can be derived by the definition of current density, using $\langle \boldsymbol{v}_\alpha \rangle (E)$ and $n_\alpha(E)$. In low electric fields, J is linear in E, but the linear relation is broken around $E = E_{\mathrm{crit}}$. Then, at $E > E_{\mathrm{crit}}$, current density decreases because the dust adsorption rate of electron, K_{de}, steeply increases.

As stated above, OI15 showed the nonlinear relation between current density and electric field strength by considering electron heating. The nonlinearity comes from the dependence of electric resistivity on electric field strength. The resistivity increased by electron heating might suppresses MRI. This effect has never considered in protoplanetary disk so far. The suppression of MRI impacts on both the disk evolution and dust growth. In the next chapter, we investigate zones where the electron heating stabilizes MRI.

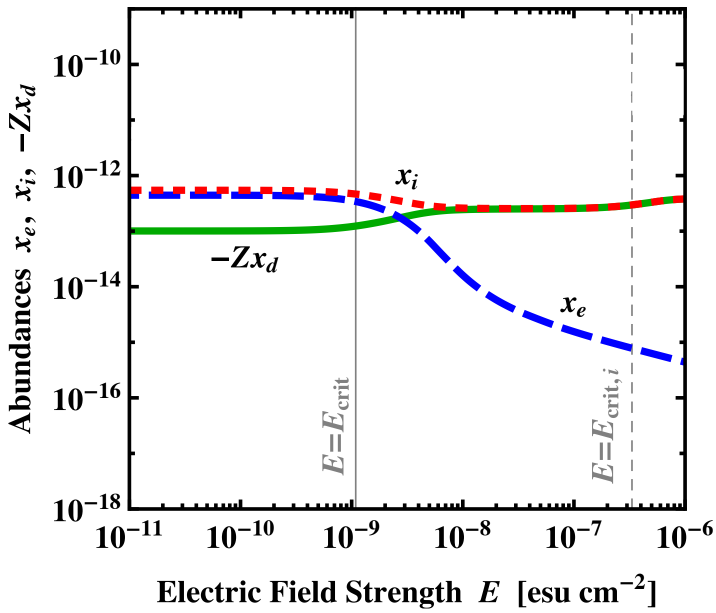

Figure 2.6: Dependence of plasma abundance on electric field strength. The vertical axis shows the abundances, and the horizontal axis shows electric field strength. The red dashed line shows the ion abundance $x_i = n_i/n_n$, the blue dashed line the electron abundance $x_e = n_e/n_n$, the green solid line the abundance of number of charges on dust grains $-Zx_d = Zn_d/n_n$. $E_{\rm crit}$ and $E_{{\rm crit},i}$ shows the electric fields where electron and ion heating start, respectively.

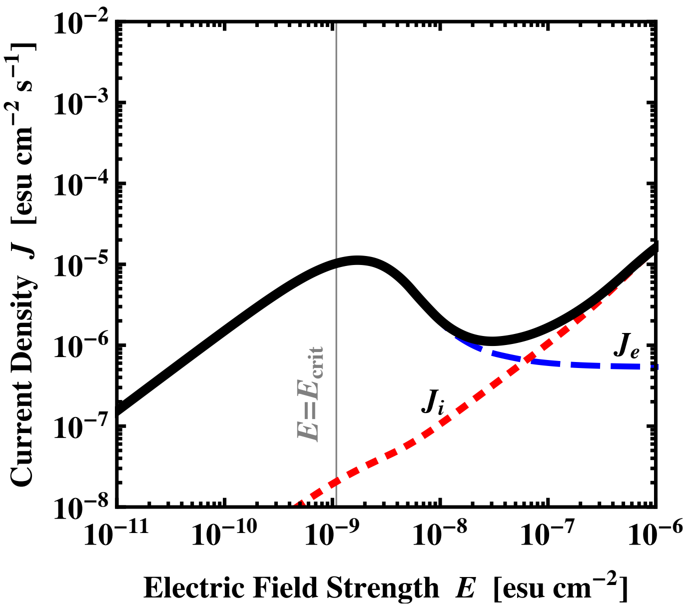

Figure 2.7: Nonlinear Ohm's law of OI15. The blue dashed line shows the electron current density, red dashed line the ion current density, black solid line the sum of these current density. The model assumes that the dust-to-gas ratio $f_{dg} = 0.01$, the ionization rate $\zeta = 10^{-17}{\rm s}^{-1}$, neutral gas temperature $T_n = 100$ K, number density of neutral gas particle $n_n = 10^{12}{\rm cm}^{-3}$, the radius of dust grains $a = 1\mu$m, and the material density $\rho_\bullet = 2{\rm g\ cm}^{-3}$.

Chapter 3

Electron Heating Zone : Mori & Okuzumi (2016)

In this chapter, we present our previous study, MO16. Inutsuka & Sano (2005) found the electron heating as a new ionization source in magnetic turbulence, i.e. collisional ionization by energetic electrons. After that, OI15 has found the electron heating would change ionization balance by electrons sticking to dust before the collisional ionization. However, these studies did not clarify the locations and the impacts on disk evolution. We here investigate the region where electron heating would affect MRI turbulence.

In Section 3.1, we present the disk model, simplified plasma heating model, and ionization balance. In Section 3.2, we present some conditions for MRI growth and some criteria for mapping of turbulent state in a disk. We also briefly summarize the turbulent state and calculation steps. In Section 3.3, we show where the electron heating affects MRI turbulence. We also consider cases with various parameters. In Section 3.4, we estimate how the electron heating suppresses MRI turbulence. In Section 3.5, we discuss the effect of heated electrons on the electric repulsion and the collisional growth of dust grains.

3.1 Disk and Ionization Models

3.1.1 Disk Model

We consider a gas disk around a solar-mass star. We assume that the surface density of the disk gas obeys a power law

$$\Sigma(r) = 1.7 \times 10^3 f_\Sigma \left(\frac{r}{1\ \mathrm{AU}}\right)^{-3/2}\ \mathrm{g\,cm^{-2}}, \tag{3.1}$$

where r is the distance from the central star, and f_Σ is a dimensionless parameter. The choice of $f_\Sigma = 1$ corresponds to the minimum-mass solar nebula (MMSN) model of Hayashi (1981), which we take as the fiducial model.

We assume that the disk is optically thin and give the temperature profile as (Hayashi, 1981)

$$T(r) = 280 \left(\frac{r}{1\ \mathrm{AU}}\right)^{-1/2}\ \mathrm{K}, \tag{3.2}$$

where the central star is assumed to have the solar luminosity.

The sound speed is given by $c_\mathrm{s} = \sqrt{kT/m_n}$, where m_n is the mass of a neutral gas particle, and k is the Boltzmann constant. Assuming $m_n = 2.34$ amu and using Equation (3.2), we have

$$c_\mathrm{s}(r) = 1.0 \times 10^5 \left(\frac{r}{1\ \mathrm{AU}}\right)^{-1/4}\ \mathrm{cm\,s^{-1}}. \tag{3.3}$$

We assume that the gas disk is hydrostatic in the vertical direction and give the vertical distribution of the gas density as

$$\rho(r, z) = \rho_c(r) \exp\left(-\frac{z^2}{2H^2}\right), \tag{3.4}$$

where ρ_c is the mid-plane density and $H \equiv c_\mathrm{s}/\Omega$ is the gas scale height with $\Omega = 2.0 \times 10^{-7}\ (r/1\ \mathrm{AU})^{-3/2}\ \mathrm{s^{-1}}$ being the orbital frequency (note that a solar-mass star is assumed). Using the relation $\Sigma = \int_{-\infty}^{\infty} \rho dz = \sqrt{2\pi} H \rho_c$, we have

$$\rho_c(r) = 1.4 \times 10^{-9} f_\Sigma \left(\frac{r}{1\ \mathrm{AU}}\right)^{-11/4}\ \mathrm{g\ cm^{-3}}. \tag{3.5}$$

Thus, the number density of gas particles $n_n = \rho/m_n$ is given as

$$n_n(r,z) = 3.5 \times 10^{14} f_\Sigma \times \left(\frac{r}{1\ \mathrm{AU}}\right)^{-11/4} \exp\left(-\frac{z^2}{2H^2}\right)\ \mathrm{cm}^{-3}. \quad (3.6)$$

As we will describe in Section 3.2.1, the criteria for MRI depends on the magnetic field strength in the disk. Following Sano et al. (2000), we consider a net (large-scale) vertical field B_{z0} threading the disk and specify its strength with the plasma beta at the midplane, $\beta_c \equiv 8\pi\rho_c c_\mathrm{s}^2/B_{z0}^2$. If we use Equations (3.3) and (3.5), the net vertical field strength can be expressed as

$$B_{z0}(r) = 0.59 f_\Sigma^{1/2} \left(\frac{\beta_c}{1000}\right)^{-1/2} \left(\frac{r}{1\ \mathrm{AU}}\right)^{-13/8}\ \mathrm{G}. \quad (3.7)$$

For simplicity, we will assume that β_c is constant in the radial direction.

The charge reaction model adopted in this study takes into account the effects of grain charging on the ionization balance. For simplicity, we assume that dust grains are well mixed in the gas so that the dust-to-gas mass ratio f_{dg} is a global constant. We also assume that the grains are spherical and single-sized with radius a (taken as a free parameter) and internal density $\rho_\bullet$ (fixed to be 3 g cm^{-3}). From these assumptions, the number density of dust grains n_d is given by $3f_{dg}\rho/(4\pi a^3\rho_\bullet)$, which is expressed as

$$\begin{aligned} n_d(r,z) &= 1.1 \times 10^3 f_\Sigma \left(\frac{f_{dg}}{0.01}\right) \left(\frac{\rho_\bullet}{3\ \mathrm{g\ cm^{-3}}}\right)^{-1} \left(\frac{a}{0.1\ \mu\mathrm{m}}\right)^{-3} \\ &\quad \times \left(\frac{r}{1\ \mathrm{AU}}\right)^{-11/4} \exp\left(-\frac{z^2}{2H^2}\right)\ \mathrm{cm}^{-3}. \end{aligned} \quad (3.8)$$

The disk is assumed to be ionized by galactic cosmic rays, stellar X-rays, and radionuclides. The ionization rate can be expressed as

$$\zeta = \zeta_\mathrm{CR} + \zeta_\mathrm{XR} + \zeta_\mathrm{RN}, \quad (3.9)$$

where ζ_CR, ζ_XR, and ζ_RN stand for the contributions from cosmic rays, X-rays, and radioactive decay, respectively. The cosmic ray distribution is expressed as (Umebayashi

& Nakano, 2009)

$$
\begin{aligned}
\zeta_{\rm CR} &= \frac{\zeta_{\rm CR,0}}{2}\left\{\exp\left(-\frac{\chi}{\chi_{\rm CR}}\right)\left[1+\left(\frac{\chi}{\chi_{\rm CR}}\right)^{3/4}\right]^{-4/3}\right. \\
&\left. +\exp\left(-\frac{\Sigma-\chi}{\chi_{\rm CR}}\right)\left[1+\left(\frac{\Sigma-\chi}{\chi_{\rm CR}}\right)^{3/4}\right]^{-4/3}\right\}, \qquad (3.10)
\end{aligned}
$$

where $\zeta_{\rm CR,0} = 1.0\times10^{-17}\ {\rm s}^{-1}$ is the characteristic ionization rate of cosmic rays, $\chi(r,z) = \int_z^\infty \rho(r,z')dz'$ is the vertical gas column density above height z, and $\chi_{\rm CR} = 96\ {\rm g\ cm}^{-2}$ is the attenuation depth of ionizing cosmic rays. The ionization rate of X-rays is expressed as (Bai & Goodman, 2009)

$$
\begin{aligned}
\zeta_{\rm XR} &= \frac{L_X}{10^{29}\ \ {\rm erg\ s}^{-1}}\left(\frac{r}{1\ {\rm AU}}\right)^{-2.2} \\
&\times\left\{\zeta_{\rm XR,1}\left[\exp\left(-\left(\frac{\chi}{\chi_{\rm XR,1}}\right)^{0.4}\right)+\exp\left(-\left(\frac{\Sigma-\chi}{\chi_{\rm XR,1}}\right)^{0.4}\right)\right]\right. \\
&\left.+\zeta_{\rm XR,2}\left[\exp\left(-\left(\frac{\chi}{\chi_{\rm XR,2}}\right)^{0.65}\right)+\exp\left(-\left(\frac{\Sigma-\chi}{\chi_{\rm XR,2}}\right)^{0.65}\right)\right]\right\}, \qquad (3.11)
\end{aligned}
$$

where $\chi_{\rm XR,1}$ and $\chi_{\rm XR,2}$ are taken to be $6\times10^{-3}\ {\rm g\ cm}^{-2}$ and $3\ {\rm g\ cm}^{-2}$ respectively, $\zeta_{\rm XR,1}$ and $\zeta_{\rm XR,2}$ are taken to be $6\times10^{-12}\ {\rm s}^{-1}$ and $1\times10^{-15}\ {\rm s}^{-1}$ respectively. We take $L_x = 2\times10^{30}\ {\rm erg\ s}^{-1}$ in accordance with the median X-ray luminosity of solar-mass young stars (Wolk et al., 2005). The ionization rate of the radionuclide is expressed as (Umebayashi & Nakano, 2009)

$$
\zeta_{\rm RN} = 7.6\times10^{-19}\left(\frac{f_{dg}}{0.01}\right)\ {\rm s}^{-1}. \qquad (3.12)
$$

3.1.2 Simplified Plasma Heating Model

As we will describe in Section 3.2.1, the criterion for MRI depends on the ionization fraction in the disk. We employ a simple ionization model proposed by OI15 to calculate the ionization fraction taking into account plasma heating by a strong electric field. The model determines the ionization fraction of the gas at each location of a disk from the balance between ionization by external high-energy sources (e.g., cosmic rays and X-rays), recombination in the gas phase, and adsorption of ionized gas particles onto dust grains. The rates of recombination and adsorption generally depend on the temperatures of ions and electrons, T_i and T_e. Previous ionization models assumed that T_i and T_e are equal to the neutral gas temperature T. By contrast, the model of OI15 determines T_i and T_e as a function of the electric field strength E. For simplicity, positive ions are represented by the single species HCO^+, which is good as a first-order approximation when heavy molecular ions that recombine through dissociation reactions dominate (Umebayashi & Nakano, 1990; Dzyurkevich et al., 2013). We do not consider negative ions. Although production of negative ions is rare in cool protoplanetary disks, electrons heated to $\gtrsim 3$ eV can produce negative hydrogen ions H^- via dissociative electron attachment $H_2 + e^- \rightarrow H^- + H$ (Wadehra, 1984). However, H^- would be instantly destroyed by CO, the most abundant molecule after H_2, via the reaction $H^- + CO \rightarrow HCO + e^-$ (Ferguson, 1973). For this reason, we may safely neglect the dissociative electron attachment during electron heating.

In this study, we make two further simplifications to the original model of OI15. Firstly, we calculate the electron temperature T_e by solving the equations of momentum and energy conservation rather than by using the solution to the full Boltzmann equation. The rate coefficients for gas-phase recombination and plasma adsorption onto grains are then evaluated by approximating the velocity distribution function with a Maxwellian with temperature T_e. The approach greatly simplifies the analytic expressions of the rate coefficients that otherwise involve confluent hypergeometric functions (see Section 3 of OI15). Such an approach was originally proposed by Hershey (1939) for calculating the mobility of heavy ions at a high electric field, and OI15 followed this approach to compute the ion temperature T_i. In this study, we apply this approach to both T_i and T_e. Secondly, we neglect the impact ionization of neutral molecules by electrically heated electrons by assuming that the electron energy in MRI turbulence is well below the ionization potential of the neutrals (~ 10 eV). The results of our calculations show that this assumption holds in most parts of protoplanetary disks.

We denote the mean drift velocity and mean kinetic energy of a charged species α ($= i$ for ions, e for electrons) by $\langle \boldsymbol{v}_\alpha \rangle$ and $\langle \epsilon_\alpha \rangle$, respectively. In a weakly ionized gas with an applied electric field $\boldsymbol{E}$, the momentum and energy of the charged species are determined by the balance between the neutral gas drag and acceleration by the electric field (Hershey, 1939). Explicitly, the solution of the momentum and energy balance equations can be written as (Equations (A9) and (A10) of OI15)

$$\langle \boldsymbol{v}_\alpha \rangle = \frac{m_\alpha + m_n}{m_\alpha m_n} q_\alpha \boldsymbol{E} \Delta t_\alpha, \tag{3.13}$$

$$\langle \epsilon_\alpha \rangle = \frac{3}{2} kT + \frac{(m_\alpha + m_n)^3}{2(m_\alpha m_n)^2} (q_\alpha E \Delta t_\alpha)^2, \tag{3.14}$$

where q_α, m_α, and Δt_α are the charge, mass and mean free time of the plasma particles (e.g., $q_e = -e$ and $q_i = e$, where e is the elementary charge). Since the magnetic field is neglected in this study, the mean drift velocity is parallel to the electric field. In a weakly ionized gas, the plasma mean free time is determined by neutrals gas particles,

$$\Delta t_\alpha = (n_n \langle \sigma_{\alpha n} v_{\alpha n} \rangle)^{-1}, \tag{3.15}$$

where $v_{\alpha n}$ is the relative velocity between a plasma particle and a neutral particle, and $\sigma_{\alpha n}$ is the momentum-transfer cross section for the plasma–neutral collision. For electrons, σ_{en} is approximately constant at low energies (Yoon et al., 2008), and therefore we may approximate $\langle \sigma_{en} v_{en} \rangle$ as $\sigma_{en} \langle v_{en} \rangle$. For ions, $\langle \sigma_{in} v_{in} \rangle$ is approximately constant owing to the polarization force between ions and neutrals (Wannier, 1953). Equations (3.13) and (3.14) are exact only when Δt_α is constant, but still hold in a good accuracy even when Δt_α is velocity-dependent (Wannier, 1953).

The plasma temperature T_α is defined so that $3kT_\alpha/2$ is equal to the kinetic energy of random motion, $\langle \epsilon_\alpha \rangle - m_\alpha \langle \boldsymbol{v}_\alpha \rangle^2 /2$. Using Equations (3.13) and (3.14), T_α can be written as

$$T_\alpha = T + \frac{(m_\alpha + m_n)^2}{3k m_\alpha^2 m_n} (q_\alpha E \Delta t_\alpha)^2. \tag{3.16}$$

For electrons, we approximate $\langle v_{en} \rangle$ in Δt_e with $\langle v_e^2 \rangle^{1/2} = \sqrt{3kT_e/m_e}$. This allows us to solve Equation (3.16) with respect to T_e, and we obtain

$$T_e = T \left(\frac{1}{2} + \sqrt{\frac{1}{4} + \frac{2}{3} \left(\frac{E}{E_{\rm crit}} \right)^2} \right), \tag{3.17}$$

where

$$E_{\rm crit} \equiv \sqrt{\frac{6m_e}{m_n}}\frac{kTn_n\sigma_{en}}{e} \tag{3.18}$$

is the critical field strength above which electron heating becomes significant. We have assumed $m_e \ll m_n$ in deriving Equation (3.17). For ions, Equation (3.16) directly gives

$$\begin{aligned} T_i &= T\left(1+\frac{2(m_i+m_n)^2m_e}{m_i^2m_n^2}\frac{\sigma_{en}^2kT}{\langle\sigma_{in}v_{in}\rangle^2}\left(\frac{E}{E_{\rm crit}}\right)^2\right), \\ &= T\left(1+7.6\times10^{-7}\left(\frac{T}{100K}\right)\left(\frac{E}{E_{\rm crit}}\right)^2\right), \end{aligned} \tag{3.19}$$

where we have set $\langle\sigma_{in}v_{in}\rangle = 1.6\times10^{-9}$ cm^3 s^{-1} (Nakano & Umebayashi, 1986) and $\sigma_{en} = 10^{-15}$ cm^2 (Yoon et al., 2008) in the second expression, and used $m_i = 29$ amu.

3.1.3 Ionization Balance and Accuracy of Simplified Approach

We calculate the plasma densities in a protoplanetary disk taking into account grain charging. The equations that describe the ionization balance in a dusty disk are (Equations (32), (33) and (35) of OI15)

$$\zeta n_n - K_{\rm rec}(T_e)n_in_e - K_{de}(\phi, T_e)n_dn_e = 0, \tag{3.20}$$

$$\zeta n_n - K_{\rm rec}(T_e)n_in_e - K_{di}(\phi, T_i)n_dn_i = 0, \tag{3.21}$$

$$n_i - n_e + Zn_d = 0, \tag{3.22}$$

where n_e and n_i are, respectively, the number density of electrons and positive ions; $K_{\rm rec}$ is the gas-phase recombination rate; K_{de} and K_{di} are the adsorption rates of electrons and ions onto grains; Z is the grain charge number; and ϕ is the coulomb potential on grain surface. ϕ is related to Z as

$$\phi = \frac{eZ}{a}. \tag{3.23}$$

As the collisional frequency, $K_{\rm rec}$ and K_{de} depend on the electron temperature T_e, while K_{di} depends on the ion temperature T_i. K_{de} and K_{di} also depend on the coulomb potential of a grain surface ϕ. For HCO^+, the recombination rate $K_{\rm rec}$ is given by

(Ganguli et al., 1988)

$$K_{\rm rec}(T_e) = 2.4 \times 10^{-7} \left(\frac{T_e}{300\ {\rm K}}\right)^{-0.69}\ {\rm cm^3\ s^{-1}}. \tag{3.24}$$

Approximating the ion velocity distribution by a Maxwellian with mean velocity $\langle \boldsymbol{v}_i \rangle$ and temperature T_i, K_{di} is given by (Shukla & Mamun, 2002, OI15)

$$\begin{aligned} K_{di}(\phi, T_i) \;=\; \pi a^2 \Bigg[& \sqrt{\frac{2kT_i}{\pi m_i}} \exp\left(-\frac{m_i \langle \boldsymbol{v}_i \rangle^2}{2kT_i}\right) \\ & + |\langle \boldsymbol{v}_i \rangle| \left(1 + \frac{kT_i + 2e|\phi|}{m_i \langle \boldsymbol{v}_i \rangle^2}\right) {\rm erf}\left(\frac{|\langle \boldsymbol{v}_i \rangle|}{\sqrt{2kT_i/m_i}}\right)\Bigg]. \end{aligned} \tag{3.25}$$

In this study, we also approximate the electron velocity distribution by a Maxwellian with temperature T_e. The drift velocity $\langle \boldsymbol{v}_e \rangle$ can be neglected here since the drift speed $|\langle \boldsymbol{v}_e \rangle|$ is generally much smaller than the random speed $\sim \sqrt{kT_e/m_e}$ owing to the smallness of m_e/m_n (see Golant et al., 1980; Lifshitz & Pitaevskii, 1981). The electron adsorption rate coefficient K_{de} is given by the simple expression (Shukla & Mamun, 2002)

$$K_{de}(\phi, T_e) = \pi a^2 \sqrt{\frac{8kT_e}{\pi m_e}} \times \begin{cases} \left(1 + \dfrac{e\phi}{kT_e}\right), & \phi > 0, \\ \exp\left(\dfrac{e\phi}{kT_e}\right), & \phi < 0. \end{cases} \tag{3.26}$$

It should be noted that Equations (3.26) and (3.25) assume perfect sticking of ions and electrons onto grain surfaces. This is a good approximation as long as the plasma temperatures are well below 100 eV (see Section 3.2.2 of OI15 for more discussion).

Equations (3.20)–(3.22) determine n_e, n_i and Z at each location in a disk as a function of E. We solve these equations using the procedure presented by Okuzumi (2009, their Section 2.2; see also Section 3.2.4 of OI15).

To test the accuracy of our simplified approach, we reproduce the current–field relation including plasma heating (the nonlinear Ohm's law of OI15) with adopting the calculation steps in OI15. Current density is generally given by

$$J(E) = q_e n_e \langle \boldsymbol{v}_e \rangle + q_i n_i \langle \boldsymbol{v}_i \rangle . \tag{3.27}$$

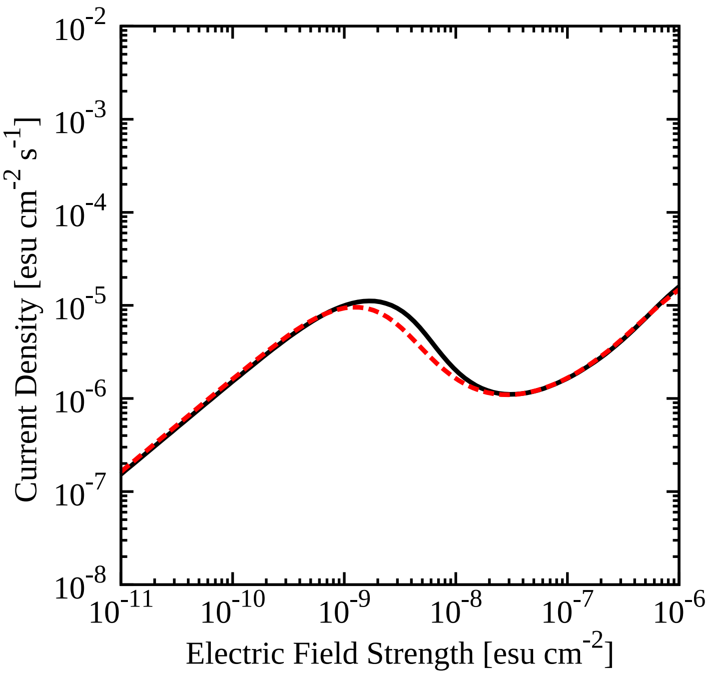

Figure 3.1: Test of the simplified plasma heating model presented in Section 3.1.3. The solid curve shows the J–E relation for 'model C' of OI15 derived using the exact electron velocity distribution (see Figure 10 of OI15), while the dashed curve shows our reproduction based on the simplified approach.

Including plasma heating, the number densities depend on the electric fields strength E. To obtain the current density, we first calculate plasma temperatures T_e and T_i from Equations (3.17) and (3.19) in an applied electric field E. We then calculate the number densities of plasma n_e and n_i from the ionization balance (Equation (3.22)). We finally obtain the current density using Equations (3.13) and (3.27). In Figure 3.1, we compare our result with the result of OI15 for the parameter set 'model C' of OI15. We find that our calculation reasonably reproduces the previous result even at high field strengths ($E \gtrsim 10^{-9}$ esu cm^{-2}) where electron heating is significant. The maximum relative difference between the two results is 37%.

3.2 Active, Dead, and E-heating Zone

3.2.1 Conditions for MRI Growth

In the limit of ideal MHD, the criterion for the MRI is given by (Balbus & Hawley, 1991)

$$\lambda_{\rm ideal} < H, \tag{3.28}$$

where

$$\lambda_{\rm ideal} \equiv 2\pi \frac{v_{Az}}{\Omega} \tag{3.29}$$

is the characteristic wavelength of the most unstable axisymmetric MRI modes, and $v_{Az} = B_z/\sqrt{4\pi\rho}$ and B_z are the vertical components of the Alfven velocity and magnetic field, respectively. Equation (3.28) expresses that the MRI operates when the lengthscale of the MRI modes is smaller than the vertical extent of the disk. When viewed as a function of z, $\lambda_{\rm ideal}$ increases with z because ρ decreases toward the disk surface. If we use Equation (3.4), the above MRI criterion can be rewritten in terms of height as

$$z < \sqrt{2\ln\left(\beta_c/8\pi^2\right)}\; H \equiv H_{\rm ideal}, \tag{3.30}$$

where the height $H_{\rm ideal}$ defines the upper boundary of the MRI active zone.

Inclusion of a finite Ohmic resistivity η introduces another criterion for MRI growth. The criterion can be expressed in terms of the Elsasser number (Turner et al., 2007)

$$\Lambda \equiv \frac{v_{Az}^2}{\eta\Omega}. \tag{3.31}$$

The instability grows when

$$\Lambda > 1 \tag{3.32}$$

and decays when $\Lambda < 1$ (e.g., Sano & Miyama, 1999).

3.2.2 Zoning Criteria

Here we describe how to determine turbulent state at a position in protoplanetary disks. Electron heating affects on the MRI turbulence when the ionization fraction is sufficiently decreased. We express the condition that the heating takes place and affect MRI turbulence, and then summarize three turbulent states of MRI and steps of zoning a disk into the state.

For electron heating to take place, the field must be sufficiently amplified before MRI turbulence reaches a fully developed state that means the stop of MRI growth. Muranushi et al. (2012) performed a local unstratified resistive MHD simulation and found that the fully developed current density is

$$J_{\max} = f_{\mathrm{sat}} \sqrt{\frac{\rho}{2\pi}} c\Omega, \tag{3.33}$$

where $f_{\mathrm{sat}} \approx 10$ according to the results by Muranushi et al. (2012). Here, we assume f_{sat} to be $f_{\mathrm{sat}} = 10$ and the maximum current density is $J_{\max}$. Thus, when the current density reaches $J_{\max}$ before electric field reaches the criterion for electron heating E_{crit}, MRI turbulence does not cause the electron heating.

As we will describe later in this section, we use current density to decide whether electron heating take place or not. Therefore, we transform the condition for suppressing MRI into a form using current density. We adopt $\Lambda = 1$ (Equation (3.32)) as the criterion for suppressing MRI which is triggered by electron heating. Using the electric conductivity σ_c and the relation $\eta = c^2/4\pi\sigma_c$, the condition for sustaining MRI turbulence $\Lambda \gtrsim 1$ leads to a condition $\sigma_c \gtrsim c^2\Omega/(4\pi v_{Az}^2)$. Under the Ohm's law $J(E) = \sigma_c E$, the condition can be rewritten as a lower limit to the current density

$$J(E) \gtrsim J_{\Lambda=1}(E), \tag{3.34}$$

where

$$J_{\Lambda=1}(E) \equiv \sigma_c(\Lambda = 1)E = \frac{c^2\Omega}{4\pi v_{Az}^2} E. \tag{3.35}$$

Using the above criteria, we can classify a region in protoplanetary disks into three

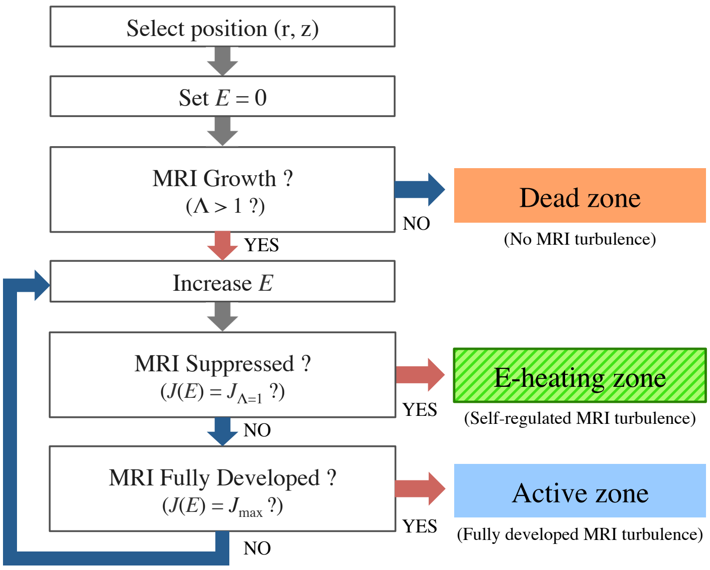

Figure 3.2: Flow chart showing key steps of zoning a protoplanetary disk into the dead, active, and e-heating zones.

different zones corresponding to three turbulent state of MRI.

1. *Dead zone.* Because of the low ionization fraction, Ohmic dissipation suppress all the unstable MRI mode. Suppressed MRI does not generate turbulence and also current density. We will refer to the region where MRI is completely suppressed as the "dead zone". In this case, the condition of Ohmic dissipation (Equation (3.35)) is satisfied with no MRI turbulence.

2. *E-heating zone.* Electric fields of MRI turbulence become sufficiently high for electron heating to be caused. The Ohmic dissipation is amplified by the electron heating after the MRI grows. We will refer to the region where electron heating affects MRI turbulence as the "e-heating zone", where the "e" refers to both "electric field" and "electron." In this case, current density falls down the critical current density of Ohmic dissipation (Equation (3.35)).

3. *Active zone.* MRI sustains fully developed turbulent state because the gas is sufficiently ionized so that Ohmic dissipation is not efficient. We will refer to the region where vigorous MRI turbulence is sustained as the "active zone" in this study. In this case, the current density J reaches and sustains its maximum value $J_{\rm max}$ before electron heating reduces the MRI turbulence.

We summarize the calculation steps for zoning the disk region under some assumptions. We assume that the electric field strength correspond to the activity of MRI turbulence since developed MRI generates strong electric fields. The growth of MRI implies increasing electric fields, and the decay of MRI implies decreasing electric fields. Furthermore, we also assume that magnetic fields are not varied by the MRI growth for simplicity. Under these assumptions, we determine the turbulent state at the position with following steps (see Figure 3.2): First, we select a calculated position in the region satisfying Equations (3.30) of a disk. We then calculate values at the position with setting $E = 0$. When MRI is initially suppressed by Ohmic dissipation, i.e., $\Lambda < 1$ at $E = 0$, the positions belong to the dead zone. During satisfying unstable condition, i.e., $\Lambda > 1$, the electric field strength E is increased from $E = 0$ with iterating until the turbulent state at the position is determined. We calculate current density $J(E)$ and assess some conditions in E. When MRI turbulence causes electron heating and Ohmic dissipation become efficient, i.e., $J(E) = J_{\Lambda=1}$, the position belongs to the e-heating zone. When MRI turbulence is fully developed, i.e., $J(E) = J_{\max}$, the position belongs to the active zone. We conduct the above steps in the whole region in a disk, and zone a protoplanetary disk into the dead, active, and e-heating zones.

3.3 Location of the E-heating Zone

We here predict the location of the e-heating zone in protoplanetary disks using the methodology described in Section 3.2.2. We conduct a parameter study varying the midplane plasma beta β_c, grain size a, dust-to-gas mass ratio f_{dg}, and surface density scaling factor f_Σ. Following Sano et al. (2000), we select the MMSN ($f_\Sigma = 1$ and $q = 3/2$) with $a = 0.1\ \mu$, $f_{dg} = 0.01$, and $\beta_c = 1000$ as the fiducial model. We start out with this fiducial model in Section 3.3.1, and discuss the dependence on the parameters in the subsequent subsections. A summary of the parameter study is given in Table 3.1. We also describe ion heating in Section 3.3.5.

Table 3.1: Sizes of the Dead and E-heating Zones for Various Parameter Sets

β_c	a (μm)	f_{dg}	f_Σ	Outer radius (AU)	
				Dead zone	E-heating zone
10^2	0.1	10^{-2}	1	18	74
10^3	0.1	10^{-2}	1	24	82
10^4	0.1	10^{-2}	1	34	82
10^5	0.1	10^{-2}	1	56	82
10^3	0.1	10^{-2}	1	24	82
10^3	1	10^{-2}	1	11	39
10^3	10	10^{-2}	1	8	19
10^3	100	10^{-2}	1	8	11
10^3	0.1	10^{-1}	1	52	151
10^3	0.1	10^{-2}	1	24	82
10^3	0.1	10^{-3}	1	12	41
10^3	0.1	10^{-4}	1	8	20
10^3	0.1	10^{-2}	10	55	149
10^3	0.1	10^{-2}	3	36	114
10^3	0.1	10^{-2}	1	24	82
10^3	0.1	10^{-2}	0.3	14	44

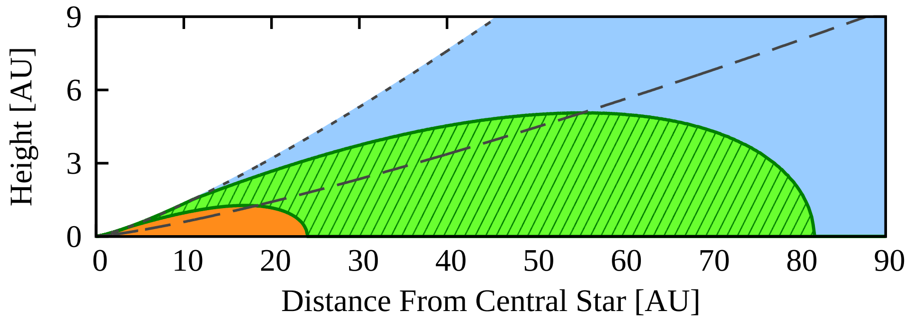

Figure 3.3: Cross-section view of the fiducial protoplanetary disk indicating the location of the dead, e-heating and active zones (red, green-shaded, and blue regions, respectively). The dashed line shows the gas scale height H, while the dotted line shows the critical height $H_{\rm ideal}$ below which the MRI criterion in the ideal MHD limit is satisfied (see Equation (3.30)).

3.3.1 Fiducial Disk Model

Figure 3.3 shows the two-dimensional (radial and vertical) map of the dead, active, and e-heating zone in the fiducial disk model. The MRI criterion in the ideal MHD limit (Equation (3.28)) is satisfied at altitudes below $z = H_{\rm ideal} \approx 2.3H$ (see Equation (3.30)). The region above this height is MRI-stable with the MRI modes suppressed by too strong magnetic tension. The dead zone is located inside 24 AU from the central star and near the midplane where the gas is shielded from ionizing irradiation. The size of the dead zone for this disk model is consistent with the prediction by Sano et al. (2000) (see their Figure 7(b)), although their dead zone is slightly thicker than ours because of the neglect of X-ray ionization. We find that the e-heating zone extends from the outer edge of the dead zone out to 82 AU from the central star. This means that MRI turbulence can develop without affected by electron heating only in the outermost region of $r \gtrsim 80$ AU.

To illustrate how our zoning criteria work in this particular example, we plot in Figure 3.4 the relation between the current density J and electric field E in the midplane at 15 AU, 45 AU and 90 AU, which represent the dead, e-heating, and active zones, respectively. Recall that for fixed E, MRI turbulence grows if $J(E) > J_{\Lambda=1}$ and decays otherwise (Equation (3.34)). At 15 AU, $J(E)$ falls below $J_{\Lambda=1}$ for all values of E, implying that the MRI is unable to grow at this location. At 45 AU, the MRI growth condition is satisfied during the initial growth stage of $E \ll 10^{-11}$ esu cm^{-2}, but breaks down *before J reaches* $J_{\rm max}$ because of the decrease in $J(E)$ due to electron heating. This implies that MRI turbulence is allowed to grow in the initial stage but saturates at a level lower than that for fully developed turbulence. At 90 AU, $J(E)$ reaches $J_{\rm max}$ before electron heating sets in, implying that fully developed MRI turbulence is sustained here.

In contrast to electron heating, ion heating is found to be negligible at all locations in the fiducial disk model. In the e-heating zone, the electric field strength at the saturation point is typically $\lesssim 10^2 E_{\rm crit}$ (see the center and right panels of Figure 3.4), which is an order of magnitude lower than the field strength required for ion heating, $10^3 E_{\rm crit}$.

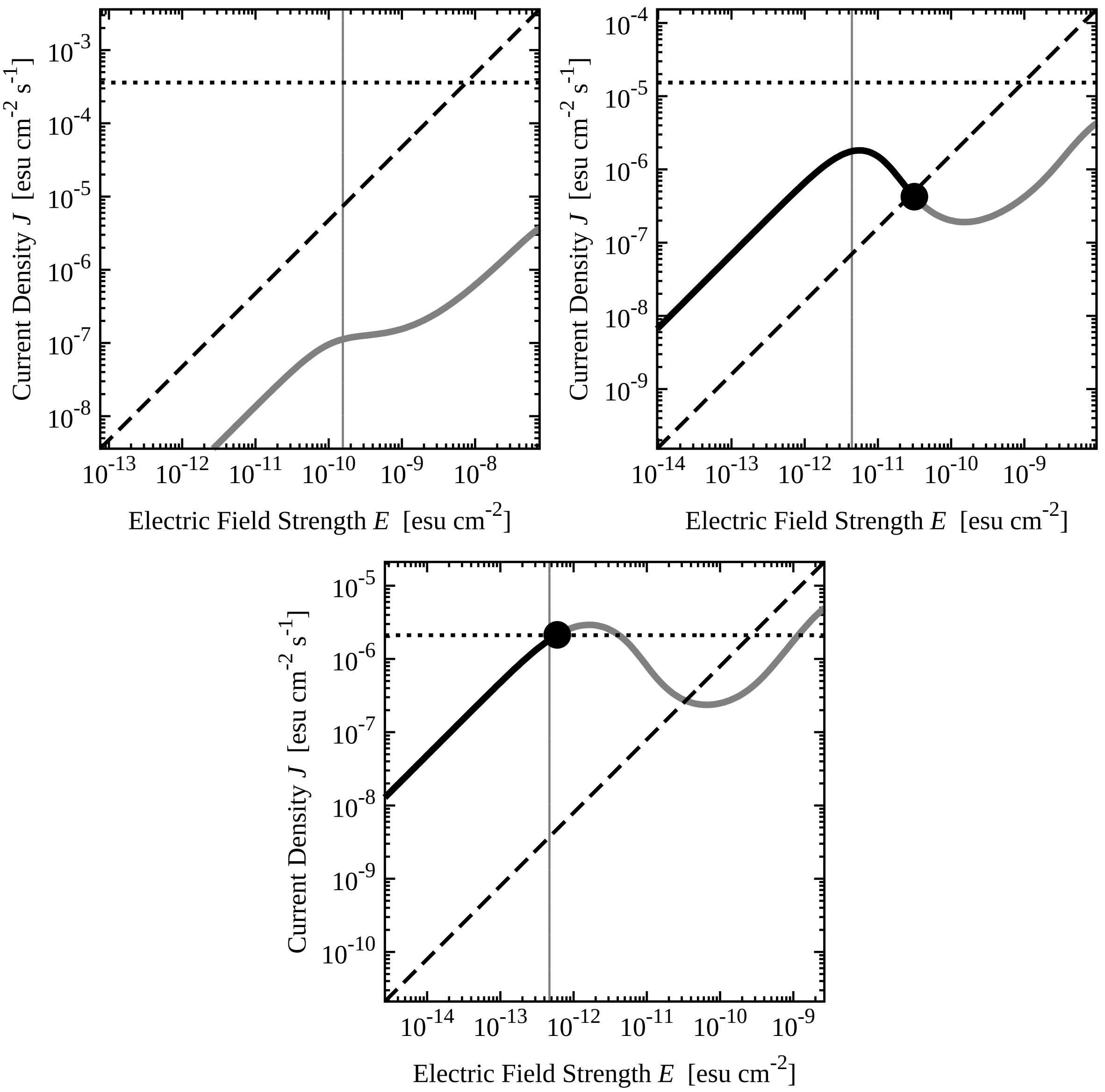

Figure 3.4: Relations between the current density J and electric field strength E in the midplane at 15 AU (upper left panel), 45 AU (upper right panel), and 90 AU (lower panel), which represent the J–E relations in the dead, e-heating, and active zones, respectively. The thick solid line shows the current–field relation $J(E)$, the dotted line the maximum current density of MRI, $J_{\max}$ (Equation (3.33)), the vertical gray solid line the criterion for electron heating, $E_{\rm crit}$ (Equation (3.18)), and the dashed line the critical current density $J_{\Lambda=1}$ below which the MRI decays owing to Ohmic dissipation (Equation (3.35)). The black dots on the J–E relations indicate the saturation points at which either fully developed ($J(E) = J_{\max}$) or self-regulated ($J(E) = J_{\Lambda=1}$) MRI turbulence is sustained.

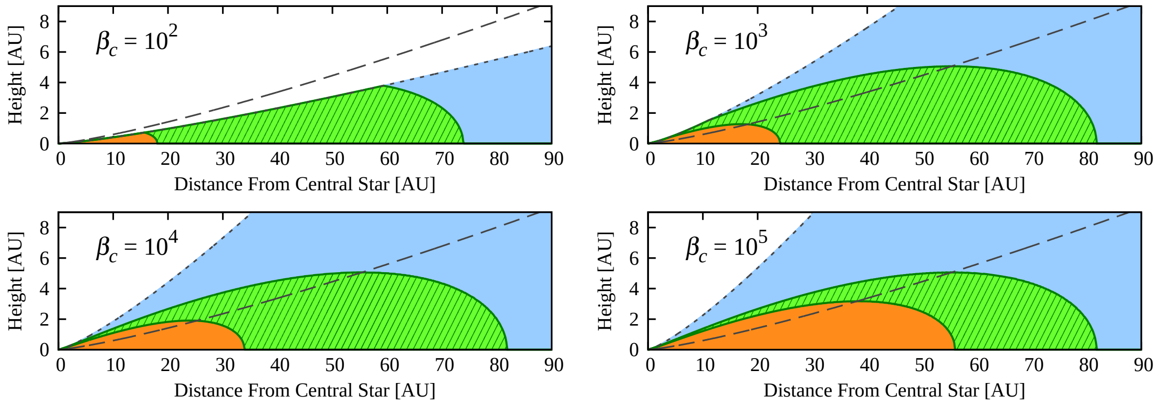

Figure 3.5: Same as Figure 3.3, but for different values of the midplane beta β_c.

3.3.2 Dependence on the Magnetic Field Strength

Figure 3.5 shows how the size of the dead and e-heating zones depend on the midplane plasma beta β_c. Recall that a higher β_c corresponds to a weaker magnetic field B threading the disk. As we increase β_c, the dead zone expands because the Elsasser number $\Lambda \propto B^2$ decreases. On the other hand, we find that the boundary between the e-heating and active zones is less sensitive to the choice of β_c. As can be inferred from the middle and right panels of Figure 3.4, this boundary is approximately determined by the condition that the current density $J(E)$ reaches $J_{\rm max}$ at a local maximum lying at $E \approx E_{\rm crit}$. Since both $E_{\rm crit}$ and $J_{\rm max}$ are independent of B and hence of β_c, so is the boundary between the e-heating and active zones.

3.3.3 Dependence on the Grain Size and Dust-to-Gas Mass Ratio

The size and amount of dust grains in disks are important parameters in the ionization model as they efficiently remove plasma particles from the gas phase. Obviously, these quantities change as the grains coagulate, settle, or are incorporated by even larger solid bodies like planetesimals. We here explore how the change of these parameters affect the size of the dead and e-heating zones.

To begin with, we show in Figure 3.6 the location of the dead, active, and e-heating zones with the dust-to-gas ratio f_{dg} fixed to 0.01 but with the grain size a varying between

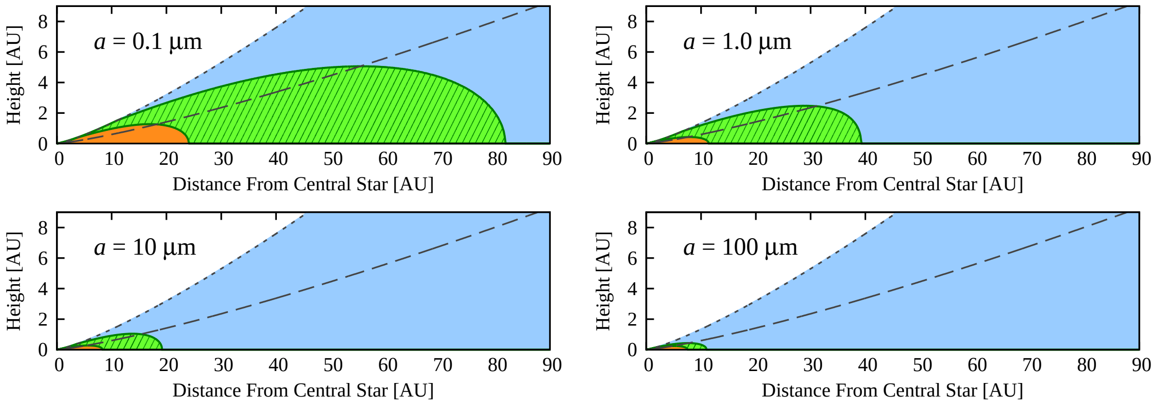

Figure 3.6: Same as Figure 3.3, but for different values of the grain size a.

0.1 μm and 100 μm. We can see that the e-heating zone shrinks with increasing grain size. On increasing a by a factor of 10, the outer radius of the e-heating zone decreases by a factor of ≈ 2. Qualitatively, this is simply because the ionization fraction of the gas increases with decreasing total surface area of the grains. Equation (3.20) shows that the electron abundance $x_e = n_e/n_n$ in equilibrium is inversely proportional to the total surface area of grains per unit volume $4\pi a^2 n_d$ as long as adsorption of plasma particles onto the grains dominate over gas-phase recombination. When dust grains aggregate, their total surface area decreases inversely proportional to a, and hence the electron abundance increases linearly with a. The resulting increase in the electric conductivity causes a shift of the J–E curve toward higher J, enabling the curve to cross the $J = J_{\rm max}$ line at smaller orbital radii. We also find that the outer radius of the dead zone decreases at a similar rate to that of the e-heating zone when we go from $a = 0.1$ μm to 1 μm. However, the decrease in the dead zone size stops beyond this grain size because gas-phase recombination takes over plasma adsorption onto dust grains. As a consequence, the e-heating zone becomes narrower and narrower as a increases beyond 10 μm.

Decreasing the dust-to-gas mass ratio f_{dg} has a similar effect to increasing the grain radius because the total surface area of the grains is linearly proportional to f_{dg}. This can be seen in Figure 3.7, where we show the location of the dead and e-heating zones for $a = 0.1$ μ with f_{dg} varying between 10^{-1} and 10^{-4}. We see that the outer radii of the active and e-heating zone decrease by a factor of ≈ 2 when f_{dg} is decreased by a factor of 10. This trend is similar to what we have seen when increasing the grain

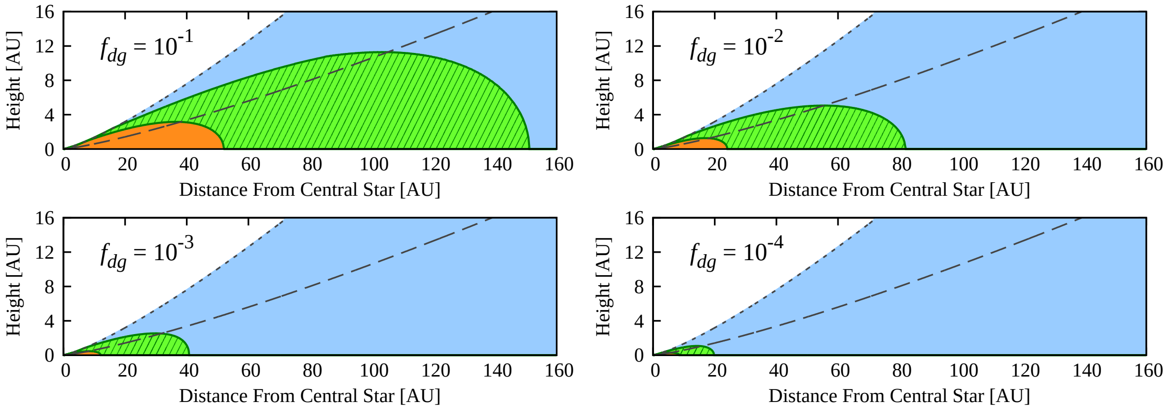

Figure 3.7: Same as Figure 3.3, but for different values of the dust-to-gas mass ratio f_{dg}.

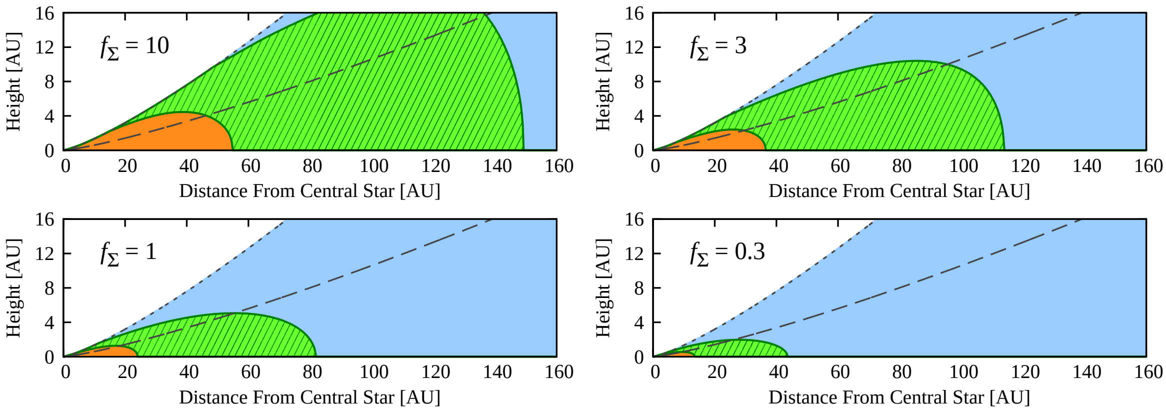

Figure 3.8: Same as Figure 3.3, but for different values of the surface density scaling factor f_Σ.

radius by the same factor.

3.3.4 Dependence on the Disk Mass

Finally, we examine how the size of the e-heating zone depends on the disk mass. Figure 3.8 shows the location of the e-heating zone for different values of f_Σ. Here, we fix the dust-to-gas mass ratio f_Σ so that both the gas and dust densities scale with f_Σ. We find that the e-heating zone expands toward larger orbital radii and higher altitudes as f_Σ increases. In the horizontal direction, the expansion is mainly due to the increased amount of dust grains with increasing f_Σ. As we have explained in 3.3.3, the ionization fraction of the gas scales inversely with $4\pi a^2 n_d$, and hence with f_Σ. Therefore, increasing f_Σ by a factor has the same effect as increasing f_{dg} by the same factor as long as the

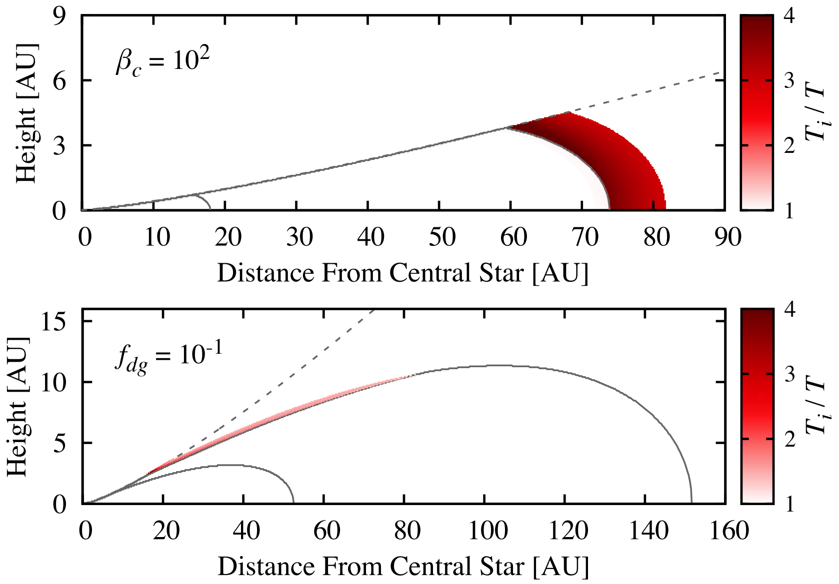

Figure 3.9: Two-dimensional distribution of the ion temperature T_i for the $\beta_c = 100$ model (upper panel) and $f_{dg} = 0.1$ model (lower panel). The solid lines show the boundary of the e-heating zone, while the dotted lines show H_{ideal}.

ionization rate ζ is unchanged (which is approximately true at ~ 100 AU where cosmic rays penetrate down to the midplane). This is exactly what we see in Figures 3.7 and 3.8, where the e-heating zone expands to 150 AU when either f_{dg} or f_Σ is increased by the factor of 10 from the fiducial value. By contrast, the vertical expansion of the e-heating zone is caused by the attenuation of X-rays that occurs at higher altitudes with increasing gas column density.

3.3.5 Ion Heating

We observe ion heating in two cases where $\beta_c = 100$ and where $f_{dg} = 0.1$. Figure 3.9 plots the distribution of the ion temperature T_i in the saturated state for these cases. In the case of $\beta_c = 100$ (the upper panel of Figure 3.9), T_i is 3–4 times higher than the temperature in a region slightly outside the e-heating zone. In this case, the Elsasser number Λ exceeds unity even after electron heating reduces Λ. This allows the electric field strength to reach the critical value for ion heating ($\approx 10^3 E_{\mathrm{crit}}$) in the vicinity of the e-heating zone. In the case of $f_{dg} = 0.1$ (the lower panel of Figure 3.9), ion heating takes place near the upper boundary of the e-heating zone. However, the region is very narrow, and the temperature rise is less than $2T$. Therefore, in this case, ion heating

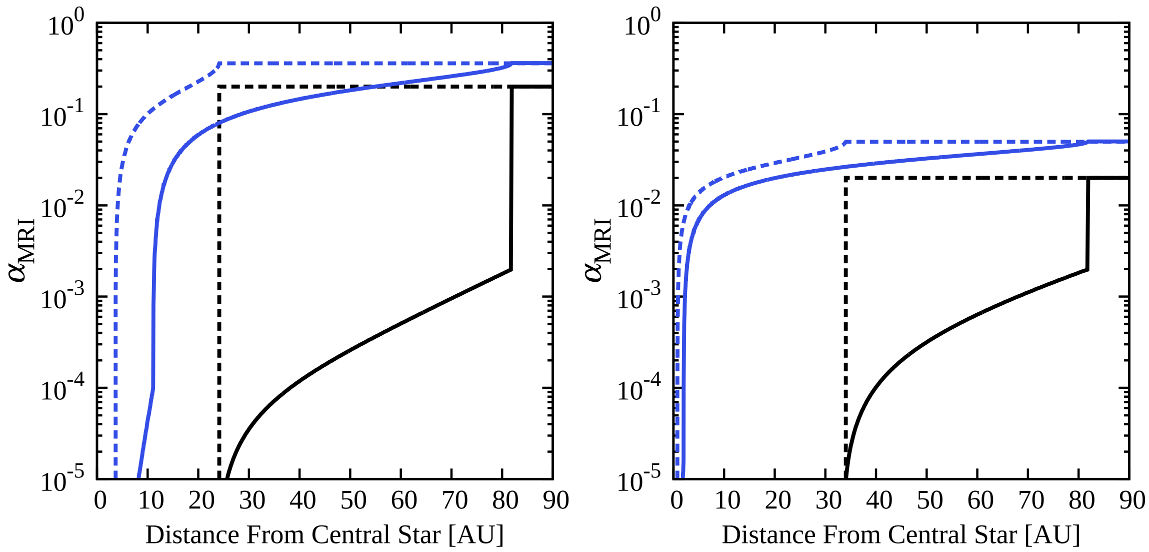

Figure 3.10: Radial distribution of $\alpha_{\rm MRI}$ (Equation (3.40)) for the fiducial model (left panel) and $\beta_c = 10^4$ (right panel). The solid black line shows $\alpha_{\rm MRI,mid}$ including electron heating on the mid-plane, and the solid blue line shows $\bar{\alpha}_{\rm MRI}$ including electron heating integrated in the z-direction. The dashed black line shows $\alpha_{\rm MRI,mid}$ without including electron heating on the mid-plane, and the dashed blue line shows $\bar{\alpha}_{\rm MRI}$ without including electron heating integrated in the z-direction.

might be practically negligible.

3.4 Saturation of Turbulence in the E-heating Zone

We have shown in Section 3.3 that self-regulation of the MRI due to electron heating can occur over a large region of protoplanetary disks. Then the question arises how strongly the e-heating will suppress the MRI turbulence in the e-heating zones. This question can only be fully addressed with MHD simulations including magnetic diffusion and electron heating in a self-consistent manner, which is far beyond the scope of this study. In this section, we attempt to estimate the saturation level of MRI turbulence from simple scaling arguments.

As usual, we quantify the strength of turbulence with the Shakura–Sunyaev α parameter $\alpha = T_{r\phi}/P$, where $P = \rho c_{\rm s}^2$ is the gas pressure and $T_{r\phi}$ is the $r\phi$ component of turbulent stress. In MRI-driven turbulence, $T_{r\phi}$ is generally dominated by the turbulent Maxwell stress $-\delta B_r \delta B_\phi/4\pi$ (Hawley et al., 1995; Miller & Stone, 2000), where δB_r and δB_ϕ are the radial and azimuthal components of the turbulent (fluctuating) magnetic fields.

Therefore, we evaluate the α parameter for MRI turbulence as

$$\alpha_{\rm MRI} \approx -\frac{\delta B_r \delta B_\phi}{4\pi\rho c_{\rm s}^2}. \tag{3.36}$$

In reality, the Reynolds stress (Fleming & Stone, 2003; Okuzumi & Hirose, 2011) or the coherent component of the Maxwell stress (e.g., Turner & Sano, 2008; Gressel et al., 2011) can dominate over the turbulent Maxwell stress at locations where the MRI is significantly suppressed. However, we do not include these components in our $\alpha_{\rm MRI}$ because they do not reflect the local MRI activity at such locations (see the references above).

Next we relate the amplitude of turbulent magnetic fields to the amplitude of the electric current density $J = |\boldsymbol{J}|$ using the Ampére 's law $\boldsymbol{J} = (c/4\pi)\nabla \times \delta\boldsymbol{B}$. We neglect large-scale, coherent components in $\boldsymbol{B}$ since the electric current is inversely proportional to the length scale of fields. We assume that the magnetic field in MRI-driven turbulence is dominated by the azimuthal component δB_ϕ and varies over a length scale $\sim \lambda_{\rm ideal}$, where $\lambda_{\rm ideal}$ is the wavelength of the most unstable MRI modes already introduced in Equation (3.29). Then, from the Ampére 's law, one can estimate the magnitude of the current density as

$$\begin{aligned} J &= \frac{c}{4\pi}|\nabla \times \boldsymbol{B}| \\ &\approx \frac{c}{4\pi}\frac{v_{Az}}{\Omega}\delta B_\phi = \sqrt{\frac{\rho}{4\pi}}c\Omega\frac{\delta B_\phi}{B_z}, \end{aligned} \tag{3.37}$$

where we have replaced the derivative ∇ with wavenumber $2\pi/\lambda_{\rm ideal} = \Omega/v_{Az}$. If we use the maximum current $J_{\rm max}$ for fully developed MRI turbulence (Equation (3.33)), Equation (3.37) results in a simple scaling relation

$$\frac{\delta B_\phi}{B_z} \approx 10\sqrt{2}\frac{J}{J_{\rm max}}. \tag{3.38}$$

For fully developed MRI turbulence where $J \approx J_{\rm max}$, the above equation predicts $\delta B_\phi/B_z \sim 10$, in agreement with the results of MHD simulations (e.g., Hawley et al., 1995; Sano et al., 2004).

Now let us consider situations where e-heating is so effective that the growth of the MRI is saturated at $J \approx J_{\Lambda=1} \ll J_{\max}$. Assuming $\delta B_z \lesssim B_{z0}$ for this case, we have

$$\delta B_\phi \approx 10\sqrt{2} B_{z0} \frac{J}{J_{\max}}. \tag{3.39}$$

This equation predicts the amplitude of δB_ϕ as a function of B_{z0} and $J/J_{\max}$. MHD simulations show that $\delta B_r \approx -(0.4 \ldots 0.6)\delta B_\phi$ in MRI turbulence (Hawley et al., 1995; Sano et al., 2004). Assuming that this scaling also holds in our case, we have $\delta B_r \delta B_\phi \approx -100 B_{z0}^2 (J/J_{\max})^2$. Finally, substituting this into Equation (3.36), we obtain the scaling relation between $\alpha_{\rm MRI}$ and $J/J_{\max}$,

$$\begin{aligned} \alpha_{\rm MRI} &\approx \frac{100 B_0^2}{4\pi\rho c_{\rm s}^2}\left(\frac{J}{J_{\max}}\right)^2 \\ &\approx 0.2\left(\frac{\beta_0}{1000}\right)^{-1}\left(\frac{J}{J_{\max}}\right)^2, \end{aligned} \tag{3.40}$$

where $\beta_0 \equiv 8\pi\rho c_{\rm s}^2/B_{z0}^2 = \beta_c \exp(-z^2/2H^2)$ is the plasma beta (not necessarily at the midplane) associated with the net vertical field B_{z0}. Formally, the derivation leading to Equation (3.40) breaks down when MRI is so active that $\delta B_z \gg B_{z0}$ and $J \approx J_{\max}$. Nevertheless, we find that Equation (3.40) reproduces the results of ideal MHD simulations with a reasonably good accuracy. Equation (3.40) predicts that $\alpha_{\rm MRI} \approx 2$ for $\beta_0 = 10^2$ and $\alpha_{\rm MRI} \approx 0.02$ for $\beta_0 = 10^2$ when $J = J_{\max}$. These are consistent with the results of isothermal simulations by Sano et al. (2004) showing that the Maxwell component of α is ~ 1 for $\beta_0 = 10^2$ and ~ 0.01 for $\beta_0 = 10^4$ (see their Table 2, column (10)). Therefore, we will apply Equation (3.40) to both the e-heating zone and active zone.

The left panel of Figure 3.10 show the radial distribution of $\alpha_{\rm MRI}$ for the fiducial disk model predicted from Equation (3.40). Here we plot the midplane value $\alpha_{\rm MRI,mid} \equiv \alpha_{\rm MRI}(z=0)$ and the density-weighted average in the vertical direction,

$$\bar{\alpha}_{\rm MRI} \equiv \frac{\int_{-H_{\rm ideal}}^{H_{\rm ideal}} \alpha_{\rm MRI}(z')\rho(z')dz'}{\Sigma}, \tag{3.41}$$

where we have assumed $\alpha_{\rm MRI} = 0$ in the magnetically dominated atmosphere at $|z| > H_{\rm ideal}$. The former quantity measures the MRI activity at the disk midplane, while the latter quantity is more closely related to the vertically integrated mass accretion rate

(Suzuki et al., 2010). For the fiducial disk model, we find that $\alpha_{\rm MRI,mid} \sim 10^{-5}$ and 10^{-3} at the inner and outer edge of the e-heating zone (20 AU and 80 AU), respectively. These values are more than two orders of magnitude lower than the value $\alpha_{\rm MRI,mid} = 0.2$ in the active zone ($r \gtrsim 80$ AU). This implies that the MRI is "virtually dead" deep inside the e-heating zone. We also find that $\alpha_{\rm MRI,mid}$ changes discontinuously at the boundary between the e-heating and active zones. The reason is that when the saturated state changes at the point, $J/J_{\rm max}$ also changes from unity to one order of magnitude because of the N-shaped current–field relation (see middle and right panels of Figure 3.4). The vertical average $\bar{\alpha}_{\rm MRI}$ decreases more slowly with decreasing r, because the upper layer of the disk remains MRI-active (see Figure 3.3). This picture is qualitatively similar to the classical layered accretion model of Gammie (1996). In right panel of Figure 3.10, we also plot the radial distribution of $\alpha_{\rm MRI,mid}$ and $\bar{\alpha}_{\rm MRI}$ for a disk with $\beta_c = 10^4$. We find that $\alpha_{\rm MRI,mid}$ in e-heating zone is almost unchanged from the fiducial disk. The reason is that increase of $(J/J_{\rm max})^2 \approx 10$ cancels out the depletion of $\beta_c^{-1} \approx 10^{-1}$ in Equation (3.40). Therefore, $\alpha_{\rm MRI,mid}$ remains low saturation level.

In summary, our simple estimate predicts that MRI turbulence can be significantly suppressed in the e-heating zone. In this sense, the e-heating zone acts as a extended dead zone. However, our estimate relies on the hypothetical scaling between the and turbulent Maxwell stress and $J/J_{\rm max}$, which is as yet justified by MHD simulations. [1] In order to test our prediction, we will perform resistive MHD simulations including electron heating in future work.

3.5 Charge Barrier against Dust Growth in the E-heating Zone

So far we have focused on the role of electron heating on the saturation of MRI turbulence. As pointed out by OI15, electron heating also has an important effect on the

[1] However, there are some support for Equation (3.40) from MHD simulations including ambipolar diffusion, not Ohmic dissipation. Bai & Stone (2011) reported the Maxwell component of α (their Table 2) and the cumulative probability distribution of J (Figure 6) for three simulation runs with $\beta_0 = 400$ and with different values of ambipolar diffusivity. Their results show that $\alpha_{\rm Maxwell} \approx 0.17$, 0.029, and 0.0041 for models with $J/J_{\rm max} \approx 1, 0.3$, and 0.1 (median values), respectively. These are consistent with Equation (3.40) predicting that $\alpha_{\rm MRI} \approx 0.5$, 0.045, and 0.005 for these values of $J/J_{\rm max}$.

growth of dust grains. In an ionized gas, dust grains tend to be negatively charged because electrons collide and stick to dust grains more frequently than ions. The resulting Coulomb repulsion slows down the coagulation of the grains through Brownian (thermal) motion. This "charge barrier" is also present in weakly ionized protoplanetary disks, in which dust grains tend to be charged as in a fully ionized gas when their size is larger than 1 μ (Okuzumi, 2009; Matthews et al., 2012). The important role of electron heating in this context is that heating electrons further promote the negative charging of the grains, because the grain charge in a plasma is linearly proportional to the electron temperature (e.g., Shukla & Mamun, 2002). In this section, we explore how this affects dust coagulation in the e-heating zone.

For simplicity, let us assume that dust grains have the single radius a and charge Z. The grains can collide with each other if the condition

$$\mathcal{E}_{\rm col} > \mathcal{E}_{\rm elc} \tag{3.42}$$

is satisfied (Okuzumi, 2009). Here, $\mathcal{E}_{\rm col}$ is the kinetic energy of the relative motion of two colliding grains, and

$$\mathcal{E}_{\rm elc} \approx \frac{(eZ)^2}{2a} \tag{3.43}$$

is the Coulomb repulsion energy of the grains just before contact. We focus on small dust grains near the midplane and assume that the relative motion is dominated by Brownian motion and turbulence-induced motion. Then, the kinetic energy of relative motion can be expressed as

$$\mathcal{E}_{\rm col} = \mathcal{E}_{\rm Brown} + \mathcal{E}_{\rm turb}, \tag{3.44}$$

where $\mathcal{E}_{\rm Brown}$ and $\mathcal{E}_{\rm turb}$ are the kinetic energy of Brownian motion and turbulence-induced motion, respectively. Brownian motion is the thermal motion of grains, and $\mathcal{E}_{\rm Brown}$ is approximately expressed as

$$\mathcal{E}_{\rm Brown} \approx \frac{1}{2}\mu u_{\rm th}^2, \tag{3.45}$$

where the thermal velocity of grains $u_{\rm th}$ is expressed as $u_{\rm th} = \sqrt{8kT/\pi m}$ and the reduced mass of grains μ is expressed as $\mu = m^2/(m+m) = m/2$. The relative energy of turbulence-induced motion is expressed as

$$\mathcal{E}_{\rm turb} \approx \frac{1}{2}\mu(\Delta u_{\rm turb})^2, \tag{3.46}$$

where $\Delta u_{\rm turb}$ is the relative velocity of the grains excited by turbulence. For small grains, $\Delta u_{\rm turb}$ is approximately given by (Weidenschilling, 1984; Ormel & Cuzzi, 2007)

$$\Delta u_{\rm turb} \approx \sqrt{\alpha_{\rm disp}}{\rm Re}^{1/4} c_{\rm s}\Omega\tau_s, \tag{3.47}$$

where $\alpha_{\rm disp} \equiv \langle \delta v^2 \rangle / c_{\rm s}^2$ is the velocity dispersion of the gas $\langle \delta v^2 \rangle$ normalized by $c_{\rm s}^2$, Re is the Reynolds number of turbulence, and

$$\tau_s = \rho_\bullet a / (\sqrt{8/\pi} c_{\rm s}\rho) \tag{3.48}$$

is the stopping time of the grains (we have adopted Epstein's drag law for τ_s). The Reynolds number is expressed as ${\rm Re} = \alpha_{\rm disp} c_{\rm s}^2 \Omega^{-1}/\nu_{\rm mol}$, where $\nu_{\rm mol}$ is the molecular viscosity. We estimate α with and without electron heating, using Equation (3.40) presented in Section 3.4. Turbulence dominates the collisional energy when $\alpha_{\rm disp}$ is high and/or a is large. For the moment, we simply assume $\alpha_{\rm disp} = \alpha_{\rm MRI}$, where $\alpha_{\rm MRI}$ is the normalized local Maxwell stress introduced in Equation (3.36). This assumption holds when the Reynolds stress in the e-heating zone is comparable to the Maxwell stress. In reality, the Reynolds stress in the e-heating zone might be higher than the Maxwell stress for a reason discussed later. Therefore, the estimate of $\mathcal{E}_{\rm turb}$ presented here should be taken as a lower limit.

To obtain Z and $\alpha_{\rm MRI}$, we calculate the ionization fraction (Section 3.1.3), determine the turbulent state (Section 3.2.2), and estimate the MRI-turbulent viscosity (Section 3.4) with changing grain radius a at a location. We then obtain $\mathcal{E}_{\rm col}$ and $\mathcal{E}_{\rm elc}$ by above-mentioned method. It should be noted that grains have single size and changing grain radius means changing the size of all grains at the location. Thus, the turbulent state at the location also depends on a.

In Figure 3.11, we plot the ratio $\mathcal{E}_{\rm elc}/\mathcal{E}_{\rm col}$ as a function of a at 35 AU in the midplane for the fiducial disk model. The ratio quantifies the effectiveness of the charge barrier: the

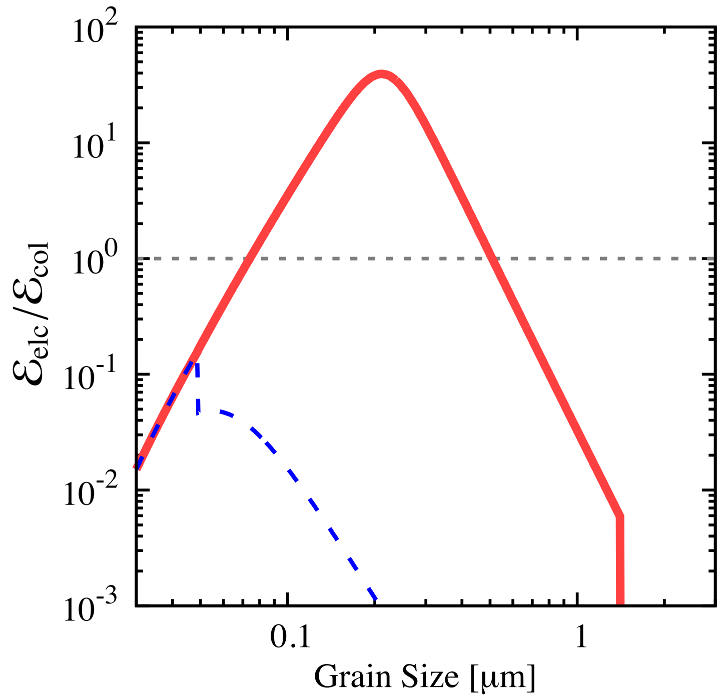

Figure 3.11: Effectiveness of the charge barrier against grain growth as a function of the grain size at the midplane 35 AU in the fiducial model. The solid line (red) shows $\mathcal{E}_{\rm elc}/\mathcal{E}_{\rm col}$ including electron heating, and the dashed line (blue) shows $\mathcal{E}_{\rm elc}/\mathcal{E}_{\rm col}$ without including electron heating. The horizontal dotted line shows $\mathcal{E}_{\rm elc}/\mathcal{E}_{\rm coll} = 1$, above which a strong Coulomb repulsion between the grains suppresses their mutual collision cross section. Here it is assumed that $\alpha_{\rm disp}(= \langle \delta v^2 \rangle / c_{\rm s}^2)$ is equal to $\alpha_{\rm MRI}$, the normalized local Maxwell stress given by Equation (3.36) (but see also Figure 3.12).

collisional cross section of two equally charged grains is significantly suppressed when $\mathcal{E}_{\rm elc}/\mathcal{E}_{\rm col} \gg 1$. We find that electron heating significantly enhances the charge barrier for submicron-sized grains. If electron heating is not included, this location belong to the dead zone and the active zone with grain size being $\lesssim 0.05$ μm and $\gtrsim 0.05$ μm, respectively. In this case, $\mathcal{E}_{\rm elc}/\mathcal{E}_{\rm col}$ is much lower than unity in all a. Thus we can conclude that dust grains at this location can grow without the charge barrier. On the other hand, if electron heating is included, this location belongs to the e-heating zone when 0.05 μm $\lesssim a \lesssim 1.4$ μm (see also Figure 3.6). In the e-heating zone, grains are charged by heated electrons, leading to increase of $\mathcal{E}_{\rm elc}$, and MRI turbulence as collisional source is well suppressed, leading to decrease of $\mathcal{E}_{\rm turb}$. Consequently, $\mathcal{E}_{\rm elc}/\mathcal{E}_{\rm col}$ is larger than unity when 0.08 μm $\lesssim a \lesssim 0.5$ μm. In particular, $\mathcal{E}_{\rm elc}/\mathcal{E}_{\rm col}$ takes its maximum value of 40 at $a = 0.2$ μm corresponding to $\mathcal{E}_{\rm Brown} = \mathcal{E}_{\rm turb}$. Both the suppression of turbulence and grain charge would enhance the charge barrier.

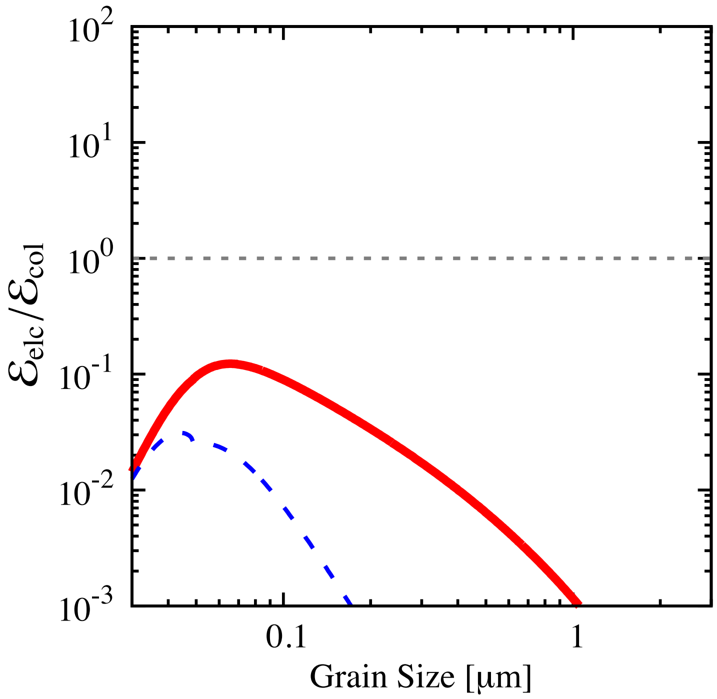

Figure 3.12: Same as Figure 3.11, but we here evaluate $\alpha_{\rm disp} = \langle \delta v^2 \rangle / c_{\rm s}^2$ using Equation (3.49) assuming that sound waves propagate from upper MRI active layers to the midplane as it is observed for the conventional dead zone.

There are at least two mechanisms that could drive further growth of dust in the e-heating zone. One is vertical turbulent mixing of dust particles as already pointed out by Okuzumi et al. (2011). In general, the charge barrier is less significant at higher altitudes where dust particles have a higher collision energy due to vertical settling (and due to if MRI is active there). Electron heating, which was not considered by Okuzumi et al. (2011), does not change this picture because it is also ineffective at high altitudes. Micron-sized grains in the e-heating zone can easily be lifted up to such high altitudes if only weak turbulence is present there (Turner et al., 2010, see also dust scale height H_d in Section 3.6.1). The lifted grains are allowed to collide and grow there until they fall back to the e-heating zone. In this way, small grains in the e-heating zone are able to continue growing on a timescale much longer than vertical diffusion timescale. Okuzumi et al. (2011) showed that the charge barrier is overcome on a timescale of 10^5–10^6 yr, but they did not consider the amplification of grain charging due to electron heating. How much the growth is delayed in the presence of electron heating should be studied in future work.

Another potentially important mechanism is dust stirring by random sound waves. It is known that the Reynolds stress in a dead zone exceeds the Maxwell stress because of sound waves propagating from upper MRI-active layers (e.g., Fromang & Papaloizou, 2006; Turner et al., 2010; Okuzumi & Hirose, 2011). If this is also the case for our e-heating zone, the assumption $\alpha_{\rm disp} = \alpha_{\rm MRI}$ would significantly underestimate the particle collision energy in the e-heating zone. To estimate this effect, we now calculate $\alpha_{\rm disp}$ using an empirical formula for the gas velocity dispersion in the dead zone (Okuzumi & Hirose, 2011),

$$\langle \delta v^2 \rangle \approx 0.78 \bar{\alpha}_{\rm MRI} c_{\rm s}^2 \exp\left(\frac{z^2}{2H^2}\right), \tag{3.49}$$

where $\bar{\alpha}_{\rm MRI}$ is the density-weighted vertical average of $\alpha_{\rm MRI}$ defined by Equation (3.41). Equation (3.49) expresses the amplitude of random sound waves inside a dead zone. Figure 3.12 shows $\mathcal{E}_{\rm elc}/\mathcal{E}_{\rm col}$ in this case and is obtained in the same way as in Figure 3.11 but we here use Equation (3.49) for $\alpha_{\rm disp}$ in Equation (3.47). The use of Equation (3.47) for the sound wave-driven collision velocity assumes that the time correlation of the waves' velocity fluctuations exponentially decays on the timescale of Ω^{-1} as in the Kolmogorov turbulence. We find that $\mathcal{E}_{\rm elc}/\mathcal{E}_{\rm col}$ now falls below unity at all grain sizes. Thus, sound waves traveling from MRI-active layers, if they exist, could help dust overcome the charge barrier in the e-heating zone. However, the argument made here is not conclusive because the induced collision velocity depends on the assumed time correlation function, or equivalently power spectrum, of the random sound waves. If the power spectrum of the waves has only a small amplitude at high frequencies (to which small dust particles are sensitive) compared to the turbulent spectrum, the wave-induced collision velocity would be lower than given by Equation (3.47). The spectrum of velocity fluctuations in the e-heating zone should be studied in future MHD simulations.

3.6 Discussion

3.6.1 Dust Diffusion

We have assumed so far that the dust-to-gas mass ratio is vertically constant. This assumption breaks down when dust particles settle toward the midplane. If this is the case, the dust-to-gas ratio would decrease at high altitudes, and consequently the e-heating zone would shrink in the vertical direction as expected from Figure 3.7.

However, as we will show below, dust settling is negligible even in the e-heating zone because even weak turbulence is able to diffuse small grains to high altitudes. Youdin & Lithwick (2007) analytically derived dust scale height H_d in the sedimentation-diffusion equilibrium. If the particle stopping time τ_s is much smaller than the Keplerian timescale Ω^{-1}, which is true for small particles, the dust scale height can be approximately written as

$$H_d \approx H \left(1 + \frac{\mathrm{St}}{\alpha_{\mathrm{disp},z}}\right)^{-1/2}, \tag{3.50}$$

where $\mathrm{St} = \tau_s \Omega$ is the so-called Stokes number and $\alpha_{\mathrm{disp},z} = \langle \delta v_z^2 \rangle / c_s^2$ is the vertical component of the velocity dispersion normalized by c_s^2. Equation (3.50) implies that dust settling takes place ($H_d < H$) when $\mathrm{St} > \alpha_{\mathrm{disp},z}$. Under the disk model employed in this study, St can be expressed as

$$\mathrm{St} = 3 \times 10^{-8} \left(\frac{a}{0.1\ \mu\mathrm{m}}\right) f_\Sigma^{-1} \left(\frac{r}{1\ \mathrm{AU}}\right)^{3/2} \exp\left(\frac{z^2}{2H^2}\right). \tag{3.51}$$

Therefore, for $a = 0.1\ \mu$, dust settling in the e-heating zone ($r \sim 10$–$100\,\mathrm{AU}$) occurs only if $\alpha_{\mathrm{disp},z} \lesssim 10^{-5}$–$10^{-6}$. In the e-heating zone, $\alpha_{\mathrm{MRI}} \sim 10^{-5}$–$10^{-3}$ at the midplane (see Figure 3.10), and therefore we may safely neglect dust settling even if the Reynolds stress is as small as the Maxwell stress ($\alpha_{\mathrm{disp},z} \sim \alpha_{\mathrm{MRI}}$). A larger a does not change this conclusion, because we then would have a higher α_{MRI} or the e-heating zone would vanish.

3.6.2 Effects of Grain Size Distribution and Porosity

We have characterized dust grains with a single particle size a assuming that the size distribution of dust grains is narrow. Under this assumption, the e-heating zone covers only a small part of protoplanetary disks when the particles grow to millimeter sizes (see Figure 3.6). However, caution is required in applying our results to more general cases where particles have a size distribution. In such cases, the smallest grains tend to dominate the total surface area of dust (which controls the ionization balance), whereas the largest grains tend to dominate the total mass of dust, simply because smaller grains have a larger area-to-mass ratio. Therefore, it is not obvious what the typical particle size is in these cases.

Here we discuss more quantitatively how we can apply the results of single-size calculations to cases with a size distribution. Let us assume that the particle size distribution is given by the power-law form

$$\frac{dn_d}{da} = \frac{3\rho f_{dg}}{8\pi\rho_\bullet\sqrt{a_{\rm max}}}a^{-3.5} \tag{3.52}$$

with $a_{\rm min} < a < a_{\rm max}$ ($a_{\rm min} \ll a_{\rm max}$), where dn_d/da is the number density of dust particles per unit particle radius, and $a_{\rm min}$ and $a_{\rm max}$ are the minimum and maximum particle sizes, respectively. The distribution is normalized so that that the total particle mass density $\int m_d(dn_d/da)da$ becomes equal to ρf_{dg}. Equation (3.52) applies when the particle size distribution is determined by fragmentation cascade (Dohnanyi, 1969) and is also known to reproduce the size distribution of interstellar dust grains (Mathis et al., 1977). The quantity we are interested in is the total surface area of the particles as it mainly determines the ionization balance in a gas–dust mixture (e.g., Sano et al., 2000). This can be calculated as

$$\int_{a_{\rm min}}^{a_{\rm max}} 4\pi a^2\frac{dn_d}{da}da \approx \frac{3\rho f_{dg}}{\rho_\bullet}\frac{1}{\sqrt{a_{\rm min}a_{\rm max}}}. \tag{3.53}$$

Note that the factor $1/\sqrt{a_{\rm min}}$ comes from the fact that the integration in Equation (3.53) is dominated by the smallest particles (because $a^2(dn_d/da)da \propto d(a^{-0.5})$), whereas the factor $1/\sqrt{a_{\rm max}}$ from the fact that the total mass is dominated by the largest particles.

By contrast, if all dust particles have a single size $a_{\rm single}$, their total surface area is $4\pi a_{\rm single}^2 n_{d,{\rm single}} = 3\rho f_{dg}/(\rho_\bullet a_{\rm single})$. Comparing this with Equation (3.53), we find that the total surface area of particles whose size distribution is given by Equation (3.52) is equal to that of single-size particles if

$$a_{\rm single} = \sqrt{a_{\rm min} a_{\rm max}}. \tag{3.54}$$

Since the total surface area approximately determines the ionization state, Equation (3.54) may be used to generalize the results presented in this study to the cases where the particle size distribution obeys Equation (3.52).

Observations of millimeter dust emission from protoplanetary disks suggest that the largest dust particles in the disk have a size of centimeters (e.g., Testi et al., 2003; Natta et al., 2004; Rodmann et al., 2006; Ricci et al., 2010). Assuming $a_{\rm max} = 1$ cm and $a_{\rm min} = 0.1\ \mu$m, we obtain $a_{\rm single} = 30\ \mu$m. In this case, we expect from Table 3.1 that the e-heating zone extends to ~ 15 AU. Thus, even if cm-sized grains exist in protoplanetary disks and the total mass of grains is dominated by such large grains, the e-heating zone can be present in the disks.

For the same reason, large dust particles can alone provide a large e-heating zone if the dust particles are highly fluffy aggregates of tiny grains. Okuzumi (2009) showed that the ionization balance is insensitive to the particle radius when the fractal dimension is ≈ 2, for which the total surface area of the aggregates is approximately conserved during the aggregation process.

3.6.3 Hall Effect and Ambipolar Diffusion

The plasma heating model employed in this study neglects the effects of magnetic fields on the motion of plasma particles. In terms of non-ideal magnetohydrodynamics, this is equivalent to neglecting ambipolar diffusion and Hall effect (see, e.g., Wardle, 1999). A full treatment of these non-Ohmic effects introduces to the model additional complexities arising from the relative angle between the magnetic and electric fields (Okuzumi, Mori, & Inutuska, in prep.), which is beyond the scope of this work. In

Table 3.2: Am and Ion Abundance x_i in E-heating Zone for Various Parameter Sets

β_c	a (μm)	f_{dg}	f_Σ	Am in e-heating zone		x_i in e-heating zone	
				Inner edge	Outer edge	Inner edge	Outer edge
10^2	0.1	10^{-2}	1	0.14	0.56	1.9×10^{-12}	4.7×10^{-11}
10^3	0.1	10^{-2}	1	0.17	0.62	3.4×10^{-12}	5.9×10^{-11}
10^4	0.1	10^{-2}	1	0.23	0.62	7.4×10^{-12}	5.9×10^{-11}
10^5	0.1	10^{-2}	1	0.41	0.62	2.5×10^{-11}	5.9×10^{-11}
10^3	0.1	10^{-2}	1	0.17	0.62	3.4×10^{-12}	5.9×10^{-11}
10^3	1	10^{-2}	1	0.21	0.72	1.7×10^{-12}	2.8×10^{-11}
10^3	10	10^{-2}	1	0.43	0.82	2.3×10^{-12}	1.3×10^{-11}
10^3	100	10^{-2}	1	0.54	0.72	2.6×10^{-12}	5.6×10^{-12}
10^3	0.1	10^{-1}	1	0.16	0.57	8.5×10^{-12}	1.2×10^{-10}
10^3	0.1	10^{-2}	1	0.17	0.62	3.4×10^{-12}	5.9×10^{-11}
10^3	0.1	10^{-3}	1	0.24	0.71	2.1×10^{-12}	2.8×10^{-11}
10^3	0.1	10^{-4}	1	0.41	0.80	2.3×10^{-12}	1.3×10^{-11}
10^3	0.1	10^{-2}	10	0.32	1.26	1.8×10^{-12}	2.5×10^{-11}
10^3	0.1	10^{-2}	3	0.22	0.82	2.5×10^{-12}	3.9×10^{-11}
10^3	0.1	10^{-2}	1	0.17	0.62	3.4×10^{-12}	5.9×10^{-11}
10^3	0.1	10^{-2}	0.3	0.16	0.65	5.4×10^{-12}	9.5×10^{-11}

this subsection, we only briefly discuss how plasma heating and these non-ideal MHD effects could affect each other.

Ambipolar diffusion can suppress MRI in low density regions of protoplanetary disks (e.g., Blaes & Balbus, 1994; Hawley & Stone, 1998; Kunz & Balbus, 2004; Desch, 2004; Bai & Stone, 2011; Simon et al., 2013a,b). If MRI is effectively suppressed in the e-heating zone, electric fields may not sufficiently grow to cause electron heating. The effectiveness of ambipolar diffusion is characterized by the ambipolar Elsasser number $\mathrm{Am} = \gamma_i\rho_i/\Omega$ (e.g., Blaes & Balbus, 1994; Lesur et al., 2014), where $\gamma_i = \langle\sigma_{in}v_{in}\rangle/(m_n+m_i)$ and $\rho_i = m_i n_i$. According to MHD simulations including ambipolar diffusion, MRI-driven turbulence behaves as in the ideal MHD limit if $\mathrm{Am} \gg 1$, while ambipolar diffusion suppresses turbulence if $\mathrm{Am} \ll 1$ (e.g., Bai & Stone, 2011). Table 3.2 lists the values of Am as well as the ion abundance $x_i = n_i/n_n$ at the inner and outer edges of the e-heating zone before electron heating sets in ($E = 0$). We find that $\mathrm{Am} \approx$ 0.2–0.7, implying that ambipolar diffusion would moderately affect MRI turbulence in the e-heating zone. Therefore, MHD simulations including both electron heating and ambipolar diffusion are needed to assess which effect determines the saturation amplitude of MRI turbulence in these outer regions of the disks.

The Hall effect is also important at $r \sim 10$–$50\,\mathrm{AU}$ (see Figure 1 of Turner et al., 2014). The Hall effect can either damp or amplify magnetic fields, which depends on the relative orientation between the disk's magnetic field and rotation axis and on the sign of the Hall conductivity (e.g., Bai, 2014; Wardle & Salmeron, 2012). At relatively high gas densities ($n_n \gtrsim 10^{10}\ \mathrm{cm}^{-3}$), the Hall conductivity is usually positive (Wardle & Ng, 1999; Nakano et al., 2002; Salmeron & Wardle, 2003), but can become negative when the number density of electrons is significantly lower than that of ions. Interestingly, our preliminary investigation shows that the Hall conductivity can indeed become negative as the electron number density is decreased by electron heating (Okuzumi et al., in prep.). This suggests that electron heating might reverse the role of the Hall term. Whether this occurs under conditions relevant to protoplanetary disks will be studied in future work.

Chapter 4

Suppression of MRI by the Electron Heating

In this chapter, we perform MHD simulations to investigate an effect of the electron heating on the nonlinear evolution of MRI. Our previous study (Mori & Okuzumi, 2016, or see previous chapter) have investigated the extent where the electron heating takes place. They found that the electron heating is effective in a large region of protoplanetary disks. Electron heating evoked by a strong electric field of MRI turbulence reduces the ionization fraction. When ionization fraction is sufficiently low, MRI is stabilized. Thus, the electron heating has potential to suppress the MRI. We have also estimated how electron heating can weaken the MRI turbulence. Then, we found the turbulence can be largely suppressed. However, the estimation is based on only a scaling relation between magnetic turbulence stress and current density. Thus, the detailed effects of electron heating on the turbulence strength is still not obvious. In addition, the nonlinear evolution of MRI is also unknown. This paper first performs MHD simulations including electron heating. Our goal in this work is to quantify the effect of electron heating on MRI. We investigate whether the scaling relation exists or not and if so, how much the electron heating suppresses the turbulence strength depending on current density. In this chapter, for simple analysis of the increasing resistivity by electron heating, we neglect the nonideal MHD effects other than Ohmic dissipation.

First, in Section 4.1, we present the numerical setup and procedure in our simulations.

In Section 4.2, we then show some results and present the interpretations. Finally, in Section 4.3, we analytically derive a relation between current density and Maxwell stress.

4.1 Numerical Setup and Procedure

We adopt a local shearing box whose center is located at a distance from the central star r_0. The coordinates x, y, and z are radial, azimuthal, and vertical axis, respectively. We numerically solve the following MHD equations (the equation of continuity, the equation of motion, and Faraday's equation)

$$\begin{aligned} \frac{\partial \rho}{\partial t} + \nabla \cdot (\rho \boldsymbol{v}) &= 0, && (4.1) \\ \frac{\partial \boldsymbol{v}}{\partial t} + (\boldsymbol{v} \cdot \nabla) \boldsymbol{v} &= -2\boldsymbol{\Omega} \times \boldsymbol{v} + 3\Omega^2 x \boldsymbol{e}_x - \frac{1}{\rho}\nabla\left(P + \frac{B^2}{8\pi}\right) + \frac{1}{4\pi\rho}\left(\boldsymbol{B}\cdot\nabla\boldsymbol{B}\right), && (4.2) \\ \frac{\partial \boldsymbol{B}}{\partial t} &= -c\nabla \times \boldsymbol{E}, && (4.3) \end{aligned}$$

where $\boldsymbol{v}$ is the gas velocity, ρ is the mass density, P is the gas pressure, Ω is the angular velocity at r_0, $\boldsymbol{B}$ is the magnetic field, $\boldsymbol{E}$ is the electric field, and c is the speed of light. In this chapter, we assume the isothermal change of gas and use the isothermal equation of state,

$$P = c_{\mathrm{s}}^2 \rho. \tag{4.4}$$

Electric field $\boldsymbol{E}$ is given by

$$\boldsymbol{E} = \frac{4\pi\eta(E')}{c^2}\boldsymbol{J} - \frac{1}{c}\boldsymbol{v} \times \boldsymbol{B}. \tag{4.5}$$

Here, we have used the Ohm's law in comoving frame,

$$\boldsymbol{J}' = \frac{c^2}{4\pi\eta(E')}\boldsymbol{E}', \tag{4.6}$$

and the Lorentz transformation of current density J,

$$\boldsymbol{J}' = \boldsymbol{J}, \tag{4.7}$$

where the $'$ means values in the comoving frame. In this chapter, since we use our resistivity model instead of usual constant resistivity, the dependence of the resistivity on electric field strength is explicitly expressed. Adopting the same formula of MO16, we use the electric field in the comoving frame. In our simulations, for electric field, we express it only in a comoving frame in order to simply derive electric fields, $E' = \eta J$. In Section 4.2, note that we omit the superscript $'$ of electric field strength.

The relation between current density and electric field including electron heating (nonlinear Ohm's law) has N-shape (see Figure 10 of OI15; see also Figure 3.4). In MHD formulation, electric field is obtained from the current density via the Ohm's law. However, under the nonlinear Ohm's law, we obtain multiple values of electric fields when a current density is given. Thus, in the MHD simulation, we cannot exactly treat the nonlinear Ohm's law. In this work, we focus on only the resistivity increased by electron heating but does not address an effect of the complex N-shaped Ohm's law. An exact treatment of Ohm's law is beyond the scope of this work.

To include the increase of resistivity by electron heating, we introduce a analytical resistivity model depending on E. From above the reason, mimicking the nonlinear Ohm's law, we give the simple analytical resistivity model where the resistivity increases but does not drops current density with increase of E during electron heating. Figure 4.1 shows the schematic diagram. Specific formula of the resistivity is expressed as

$$J' = \begin{cases} \dfrac{c^2}{4\pi\eta_0} E', & E' < E_{\rm EH}, \\ \dfrac{c^2}{4\pi\eta_0} \left(\dfrac{E'}{E_{\rm EH}}\right)^{\gamma-1} E', & E' > E_{\rm EH}, \end{cases} \tag{4.8}$$

or

$$E' = \begin{cases} \dfrac{4\pi\eta_0}{c^2} J', & J' < J_{\rm EH}, \\ \dfrac{4\pi\eta_0}{c^2} \left(\dfrac{J'}{J_{\rm EH}}\right)^{1/\gamma\ -1} J', & J' > J_{\rm EH}. \end{cases} \tag{4.9}$$

where γ is a constant value sufficiently less than unity, $E_{\rm EH}$ is an electric fields strength

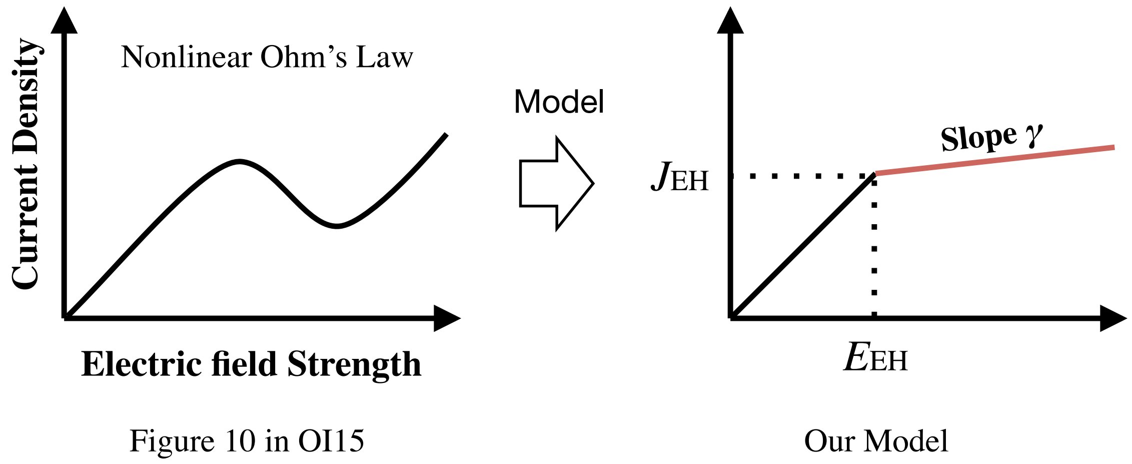

Figure 4.1: Schematic diagram of modeling our J–E relation after the nonlinear Ohm's law. We neglect the N-shape of the nonlinear Ohm's law. Instead, we give the shallow inclination of J–E relation during electron heating. In this model, the resistivity increases with increase of E.

when electron heating start to take place, and $E_{\rm EH} = \dfrac{4\pi\eta_0}{c^2} J_{\rm EH}$. Especially, η is written as

$$\eta = \begin{cases} \dfrac{4\pi\eta_0}{c^2}, & J' < J_{\rm EH}, \\ \dfrac{4\pi\eta_0}{c^2}\left(\dfrac{J'}{J_{\rm EH}}\right)^{1/\gamma\ -1}, & J' > J_{\rm EH}. \end{cases} \tag{4.10}$$

In this chapter, we take γ to be 0.1 and $J_{\rm EH}$ to be arbitrary parameter. Using this model, we solve the MHD equation.

We use a shearing box and thus set a uniform shear flow, $(v_{x0}, v_{y0}, v_{z0}) = (0, -\frac{3}{2}\,\Omega x,\ 0)$. The simulation box size is $(L_x, L_y, L_z) = (H,\ 2\pi H,\ H)$, where L_x, L_y, and L_z are lengths of simulation box in each directions and H is the gas scale height. We use the periodic boundary conditions at each boundary $x = -0.5H, 0.5H; y = -\pi H, \pi H; z = -0.5H, 0.5H$ because we assume the simulated phenomena occurs in local region.

Following Hawley et al. (1995), we define the computational units of length $L_{\rm u}$, time $T_{\rm u}$, and mass $M_{\rm u}$ as H, $10^{-3}\Omega^{-1}$, and $\rho_0 H^3$, respectively, where the subscript "u" means units of our simulation results. Therefore, the unit of velocity is given by $V_{\rm u} = 10^3 c_{\rm s}$, the unit of density $\rho_{\rm u} = \rho_0$, and the unit of pressure $P_{\rm u} = 10^6 \rho_0 c_{\rm s}$. The sound speed, the initial density, and the initial pressure of numerical values ($c_{\rm s}/V_{\rm u}$, $\rho_0/\rho_{\rm u}$, and $P_0/P_{\rm u}$) are, respectively, given by $c_{\rm s}/V_{\rm u} = 10^{-3}$, $\rho_0/\rho_{\rm u} = 1$, and $P_0/P_{\rm u} = 10^{-6}$. Let the unit of magnetic field strength be

$$B_{\mathrm{u}} = \sqrt{8\pi P_0}. \tag{4.11}$$

We obtain the unit of current density from Ampére's equation,

$$J_{\mathrm{u}} = \frac{c}{4\pi}\frac{B_{\mathrm{u}}}{H}. \tag{4.12}$$

To write the Ohm's law $E = (4\pi\eta/c^2)J$ as

$$\frac{E}{E_{\mathrm{u}}} = \frac{\eta}{\eta_{\mathrm{u}}}\frac{J}{J_{\mathrm{u}}}, \tag{4.13}$$

we define the unit of electric fields strength as

$$E_{\mathrm{u}} = \frac{B_{\mathrm{u}}\eta_{\mathrm{u}}}{cH} = 10^3\frac{c_{\mathrm{s}}}{c}B_{\mathrm{u}}, \tag{4.14}$$

where we use $\eta_{\mathrm{u}} = L_{\mathrm{u}}^2/T_{\mathrm{u}} = 10^3 H c_{\mathrm{s}}$. Using these units, in this work, we define J_{max} as

$$J_{\mathrm{max}} = 10 J_{\mathrm{u}}. \tag{4.15}$$

Here, J_{max} indicates just a typical value of the resulting maximum value of current density in fully developed MRI (Muranushi et al., 2012). Note that the resulting maximum current does not necessarily equal to $10J_{\mathrm{u}}$.

We set initial setup as Figure 4.2. We give the uniform vertical magnetic fields whose strength is

$$B_{z0} = \beta_0^{-1/2} B_{\mathrm{u}}, \tag{4.16}$$

where the initial plasma beta vales β_0 is

$$\beta_0 = \frac{8\pi P_0}{B_{z0}^2}. \tag{4.17}$$

In order for MRI to grow in the beginning, we give the initial Elsasser number Λ_0 as $\Lambda_0 = 10$. Here, in this work, the Elsasser number is defined by

$$\Lambda = \frac{v_A^2}{\eta\Omega}. \tag{4.18}$$

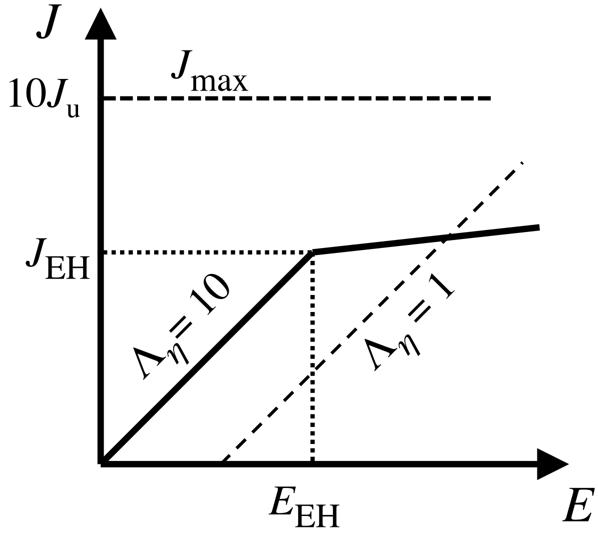

Figure 4.2: Schematic diagram of initial setup of our calculation. Initially, for MRI to grow, we give the Elsasser number $\Lambda_0 = 10$. Then, for the current growth to be suppressed, we give $J_{\rm EH}$, at which electron heating begin to occur, to be less than $J_{\rm max}$

Because an efficiency of ohmic dissipation is changed at $\Lambda = 1$, we can approximately expect MRI growth in $\Lambda > 1$ and MRI decay in $\Lambda < 1$. Thus we can also expect that final saturated current density converges on $\Lambda = 1$. In order to investigate the dependence of the results of a saturated current density, we changes the parameter $J_{\rm EH}$, which expresses where in a J–E plane, electron heating starts up. We randomly gives the initial amplitude of pressure perturbations as $\delta P/P_0 = 2.5 \times 10^{-4}$ and the one of velocity perturbations as $|\delta \boldsymbol{v}|/c_{\rm s} = 5 \times 10^{-5}$. The initial perturbation values are two orders of magnitude less than the ones of (Hawley et al., 1995). Because we treat very small fluctuations in our simulation, to properly treat them, we note that initial perturbations should be less than amplified fluctuations.

In this study, we use Athena, open source code which uses Godunov's scheme. We perform MHD simulations with a unstratified local sharing box. The fluid is compressible, isothermal, and magnetized.

In this work, we plot all values as the volume-averaged quantities as $\langle ... \rangle$ and express also the time-averaged quantities as $\langle\langle ... \rangle\rangle$. For example, the volume average of a variable a is written as

$$\langle a \rangle = \frac{\int a \, dV}{\int dV}, \tag{4.19}$$

where the integration region is the simulation box $-0.5H < x < 0.5H$, $-\pi H < y < \pi H$, and $-0.5H < z < 0.5H$. The time average of a is written as

$$\langle\langle a \rangle\rangle = \frac{\int a \ dt}{\int dt} \tag{4.20}$$

where we average a value from 20 orbits to 30 orbits in this work. Here, we express time with "orbits" which indicates one orbital time, $2\pi/\Omega$. The integration interval corresponds to final state in our simulation, and thereby the time averaged value is expected to means the saturated value.

The Courant-Friedrichs-Lewy number, which is a ratio of fluid velocity to computable velocity, is fixed at 0.4. In order for the number to be fixed, time intervals per one time step is variable since the size of a mesh is constant. We take the number of meshes to be $(N_x, N_y, N_z) = (64, 128, 64)$ in each direction. For MRI in a uniform vertical field, we have to note that at least vertical size of one cell (i.e. resolution) should be less than the most unstable wavelength to properly treat MRI growth. The most unstable mode is written as

$$\lambda_{\mathrm{m.u.,\,ideal}} = 2\pi \frac{v_{\mathrm{A},z}}{\Omega} = 2\pi \sqrt{\frac{2}{\beta_0}} H = 0.089 \left(\frac{\beta_0}{10^4} \right)^{-1/2} H. \tag{4.21}$$

Therefore, because N_z requires $N_z > 11.2 \left(\frac{\beta_0}{10^4}\right)^{1/2}$, $N_z = 64$ is reasonable resolution in our calculation.

The most interesting values in our calculation is the Maxwells stress, which greatly affects the disk evolution. Moreover, if we simply assume the magnetic energy to be the kinetic energy, the Maxwell stress also controls the velocity fluctuation which affects dynamics of solid particles. The Maxwell stress $\langle -B_x B_y \rangle / (4\pi)$ is often expressed as a Shakura-Sunyaev α parameter which is defined as the accretion stress normalized the pressure. When the Maxwell stress dominates in the accretion stress, α is written as $\alpha = \frac{\langle\langle -B_x B_y \rangle\rangle}{4\pi P}$. Although pressure P varies, in this work, we use a dimensionless value which is defined as the Maxwell stress normalized by the initial pressure,

$$\alpha_{\mathrm{M}} = \frac{\langle\langle -B_x B_y \rangle\rangle}{4\pi P_0}. \tag{4.22}$$

Table 4.1: Summary of results.

Run ID	β_0	$J_{\rm EH}$	Λ_0	$\langle\langle B^2\rangle\rangle/(8\pi P_0)$	$\langle\langle \alpha_{\rm M}\rangle\rangle$	$\langle\langle \rho v_x \delta v_y\rangle\rangle/(8\pi P_0)$	$\langle\langle J\rangle\rangle/J_{\rm u}$
34	10^4	0.001	10	$(1.0 \pm 0.0) \times 10^{-4}$	$(2.4 \pm 0.3) \times 10^{-8}$	$(2.0 \pm 0.4) \times 10^{-10}$	$(1.7 \pm 0.1) \times 10^{-3}$
35	10^4	0.003	10	$(1.0 \pm 0.0) \times 10^{-4}$	$(2.6 \pm 0.0) \times 10^{-7}$	$(1.5 \pm 0.2) \times 10^{-9}$	$(5.2 \pm 0.0) \times 10^{-3}$
36	10^4	0.01	10	$(1.1 \pm 0.0) \times 10^{-4}$	$(2.8 \pm 0.0) \times 10^{-6}$	$(1.5 \pm 0.2) \times 10^{-8}$	$(1.7 \pm 0.0) \times 10^{-2}$
37	10^4	0.03	10	$(1.6 \pm 0.0) \times 10^{-4}$	$(2.6 \pm 0.0) \times 10^{-5}$	$(1.5 \pm 0.1) \times 10^{-7}$	$(5.2 \pm 0.0) \times 10^{-2}$
38	10^4	0.1	10	$(7.6 \pm 0.0) \times 10^{-4}$	$(2.8 \pm 0.0) \times 10^{-4}$	$(1.7 \pm 0.2) \times 10^{-6}$	$(1.7 \pm 0.0) \times 10^{-1}$
39	10^4	0.3	10	$(1.8 \pm 1.2) \times 10^{-3}$	$(7.6 \pm 2.1) \times 10^{-4}$	$(9.9 \pm 9.7) \times 10^{-4}$	$(4.1 \pm 0.3) \times 10^{-1}$
40	10^4	1.0	10	$(7.0 \pm 2.4) \times 10^{-3}$	$(4.2 \pm 0.7) \times 10^{-3}$	$(2.7 \pm 2.7) \times 10^{-3}$	(1.2 ± 0.0)
41	10^4	3.0	10	$(1.3 \pm 0.1) \times 10^{-2}$	$(1.1 \pm 0.0) \times 10^{-2}$	$(2.9 \pm 1.5) \times 10^{-3}$	(2.8 ± 0.0)
42	10^4	∞	10	$(6.2 \pm 2.1) \times 10^{-2}$	$(5.6 \pm 0.7) \times 10^{-2}$	$(8.3 \pm 2.9) \times 10^{-3}$	(8.5 ± 0.9)

We have confirmed that the pressure P can vary within a factor of two at most in our calculations. In addition, we define a dimensionless value with respect to resistivity η,

$$\Lambda_\eta = \left(\frac{v_{{\rm A},z0}^2}{\eta\Omega}\right) \tag{4.23}$$

where $v_{{\rm A},z0}$ is the Alfvén velocity consisting of initial magnetic field strength, $v_{{\rm A},z0} = B_{z0}/\sqrt{4\pi\rho_0}$. Λ_η expresses the Elsasser number assuming that magnetic field strength and density do not vary. In Figure 3.4 of Section 3.2, we plot a line of $\Lambda_\eta = 1$ in a J–E plane to show the threshold of the resistive MHD. The magnetic field is not amplified during a linear growth, and thus Λ_η exactly indicates the Elsasser number Λ.

In our previous work (MO16), we have found out the scaling relation between the Maxwell stress (or $\alpha_{\rm M}$) and the current density. In the next section, in order to verify the scaling relation, we plot the Maxwell stress and the current density.

4.2 Results of Shearing-Box MHD Simulations

In this section, we present the representative simulation results. We set the initial parameters as $\beta_0 = 10^4$ and $\Lambda_0 = 10$. We give $J_{\rm EH}$ of 8 parameters as $J_{\rm EH}/J_{\rm u} = 3 \times 10^{-4}, 1 \times 10^{-2}, 3 \times 10^{-2}, 1 \times 10^{-1}, 3 \times 10^{-1}, 1, 3$, and ∞, where $J_{\rm EH}/J_{\rm u} = \infty$ means the ideal MHD case. The initial setup and result are summarized in Table 4.1.

Figure 4.3 shows the finale state ($t = 30$ orbits) of the representative our simulation results of $J_{\rm EH}/J_{\rm u} = 0.03$ and the ideal MHD case, $J_{\rm EH}/J_{\rm u} = \infty$, for comparison. We also show the x–z and y–z plane at the final state of the each parameters in Figure 4.4.

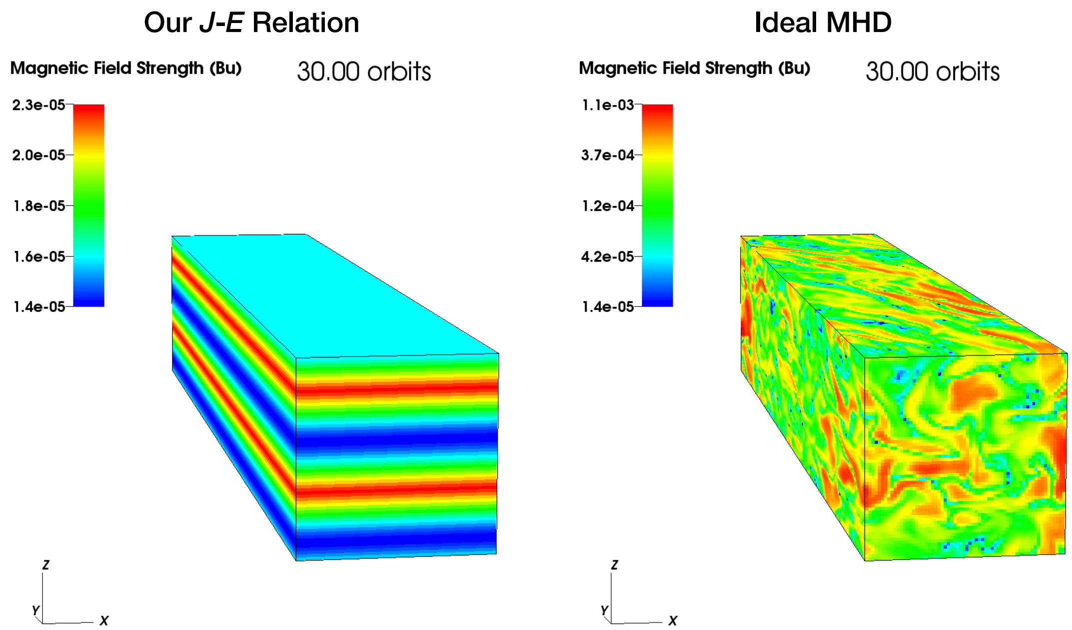

Figure 4.3: Outline of representative our MHD shearing box simulations. The left figure shows the distribution of magnetic field strength $|\boldsymbol{B}|$ with our J–E relation of $J_{\rm EH}/J_{\rm u} = 0.03$. The right figure shows the result in ideal MHD case for comparison. These figures show the final state of the calculations. Note that the color range of the two is largely deferent.

We find the ordered magnetic field and the non-turbulent steady state, the laminar flow or the stationary state, with our J–E relation model, whereas the magnetic turbulence is generated in the ideal MHD case because of the MRI nonlinear growth. In the non-turbulent state, the magnetic field is stretched in the y-direction, and thereby sinusoidal structure of the magnetic field forms in y–z plane (the upper left panel in the upper block in Figure 4.4). Because azimuthal magnetic field B_y varies in the z-direction, the layered contour of magnetic field strength appears. Such an anti-parallel magnetic field structure forms a current sheet which is maximum in calculating box. In our model, the growth of the current sheet is suppressed by the increasing resistivity. Thus, the initial uniform magnetic field is stretched but its growth stops at the sinusoidal structure.

In Figure 4.5, we shows the tracks of the volume-averaged current density $\langle J \rangle$ and electric field strength $\langle E \rangle$ in order to check our model. The current densities initially grow on the line of $\Lambda_0 = 10$ and then branch off the line after the current densities reaches each $J_{\rm EH}$. We confirm that our model works according to our expectation of J–E relation. We also confirm that the Elsasser number of initial magnetic field strength

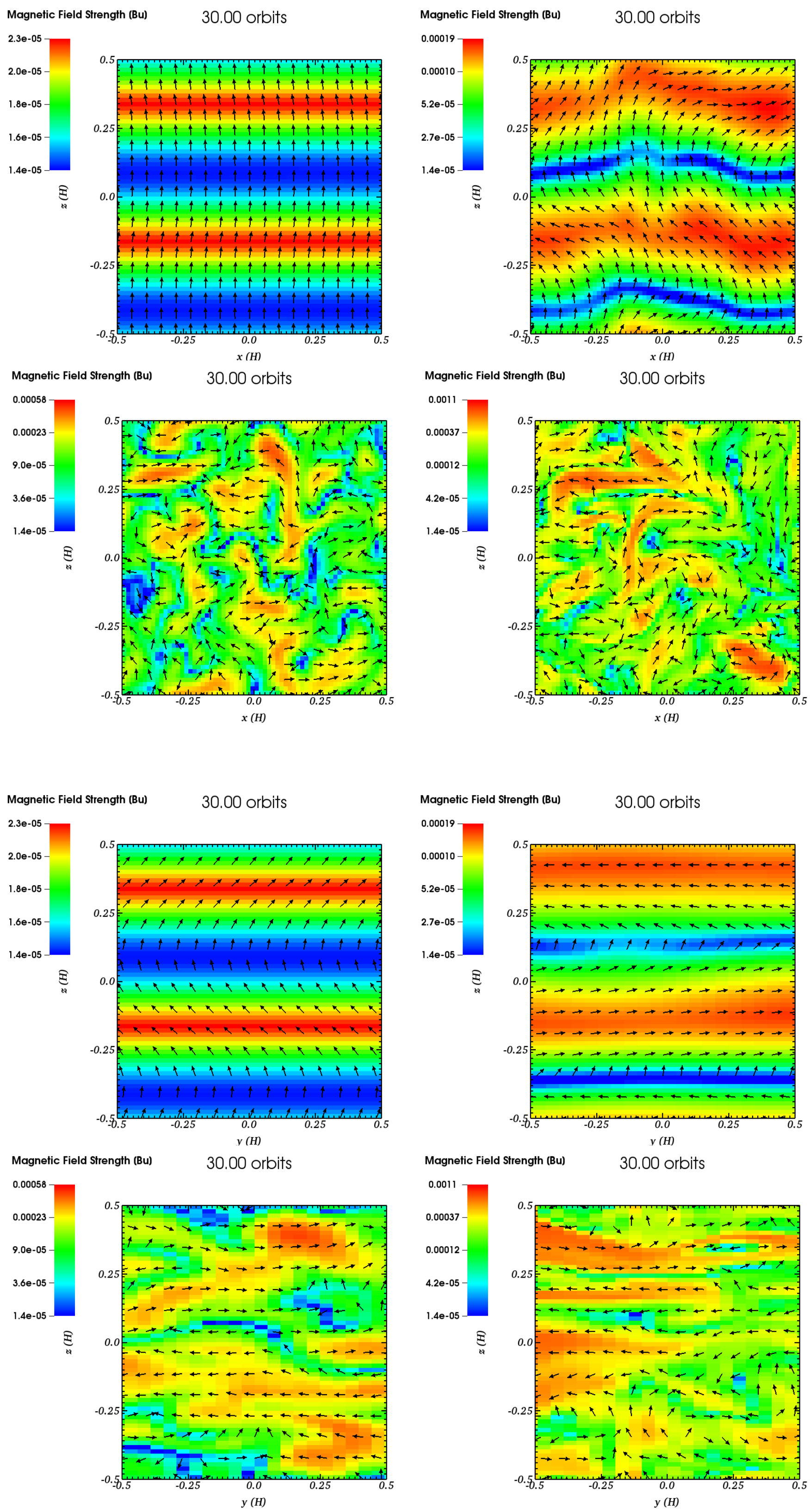

Figure 4.4: Magnetic field distribution in the x–z plane ($-0.5H \leq x \leq 0.5H, -0.5H \leq z \leq 0.5H$; upper block including four panels) and y–z plane ($-0.5H \leq y \leq 0.5H, -0.5H \leq z \leq 0.5H$; lower block including four panels) at the final state ($t = 30$ orbits) of the each calculation. The each panel in blocks shows the case of $J_{\mathrm{EH}}/J_{\mathrm{u}} = 0.03$ (upper left), 0.3 (upper right), 3 (lower left), and the ideal MHD (lower right). The arrows show directions of the magnetic field in x-z plane, but does not express the magnitude. The colors show the magnetic field strength $|\boldsymbol{B}|$, but note that the color scale varies at each initial parameters.

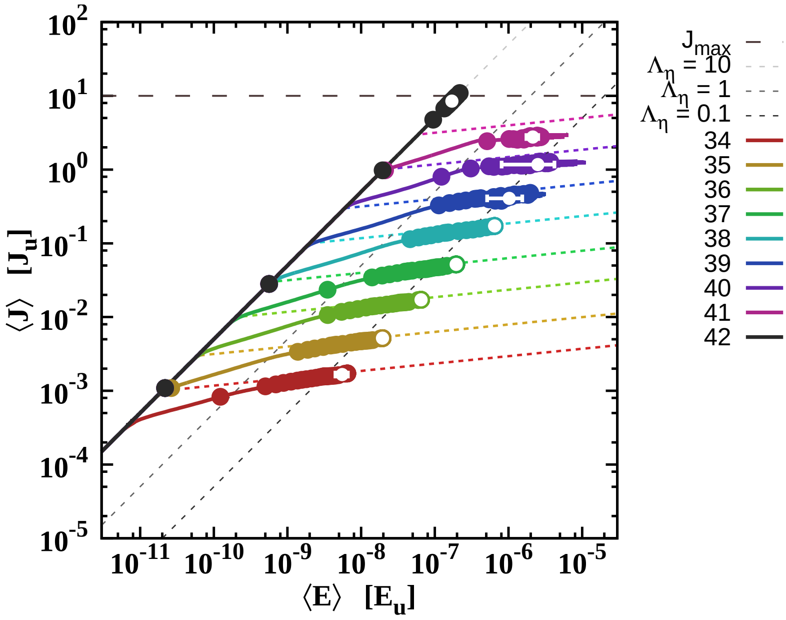

Figure 4.5: Tracks in the current-field plane. The vertical axis shows volume-averaged current density $\langle J \rangle$, and the horizontal axis volume-averaged electric field strength $\langle E \rangle$. The colors show run ID which means variation of $J_{\rm EH}$. The dashed lines of white grey, grey, and dark grey show the initial Elsasser number $\Lambda_\eta = 10, 1,$ and 0.1. The circles are plotted at equal intervals ($\Delta t = 1$ orbits) to express the speed in the J–E plane. The white filled circles show that saturated vale of $\langle J \rangle$ and $\langle E \rangle$ of each $J_{\rm EH}$.

Λ_η is approximately saturated at $\Lambda_\eta = 0.1$.

In Figure 4.6, we shows the time variation of the Maxwell stress varying the parameter $J_{\rm EH}$ which control saturated current density. We found that the saturated Maxwell stress depends on $J_{\rm EH}$. Thus saturated Maxwell stress depends on the saturated current density. Lower current density provides lower Maxwell stress. Therefore, we can conclude that MRI growth stops if electron heating begin to take place at much low electric field strength. We also find the saturated MRI behavior can be divided into the two case, the fluctuated case ($J_{\rm EH} \lesssim 0.1$) and the stationary case ($J_{\rm EH} \gtrsim 0.3$). According to Figure 4.3, the two case would correspond to the turbulent state and laminar state. Thus, we can find the threshold of current density at which the MRI completely dies away. Hereafter, we call the threshold by $J_{\rm turb}/J_{\rm u} \approx 0.3$.

In MO16, we used a scaling relation between the Maxwell stress and current density to investigate the possibility of suppressing MRI by electron heating. The scaling relation

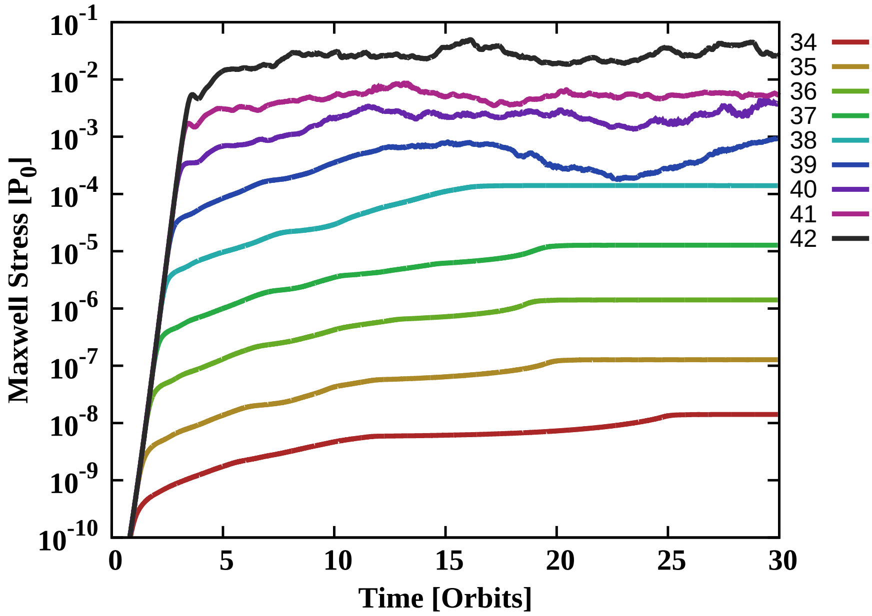

Figure 4.6: Time variation of α_{M} with variating J_{EH}. The colors show the different value of J_{EH}, and the black solid line shows the ideal MHD case.

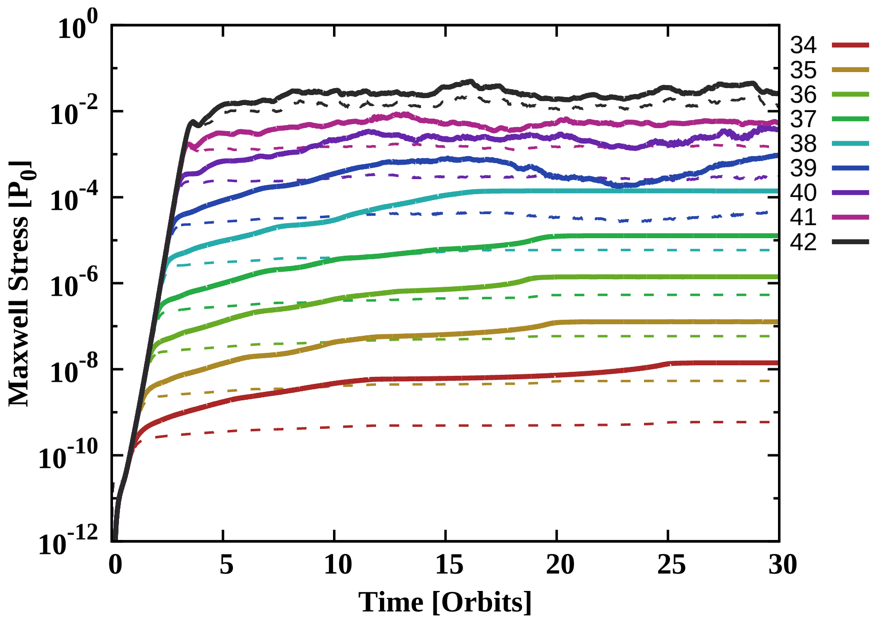

Figure 4.7: Figure 4.6 with plot of the analytical scaling relation presented in MO16. The dashed lines show the scaling relation.

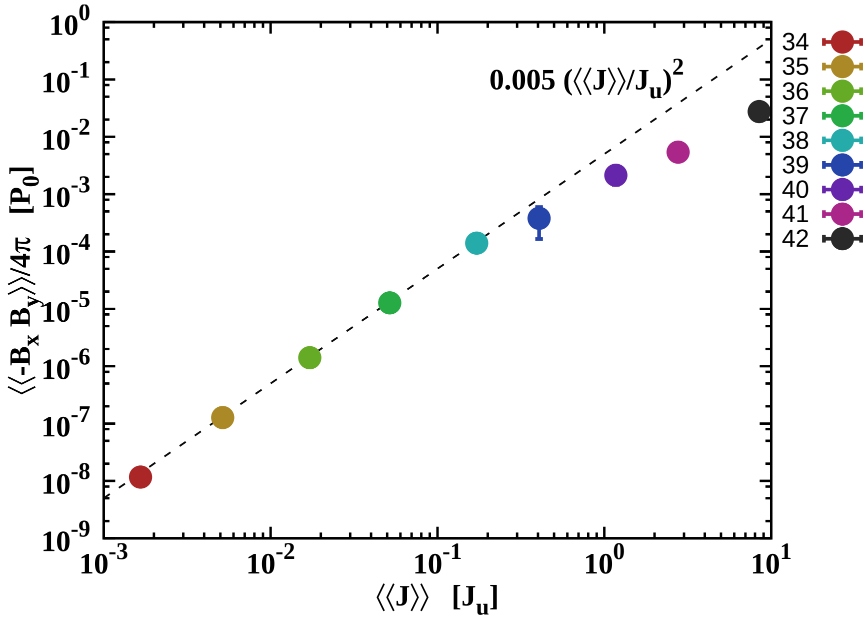

Figure 4.8: Dependence of volume-averaged $\langle \alpha_\mathrm{M} \rangle$ to volume-averaged $\langle J \rangle$ (colored dots). The colors show the same as Figure 4.3. The dashed line shows the fitting formulae in low current region, $\langle \alpha_\mathrm{M} \rangle = 0.005(\langle J \rangle / J_\mathrm{u})^2$ or $0.5(\langle J \rangle / J_\mathrm{max})^2$.

is written as

$$\alpha_\mathrm{M} \approx 0.02 \left(\frac{\beta_0}{10^4}\right)^{-1} \left(\frac{J}{J_\mathrm{max}}\right)^2 . \tag{4.24}$$

However, the equation is supported only by the scaling law. In addition, even the existence of this relation is not clear because many previous studies have not focused the relation of current density to the Maxwell stress. Thus, in order to verify this relation, we plot the formula over the resulting Maxwell stress in Figure 4.7. The relation is expressed as a function only of the initial plasma beta β_0 and current density J. Thus, if the relation is correct, the relation should be similar to the result at each time. However, Figure 4.7 shows that the relation does not follow the resulting Maxwell stress, although the relation follows the plot during the MRI linear growth. At the final state, the saturated Maxwell stress of the two is different by a factor of 3–10. In Section 4.3, we will investigate the cause of this discrepancy and will propose a new predictive formula for α as a function of J. We improve the relation between the Maxwell stress and current density (Equation (4.24)) using a more sophisticated scaling law (Equation (4.34) in Section 4.3).

To obtain an empirical formula of the stress–current relation in saturated state, taking

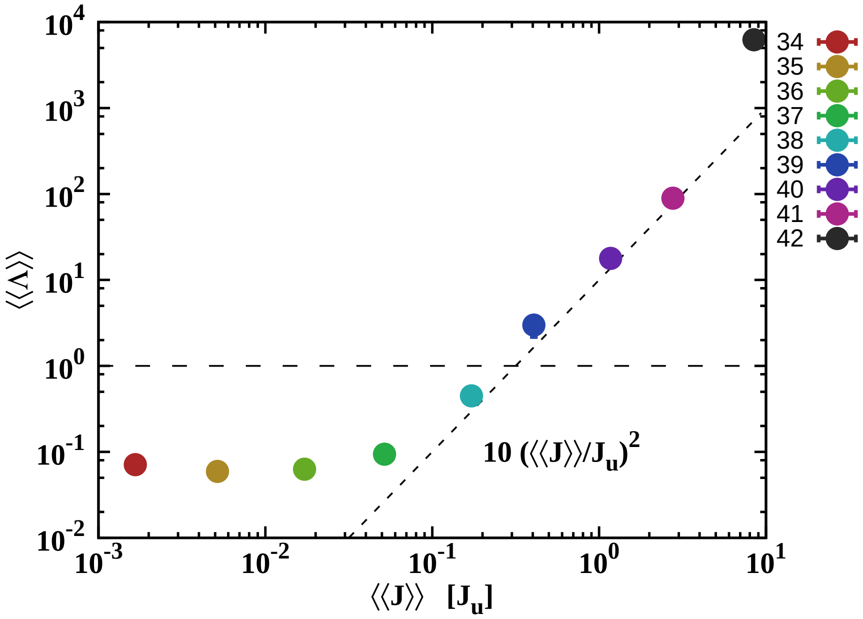

Figure 4.9: Dependence of time- and volume-averaged Elsasser number $\langle\langle\Lambda\rangle\rangle$ on time- and volume-averaged $\langle\langle J\rangle\rangle$.

the time average of the Maxwell stress and current density, we show dependence of the saturated Maxwell stress $\langle\langle\alpha_{\rm M}\rangle\rangle$ on saturated current density $\langle\langle J\rangle\rangle$ in Figure 4.8. In this chapter, since the interval of the time integration is from 20 orbits to 30 orbits, the time average means saturated values. We confirm an obvious correlation between the two quantities. Fitting the correlation with a quadratic function, we obtain the empirical formula of the relation, $0.005(\langle\langle J\rangle\rangle/J_{\rm u})^2$ or $0.5(\langle\langle J\rangle\rangle/J_{\rm max})^2$. We can see that the Maxwell stress largely depends on current density. This formula means that a lower current leads to lower turbulence strength.. The dependence on current density, $\alpha_{\rm M} \propto J^2$, is consistent with Equation (4.24) presented in MO16. Thus, in Equation 4.24, the dependence of current density is consistent with the results, whereas the magnitude is different from the results. Note that since in this calculation the initial plasma beta β_0 is constant, the dependence on β_0 does not appear in this fitting formula.

Here we address what determines the boundary of the laminar and turbulent state, namely what determines $J_{\rm turb}$. In Figure 4.8, we can see that the fitting formula is slightly incorrect at high current density ($\langle J\rangle \gtrsim J_{\rm turb}$),. This may concern the nonlinear evolution of the Elsasser number. Figure 4.9 shows dependence of the volume- and time-averaged Elsasser number $\langle\langle\Lambda\rangle\rangle$ on current density. Here, the Elsasser number is defined as $\Lambda = v_{\rm A}^2/(\eta\Omega) = |\boldsymbol{B}|^2/(4\pi\rho_0\eta\Omega)$. As we see, at $J > J_{\rm turb}$, we can see that

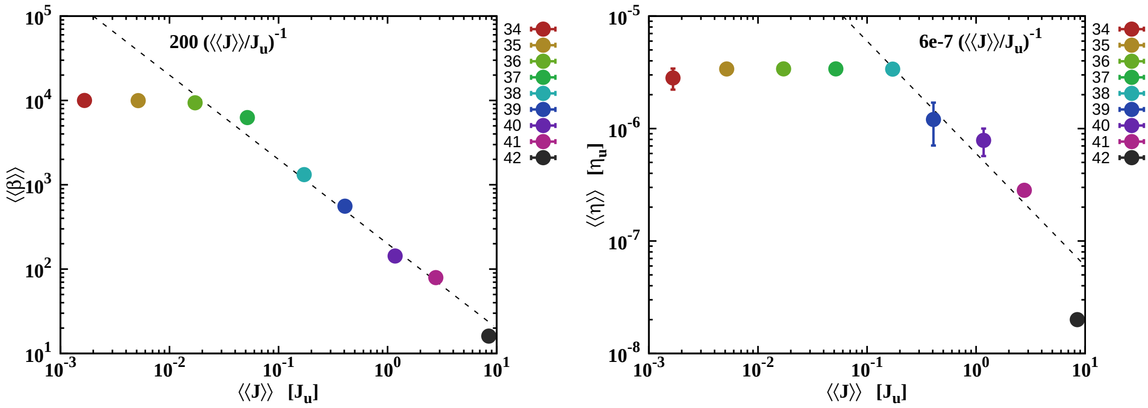

Figure 4.10: Dependence of time- and volume-averaged plasma beta $\langle\langle\beta\rangle\rangle$ and resistivity $\langle\langle\eta\rangle\rangle$ on time- and volume-averaged $\langle\langle J\rangle\rangle$. The colors shows the same as Figure 4.9.

the threshold current density $J_{\rm turb}$ approximately corresponds to the current density at $\Lambda = 1$. Thus, we can naturally understand that the MRI does not generate the magnetic turbulence because MHD is resistive at $\Lambda \lesssim 1$. On the other hands, the MRI generates the turbulence at $\Lambda \gtrsim 1$.

The increase of the Elsasser number is understood by the following. The Elsasser number can be written as

$$\Lambda = \frac{v_A^2}{\eta\Omega} = \frac{B^2}{4\pi P}\frac{\rho c_{\rm s}^2}{\eta\Omega} = 2\times 10^{-3}\frac{1}{\beta}\frac{\eta_{\rm u}}{\eta}.$$

Thus, Λ is proportional to $\beta^{-1}\eta^{-1}$. Figures 4.10 shows dependence of the volume- and time-averaged plasma beta $\langle\langle\beta\rangle\rangle$ (left panel) and resistivity $\langle\langle\eta\rangle\rangle$ on $\langle\langle J\rangle\rangle$(right panel). We can see that when $\langle\langle\Lambda\rangle\rangle$ begins to increase, $\langle\langle\Lambda\rangle\rangle$ also begins to increase. $\langle\langle\eta\rangle\rangle$ begins to decrease when $\langle\langle\Lambda\rangle\rangle$ reaches unity. Thus, we can expect that $\langle\langle\Lambda\rangle\rangle$ is increased by $\langle\langle\beta\rangle\rangle$ in $0.03J_{\rm u} < J < J_{\rm turb}$. $\langle\langle\eta\rangle\rangle$ decreases due to changing state of flow and thereby $\langle\langle\Lambda\rangle\rangle$ increases with $\langle\langle J^2\rangle\rangle$.

To see why the MRI is saturated in steady non-turbulent state when the resistivity by the electron heating, in Figure 4.11, we shows the time variation of the critical wavelength. The critical wavelength is the shortest wavelength in unstable MRI mode and defined as

$$\lambda_{{\rm crit},z} \approx 2\pi\frac{1}{\sqrt{3}}\frac{v_{{\rm A},z}}{\Omega}\left(1+\Lambda_z^{-1}\right), \tag{4.25}$$

which is given by the dispersion relation in a steady state (Sano & Miyama, 1999). The

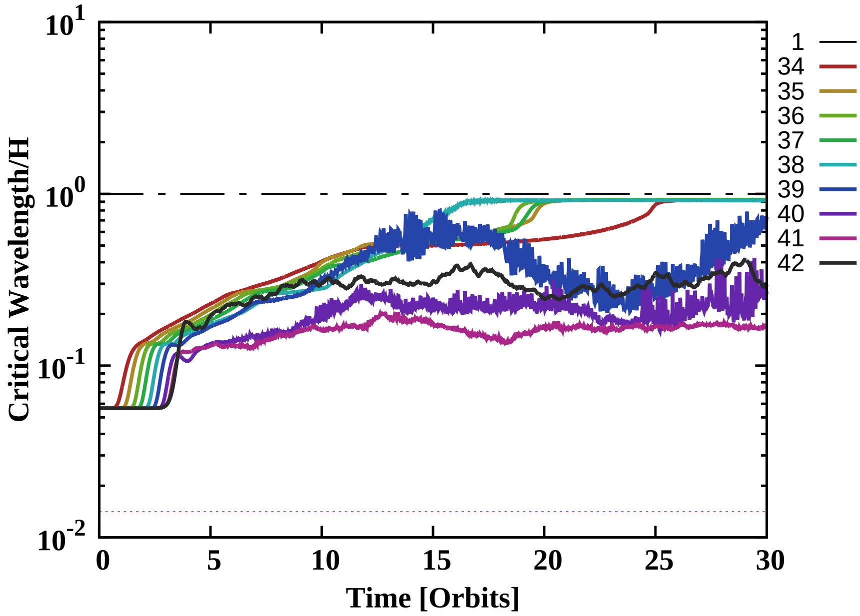

Figure 4.11: Critical wavelength $\lambda_{\mathrm{crit},z}$ (lower panel) in vertical direction and normalized by H. The colors show the same as Figure 4.3.

critical wavelength is approximately equal to simulation box size H. This indicates that unstable wavelength become larger and larger during MRI growth, and then all MRI unstable mode dies when the unstable wavelength cannot exist. Thus, in this simulation, the final state is determined by the box size.

4.3 Predictive Formulae

In this section, we derive a formula which predicts the Maxwell stress from current density. Simulation of MRI can treat significantly shorter time than the disk lifetime. Thus, such the predictive formula enable us to introduce the effect of turbulence as α parameter. In Subsection 4.3.1, we derive a fitting formula which predicts the Maxwell stress in both the laminar and turbulent state. Then, in Subsection 4.3.2, focusing that the fluctuation can be assumed to be first order, we derive an analytical expression of the laminar state that exactly gives the physical quantities. The expression also provides an interpretation of the scaling relation in the laminar state.

4.3.1 Scaling Relation

Here we improve the scaling relation presented in MO16 and find the practical predictive formula. First, we determine an fitting formula of the laminar state from a scaling law, and then we determine that in the ideal MHD case. After that, we link the two formulae together by taking the average to reproduce simulation results.

We first derive a scaling relation between the Maxwell stress and the current density, noting that MHD is resistive when MRI is saturated by the increased resistivity. To relate current density to Maxwell stress, we take ∇ to be the typical wavenumber $\boldsymbol{k}$ in the Ampére's equation $\boldsymbol{J} = \frac{c}{4\pi}\nabla\times\boldsymbol{B}$. Here, we assume that $\boldsymbol{k}$ is the critical wavenumber in the vertical direction,

$$k = k_{z,\mathrm{crit}} = \sqrt{3}\frac{v_{\mathrm{A}z0}}{\eta} \tag{4.26}$$

The current densities of x and y components are described as

$$J_x \approx -\frac{c}{4\pi}k_{z,\mathrm{crit}}B_y, \tag{4.27}$$
$$J_y \approx \frac{c}{4\pi}k_{z,\mathrm{crit}}B_x. \tag{4.28}$$

Therefore, using the current density, Maxwell stress $\langle B_x B_y\rangle/(4\pi)$ normalized P_0 can be expressed as

$$\begin{aligned}
\alpha_{\mathrm{M}} &= \frac{1}{4\pi P_0}\left(\frac{J_x J_y}{k_{z,\mathrm{crit}}^2}\right)\left(\frac{4\pi}{c}\right)^2 \\
&= 200\frac{1}{3}\left(\frac{\eta}{v_{\mathrm{A}z0}H}\right)^2\left(\frac{J_x J_y}{J_{\max}^2}\right), \\
&= 200\frac{1}{3}\left(\frac{v_{\mathrm{A}z0}^2}{c_{\mathrm{s}}^2}\right)\left(\frac{\eta\Omega}{v_{\mathrm{A}z0}^2}\right)^2\left(\frac{J_x J_y}{J_{\max}^2}\right), \\
&= 400\frac{1}{3}\left(\frac{1}{\beta_{z0}}\right)\Lambda_\eta^{-2}\left(\frac{J_x J_y}{J_{\max}^2}\right),
\end{aligned} \tag{4.29}$$

where the current densities is normalized by the maximum current density in fully developed MRI, $J_{\max} = 10\sqrt{\frac{\rho}{2\pi}}c\Omega$,(Muranushi et al., 2012). J would be dominated by J_x because B_y is generally larger than B_x (e.g., Hawley et al., 1995; Sano et al., 2004), and therefore we assume that $J_x \approx J$ and $J_y \approx J(B_x/B_y)$.

$$\alpha_{\mathrm{M}} = 400\frac{1}{3}\left(\frac{1}{\beta_{z0}}\right)\Lambda_\eta^{-2}\frac{B_x}{B_y}\frac{J^2}{J_{\mathrm{max}}^2}, \tag{4.30}$$

As we see below, we here assume the ratio of B_x to B_y in the saturated laminar state (Equation (4.41)),

$$\frac{B_x}{B_y} = -2\Lambda_{\eta,\mathrm{sat}} = -0.1\left(\frac{\beta_{z0}}{10^4}\right)^{-1/2}. \tag{4.31}$$

Then, we obtain

$$\alpha_{\mathrm{M,lami}} = 1.3\times 10^{-3}\left(\frac{\beta_{z0}}{10^4}\right)^{-1.5}\Lambda_\eta^{-2}\left(\frac{J}{J_{\mathrm{max}}}\right)^2. \tag{4.32}$$

This expression provides the Maxwell stress once current density and Λ_η is given.

On the other hand, in the case of the ideal MHD, the scaling relation has been obtained in MO16 (or see Equation (4.24))

$$\alpha_{\mathrm{M,turb}} \approx 3\times 10^{-2}\left(\frac{\beta_{z0}}{10^4}\right)^{-1}\left(\frac{J}{J_{\mathrm{max}}}\right)^2, \tag{4.33}$$

where we have modified a factor of 1.5 to fit with our results.

Finally, we take link the two formulae together by taking the average. For best fitting, we square a sum of root values,

$$\begin{aligned}\alpha_{\mathrm{M}} &= \left((\alpha_{\mathrm{M,\,turb}})^{1/2} + (\alpha_{\mathrm{M,\,lami}})^{1/2}\right)^2 \\ &= \left(\left(3\times 10^{-2}\left(\frac{\beta_{z0}}{10^4}\right)^{-1}\right)^{1/2} + \left(1.3\times 10^{-3}\left(\frac{\beta_{z0}}{10^4}\right)^{-1.5}\Lambda_\eta^{-2}\right)^{1/2}\right)^2\left(\frac{J}{J_{\mathrm{max}}}\right)^2\end{aligned} \tag{4.34}$$

In Figure 4.12, we plot (4.34) over Figure 4.6. We can see that the equation surprisingly reproduce the resulting Maxwell stress at each time. The formula requires the initial plasma beta β_0, current density J, and Λ_η. β_0 is usually given by initial magnetic field. Λ_η is analytically given by (4.38) in the laminar state. Even in the turbulent state, Λ_η can be estimated to be approximately 0.1. In the J–E plane, Λ_η corresponds to the contour whose slope is proportional to J. Thus, once Λ_η is given, J also is determined.

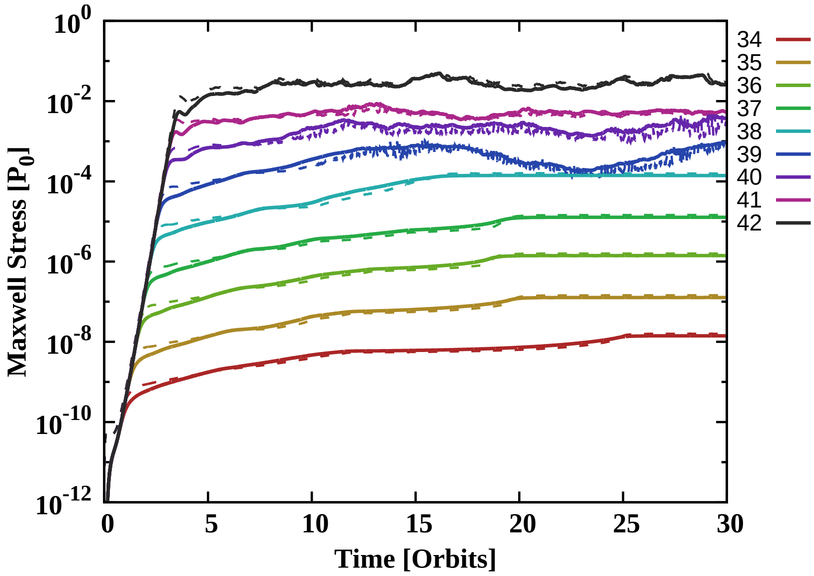

Figure 4.12: Figure 4.6 with plot of Equation (4.34). The dashed lines show the equation.

Using this formula, we can predict the Maxwell stress from the J–E relation at a location in protoplanetary disks.

We have to note that these results is based just on the simple analytic J–E relation. In reality, the electron heating rises the N-shaped nonlinear Ohm's law. Of course, finally, the real effect of electron heating on MRI is investigated by considering the realistic resistivity model with a MHD simulation. However, this work first unveils the relation of Maxwell stress and current density and the state when MRI completely dies away by suppressing current density. The importance of current density in MRI is stressed. We eventually conclude that the reliability of the suppression of MRI by electron heating has been shown by this work.

4.3.2 Analytical Solution of Laminar State

Next, we present a solution of the laminar state that provides a better understanding of the empirical formula of Equation (4.32). As we see below, the laminar state can be obtained by an analytical manner. A point of the manner is to assume that linearized equations are available because the fluctuations of the final state is sufficiently small to be first order displacement even in the "nonlinear" stage. Actually, the nonlinearity of the simulation is imposed on the evolution of resistivity. In addition, some features of the laminar state is also available. At the laminar state, one wavelength of the magnetic field vertically lies in simulation box, as we see in Figure 4.3. Thus, we can use the vertical wavelength $k_z = 2\pi/H$. Since the laminar state is steady, we can evidently neglect time-evolution terms in basic equations. In the concrete, we put $\omega = 0$. Since ω and k are given in the dispersion relation $\omega = \omega(k, \eta)$, we obtain the saturated resistivity in the steady laminar state, $\eta_{\rm sat}$. $\eta_{\rm sat}$ also gives the saturated Elsasser number Λ. Moreover, since η is a function of current density J in our model (see Equation (4.10)), we can obtain also the saturated current density, $J_{\rm sat}$. Thus, finally, we will obtain an analytical solution of the Maxwell stress in the saturated laminar state because the current is closely related to magnetic field.

First, let us derive resistivity in the saturated state, $\eta_{\rm sat}$. We use the dispersion relation derived from the linearized equations in Sano & Miyama (1999),

$$v_{{\rm A}z0}^4 k_z^4 + \Omega^2 \eta_{\rm sat}^2 k_z^2 - 3\Omega^2 v_{{\rm A}z0}^2 k_z^2 = 0, \tag{4.35}$$

where we have assumed incompressible fluid, a sheet approximation, and a uniform vertical magnetic field. The uniform magnetic field is justified by the fact that fluctuation of B_z is much smaller than B_{z0}. Solving Equation (4.35) with respect to $\eta_{\rm sat}$, we obtain η as function of k_z,

$$\eta_{\rm sat} = \sqrt{\frac{3v_{{\rm A}z0}^2}{k_z} - \frac{v_{{\rm A}z0}^4}{\Omega^2}}. \tag{4.36}$$

Using $k_z = 2\pi/H$ in Equation (4.36), η is analytically given by

$$\eta = \frac{v_{{\rm A}z0}^2}{\Omega}\sqrt{\frac{\beta_{z0}}{\beta_{\rm crit}} - 1} \approx \frac{v_{{\rm A}z0}^2}{\Omega}\sqrt{\frac{\beta_{z0}}{\beta_{\rm crit}}}, \tag{4.37}$$

where $\beta_{\rm crit}$ is defied as $\beta_{\rm crit} = 8\pi^2/3$ and we have used $\beta_{z0} > \beta_{\rm crit} \approx 26.3$. Thus, dividing Equation (4.37) by $v_{{\rm A}z0}^2/\Omega$, we obtain the Elsasser number in the saturated state as

$$\Lambda_{\eta,\,{\rm sat}} = \frac{v_{{\rm A}z0}^2}{\eta\Omega} = \sqrt{\frac{\beta_{\rm crit}}{\beta_{z0}}} = 0.051\left(\frac{\beta_{z0}}{10^4}\right)^{-1/2}. \tag{4.38}$$

We show dependence of the time- and volume-averaged $\Lambda_{\eta,\,{\rm sat}}$ on $\langle\langle J\rangle\rangle$ in Figure 4.13 in order to verify this formula. We confirm that at $J \lesssim J_{\rm turb}$, the formula is consis-

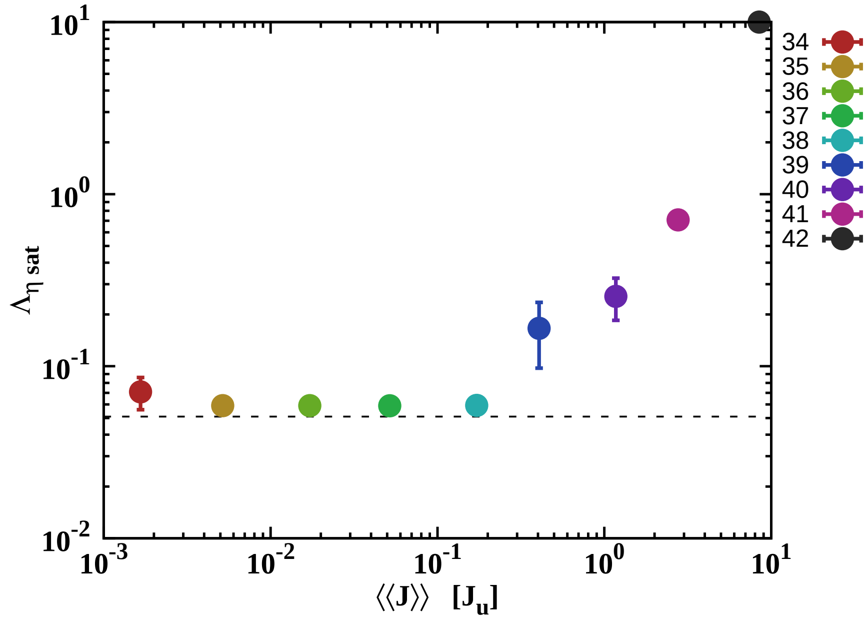

Figure 4.13: Dependence of $\Lambda_{\eta,\mathrm{sat}}$ on $\langle\langle J\rangle\rangle$. The dashed line shows Equation (4.38).

tent with the result. When the formula well reproduces the result, the fluctuation is small because this formula is derived only by assumption of the linearization of basic equations. Because the nonlinearity of the fluctuations does not appear, we can expect this formula to strongly predict $\Lambda_{\eta,\mathrm{sat}}$ and other physical quantities. Note that in usual the dispersion relation with $\omega = 0$ leads to the shortest unstable wavenumber (critical wavenumber), $k_{\mathrm{crit}} = \sqrt{3}v_{\mathrm{A}z0}/\eta$. Thus, the assumption of $k_{\mathrm{crit}} = 2\pi/H$ means that MRI growth stops at the laminar state because unstable wavenumbers can not exist in the simulation box. We can also derive Equation (4.37) from a equation $2\pi H = k_{\mathrm{crit}}$.

Next, we give the Maxwell stress as a function of current density J. We obtain a relationship between B_x and B_y from Sano & Miyama (1999),

$$B_x = \frac{v_{\mathrm{A}z0}^2}{\eta_{\mathrm{sat}}\Omega}(-2\delta B_y) = -2\Lambda_{\eta,\mathrm{sat}} B_y, \tag{4.39}$$

$$B_y = \frac{v_{\mathrm{A}z0}^2}{\eta_{\mathrm{sat}}\Omega}\left(\frac{1}{4} - \frac{1}{4}\frac{\Omega^2}{v_{\mathrm{A}z0}^2 k_z^2}\right) B_x = \Lambda_{\eta,\mathrm{sat}}\left(\frac{1}{4} - \frac{1}{4}\frac{\Omega^2}{v_{\mathrm{A}z0}^2 k_z^2}\right) B_x. \tag{4.40}$$

These relations give the ratio between B_x and B_y as, dividing Equation (4.39) by B_y,

$$\frac{B_x}{B_y} = -2\Lambda_{\eta,\mathrm{sat}} = -0.1\left(\frac{\beta_{z0}}{10^4}\right)^{-1/2}. \tag{4.41}$$

Here, we define the Maxwell stress normalized by P_0 in the laminar state as $\alpha_{\mathrm{M,\,lami}}$. From Equation (4.39), α_{M} is given by

$$\alpha_{\mathrm{M,\,lami}} = \Lambda_{\eta,\mathrm{sat}} \frac{1}{4\pi P_0} 2B_y^2. \tag{4.42}$$

Ampére's equation $\boldsymbol{J} = c/(4\pi)\ (\nabla \times \boldsymbol{B})$ can current density to magnetic field. Substituting k_z for ∇, we obtain the relation between J_x and B_y,

$$J_x \approx -\frac{c}{4\pi} k_z B_y. \tag{4.43}$$

Because a current sheet is formed by anti-parallel B_y, J_x dominates J. Thus, we can reasonably assume that

$$J \approx J_x. \tag{4.44}$$

Thus, using Equations (4.38), (4.42), (4.43), and (4.44), we obtain $\alpha_{\mathrm{M,\,lami}}$ as a function of J_{sat},

$$\begin{aligned} \alpha_{\mathrm{M,\,lami}} &= \frac{4}{k^2 H^2} \Lambda_{\eta,\mathrm{sat}} \left(\frac{J_{\mathrm{sat}}}{J_{\mathrm{u}}}\right)^2 \\ &\approx 0.52 \left(\frac{\beta_{z0}}{10^4}\right)^{-1/2} \left(\frac{J_{\mathrm{sat}}}{J_{\mathrm{max}}}\right)^2, \end{aligned} \tag{4.45}$$

where we have used $k_z = 2\pi/H$ and normalized J_{sat} by the maximum current density $J_{\mathrm{max}} = 10 J_{\mathrm{u}}$ which is expected to be the saturated current in fully developed MRI turbulence. This formula can be shown from the scaling relation of Equation (4.32), substituting Λ_η^{-2} of Equation (4.38) into Equation (4.32).

Then, we present maxwell stress in our model mimicking the real nonlinear Ohm's law. The J–E relation of our model at $J > J_{\mathrm{EH}}$ is given by the power function with the index γ (Equation (4.8)), $J \propto E^\gamma$. Since we have already obtained the saturated η_{sat} in Equation (4.37), the specified J–E relation can gives the saturated current density. Once saturated current density J_{sat} is obtained, Equation (4.49) gives the Maxwell stress α_{M} which is the most interesting value. Thus, we here derive a specific formula of α_{M} when the J–E relation is given by the power function at saturated state. In the power function of the J–E relation, $\eta_{\rm sat}$ is given by, (Equation (4.10)),

$$\eta_{\rm sat}(J) = \eta_0 \left(\frac{J_{\rm sat}}{J_{\rm EH}}\right)^{\frac{1}{\gamma}-1}. \tag{4.46}$$

Multiplying this equation by $\Omega/v_{{\rm A}z0}^2$, the inverse is given by

$$\Lambda_{\eta,{\rm sat}} = \Lambda_0 \left(\frac{J_{\rm sat}}{J_{\rm EH}}\right)^{1-\frac{1}{\gamma}} \tag{4.47}$$

Using Equation (4.44), we obtain

$$J_x = J_{\rm EH} \left(\frac{\Lambda_{\eta,\,{\rm sat}}}{\Lambda_0}\right)^{\frac{\gamma}{\gamma-1}}. \tag{4.48}$$

Substituting this equation for $J_{\rm sat}$ in Equation (4.49), we obtain

$$\begin{aligned}
\alpha_{\rm M,\,lami} &\approx 0.52 \left(\frac{\beta_{z0}}{10^4}\right)^{-1/2} \left(\frac{J_{\rm EH}}{J_{\rm max}}\right)^2 \left(\frac{\Lambda_0}{\Lambda_{\eta,\,{\rm sat}}}\right)^{\frac{2\gamma}{1-\gamma}} && (4.49)\\
&\approx 0.52 \left(\frac{\beta_{z0}}{10^4}\right)^{-1/2} \left(\frac{J_{\rm EH}}{J_{\rm max}}\right)^2 \left(195 \left(\frac{\Lambda_0}{10}\right) \left(\frac{\beta_{z0}}{10^4}\right)^{1/2}\right)^{\frac{2\gamma}{1-\gamma}} && (4.50)
\end{aligned}$$

We have used $\gamma = 0.1$. Here, using $\gamma = 0.1$, the Maxwell stress in our model is written as

$$\alpha_{\rm M,\,lami} \approx 1.68 \left(\frac{\beta_{z0}}{10^4}\right)^{-1/2} \left(\frac{J_{\rm EH}}{J_{\rm max}}\right)^2 \left(\frac{\beta_{z0}}{10^4}\right)^{-7/18} \left(\frac{\Lambda_{z,\,0}}{10}\right)^{2/9}. \tag{4.51}$$

This predictive formula of the Maxwell stress in the laminar state is available when J–E relation during electron heating is given by a power function with the index $\gamma = 0.1$.

In usual, a nonlinear state of MRI can not be expressed by such the analytic expression because of the nonlinearity of the fluctuations. Thus, when electron heating effectively completely dies away MRI, the accretion stress will be exactly given by these quantities.

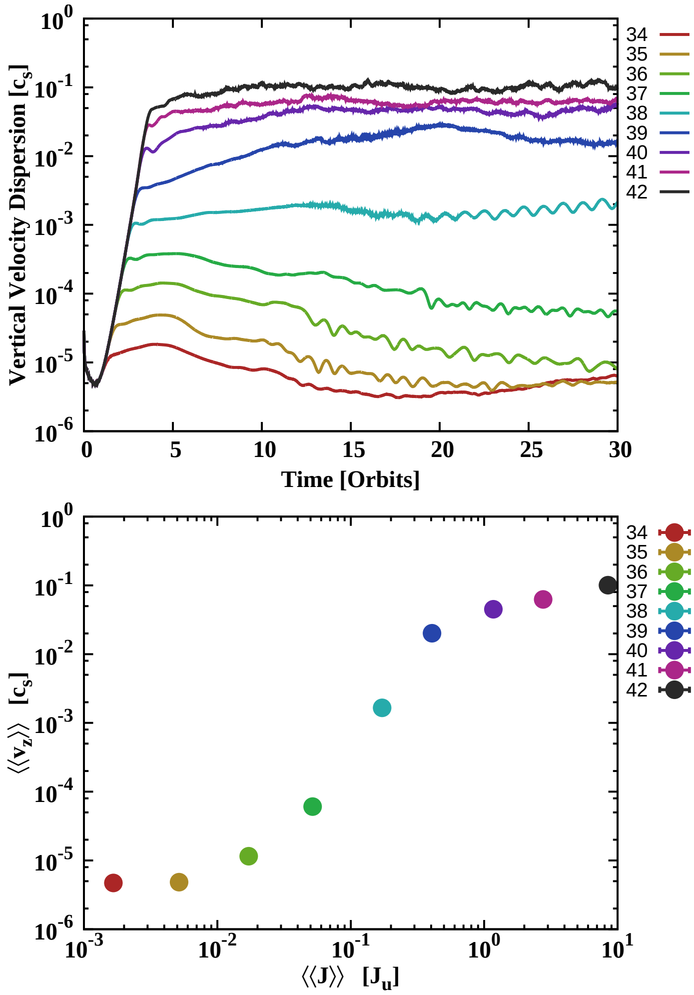

Figure 4.14: Time variation of volume-averaged vertical velocity $\langle v_z \rangle$normalized by sound speed c_s (upper panel) and dependence of time- and volume-averaged resistivity $\langle\langle v_z \rangle\rangle$ on time- and volume-averaged $\langle\langle J \rangle\rangle$ (lower panel). The colors are the same as in Figure 4.5.

4.4 Discussion

4.4.1 Vertical Diffusion of Dust

Here we describe the implication for dust dynamics in the disks. Under the classical planetesimal formation theories, the sedimentation of dust forms a dusty layer on midplane which is gravitationally unstable. Then, the dust layer causes gravitational instability and forms planetesimals. This model has been focused in terms of avoiding meter size barrier. However, disk turbulence easily stir up the dust layer and diffuse it . Therefore, weak disk turbulence may help the planetesimal formation.

To investigate the potential of the laminar state to help dust settling, we investigate vertical velocity at each parameter. The upper panel of Figure 4.14 shows the time variation of vertical velocity, and the lower panel of Figure 4.14 shows dependence of the time-averaged one on $\langle J \rangle$. We can see that vertical velocity drops at $\langle J \rangle / J_{\rm u} \sim 10^{-1}$ where the state of gas motion changes from turbulence to laminar flow. To settle down, dust grains requires

$$\mathrm{St} > \frac{\delta v_z^2}{c_{\rm s}^2}, \tag{4.52}$$

where St is the Stokes number, and δv_z^2 is velocity dispersion. Under the minimum-mass solar nebula in a hydrodynamic equilibrium, St can be expressed as

$$\mathrm{St} = 1 \times 10^{-5} \left(\frac{a}{1\ \mu\mathrm{m}} \right) \left(\frac{r}{10\ \mathrm{AU}} \right)^{3/2} \exp\left(\frac{z^2}{2H^2} \right). \tag{4.53}$$

When the disk flow is laminar or $J < J_{\rm turb}$, even 0.1 μm sized dust grains settles on the midplane dust layer. The laminar state in e-heating zones may help formation of a dust layer and planetesimal formation there.

4.4.2 Weak Disk Turbulence Suggested by Recent Observations

Electron heating would suppress the disk turbulence in a large region, but the direct observability of our theory is still unknown. Therefore the theory might be supported with a indirect manner. If electron heating is widely effective in protoplanetary disks, the disk turbulence is expected to be weak. Unfortunately, an observation of disk turbulence requires a high spectral resolution to distinguish Keplerian velocity ($\sim 100c_{\rm s}$) and non-Keplerian velocity ($\sim 0.1c_{\rm s}$ or $\lesssim 0.01c_{\rm s}$, weak turbulence). Thus, the disk turbulence in protoplanetary disk is actually vague, but the turbulence strength has been expected to be $\alpha \sim$ 0.1–0.01 from the accretion stress allowing lifetime of the disks.

However, recent disk observations might possibly imply the weak disk turbulence. The disk around HL Tau, which is thought to be the most typical protoplanetary disk surrounding a T Tauri star (a young solar-type star), is recently observed by ALMA observatory having extremely high resolution, and then the amazing detailed figure is unveiled with the high resolution (ALMA Partnership et al., 2015). The disk has axisymmetric many rings and gaps approximately within 100 AU from the star. Because such the young system ($\leq$ 1-2 Myr; Briceño et al., 2002) is thought to be dynamic, many researchers discuss the formation mechanism. Because gas giant planets are well known to make a gap, the gaps might be formed by gas ginats. However, according to a core accretion model of classical planet formation, gas giants take time to get their envelope from the surrounding disk gas (several Myr). In addition, if each of the gaps is caved by a gas giant, planets are orderly arranged with the separation of each planets of $\sim$ 10 AU. Thus, the orbital stability has been discussed (ALMA Partnership et al., 2015). The other possibilities to explain the rings and gaps is some (gravitational) instabilities (Takahashi & Inutsuka, 2014) and dust growth with/without a planet (Zhang et al., 2015; Okuzumi et al., 2015).

It goes without saying that the gap formation mechanism is debated, but the disk properties of HL Tau are of great interest too. Pinte et al. (2016) reproduced the similar observational image with the radiative transfer simulation and obtained the dust and gas properties. According to the paper, such a clear gap requires for the disk to be geometrically thin, which means the weak turbulence ($\alpha \lesssim$ a few 10^{-4}). That is because if the disk is thick, the back of the disk should be observed. Kataoka et al. (2015) constrained the maximum dust particle size with a size distribution and obtained relatively small maximum particle size ($\sim$ 150 μm), using the dust continuum data of ALMA and the polarization data of the other observatories. Because even the maximum size of 3 mm assumed by Pinte et al. (2016) leads to $\alpha \lesssim$ a few 10^{-4}, the maximum size of Kataoka et al. (2015) should lead to much smaller α value.

Moreover, Flaherty et al. (2015) observed a disk around A-type star, HD163296, and obtained the spectral map which limits on non-thermal gas velocity dispersion, i.e. turbulence. They constraints the velocity dispersion of turbulence to be less than $\sim 0.03c_{\rm s}$ which corresponds to $\alpha \lesssim 10^{-3}$ outside $\sim$ 30 AU, from CO(3-2) transition. The value is one order of magnitude less than typical α value of fully developed MRI turbulence $\alpha \sim 10^{-2}$. However, we have to note that the observation with the transition line observe a sparse region of disks ($\lesssim 5\times10^{-3}$ g cm^{-2} or 3–5 H in their model) and the precise information of disk turbulence in a dense region has still not been obtained. In future, a observatory having higher spectral resolution will clearly reveal the turbulence distribution of the disks.

Chapter 5

Summary and Conclusion

5.1 Summary

In this work, we investigated the quantitative effect of electron heating on the MRI with MHD simulation including the increasing resistivity by the electron heating. First, we presented the zones where electron heating can suppress MRI turbulence and showed that the zones dominate large regions that have been is in a vigorous turbulent state so far. However, how much electron heating suppresses the MRI was still unknown. We perform MHD simulation to address the nonlinear evolution of MRI including the resistivity by electron heating. We introduce a simple analytic resistivity model that enables us to treat the increasing resistivity. We summarize the results as follows:

- We find an clear relation between magnetic turbulence strength and its current density in Figure 4.8 in Section 4.2. The relation means that a lower current leads to lower turbulence strength.. Thus, we confirmed the electron heating suppresses MRI turbulence when current density is well suppressed by electron heating.
- We find that when turbulence completely dies away, laminar accretion flow is caused by ordered magnetic field in Figure 4.3 in Section 4.2. The growth of magnetic field stops at the sinusoidal structure because the resistivity increases at the current sheet,
- Based on the simulation results and the scaling relation between the accretion

stress and current density, we obtain a formula that successfully predicts the accretion stress in the presence of electron heating once current density is given. In a protoplanetary disk, the current density can be estimated by using the current-dependent resistivity and the saturated resistivity. Thus, we can predict the accretion stress in extensive regions where the electron heating occur. This helps us to construct realistic planet formation theory.

This paper have revealed the importance of electron heating on the nonlinear evolution of MRI. Disk turbulence in protoplanetary disks critically impacts on the disk evolution and planet formation. A role of electron heating should be elucidated in order to construct realistic planet formation models.

In this work, we have neglected the stratified density structure. However, our results might depends on the simulation box size in a vertical direction. We have to note that these results is based just on the simple analytic J–E relation. In reality, the electron heating rises the N-shaped nonlinear Ohm's law. Of course, finally, the real effect of electron heating on MRI is investigated by considering the realistic resistivity model with a MHD simulation. However, this work first unveils the relation of Maxwell stress and current density and the state when MRI completely dies away by suppressing current density. The importance of current density in MRI is stressed. We conclude that the reliability of the suppression of MRI by electron heating has been shown by this work.

5.2 Future Work

We will address the following in future work.

Development of General Nonideal MHD Effects Amplified Electron Heating

In this study, we have neglected the all nonideal MHD effects amplified the electron heating except for the Ohmic dissipation. We will develop an applicable manner to Hall effect and ambipolar diffusion. This work is done with Satoshi Okuzumi.

Inspection of MRI Activity in Disk around HL Tau

Recently, Pinte et al. (2016) suggested weak turbulence in the disk around HL Tau. So far young disk is thought to be dynamic because of high accretion rate onto the star and free fall to the disk from the envelope. The accretion rate of the disk surrounding HL Tau was estimated 8.7×10^{-7} $\mathrm{M_\odot}$ $\mathrm{yr^{-1}}$ as an upper limit (Beck et al., 2010). This corresponds to $\alpha \sim 0.01$ at 100 AU, whereas Pinte et al. (2016) suggested $\alpha \lesssim 10^{-4}$ to reproduce the observation. This seems to be inconsistent, but we have to note that the two α parameters shows different physics. α in mass accretion rate comes from accretion stress, whereas α in Pinte et al. (2016) comes from vertical velocity dispersion. Thus, the gap of the two suggest high Schmidt number, which is a ratio of accretion viscosity to diffusion coefficient. Because our work suggested that laminar state leads to high Schmidt number (see Section 4.4.1), the laminar state of our work is good for this point.

We will first investigate the possibility that MRI in the disk is stabilized by nonideal MHD including suppression of MRI by electron hating. First, using some suggested disk profile (density, temperature and so on), we evaluate dimensionless number indicating efficiency of nonideal MHD effects. In that case, the effects includes Ohmic dissipation, Hall effect, and Ambipolar diffusion, but not include electron heating. Then, we strict the parameter (magnetic field strength, X-ray luminosity, and so on) to reproduce the weak turbulence in a whole region of HL Tau's disk. We will also evaluate the α parameter suggested from several nonideal MHD simulations. After that, we introduce the electron heating effect. Comparing the two restricted parameters with respect to accretion rate and diffusion coefficient, we will investigate the plausibilities.

Formation of Ring Structure in Disk around HL Tau

In addition to the weak turbulence has a potential to explain a formation mechanism of the ring structure. The observed ring width is approximately 10 AU. Although several formation mechanisms are proposed, there is no consensus. One possible formation mechanism is secular gravitational instability (Youdin, 2005a,b, 2011; Takahashi & Inutsuka, 2014), which is gravitational instability caused by gas friction between gas and dust. Takahashi & Inutsuka (2014) found the most unstable wavelength in the radial direction is typically 10 AU in weak turbulence. If the instability grows globally, the rings whose width is 10 AU forms.

We will investigate possibility of secular gravitational instability in disk around HL Tau. The weak turbulence has already been suggested (Pinte et al., 2016), but the distribution of turbulence strength is unknown. We calculate turbulence strength simply assuming the existence of dead zone and e-heating zone. This work will be performed with Takahashi Sanemichi.

Gravitational Instability Far from the Star

In protoplanetary disks which is one kind of accretion disks, the disk gas accretes onto the star. If the disk turbulence presents, the accretion is driven by turbulent viscosity closely related to turbulence strength. Thus, in the weak turbulence region, e.g. dead zone, accreted gas is accumulated and eventually causes gravitational instability (Sano et al., 2000; Martin & Lubow, 2011). The dead zones, where MRI is completely suppressed, lies within $\sim$ 20 AU in typical disk at early stage. Since electron heating enlarges the zone where MRI is completely or moderately suppressed, gravitational instability would occurs in a larger region. This might suggests gas giant far from the star which is formed by the gravitational instability. The formation mechanism of such gas giants is still mysterious.

We will investigate how electron heating enlarges the gravitationally unstable region. The stress–current relation presented in this work gives accretion stress in each position. Assuming the steady and gravitationally stable accretion disk driven by the Maxwell stress, we calculate dependence of accretion rate on surface density within the gravitationally unstable surface density, i.e. Toomre's gravitational unstable condition. Next, assuming a gas accretion from the outer disk by effective turbulent viscosity, we give the constant accretion rate. If the stable disk is realizable, there is a surface density realizing the constant accretion rate. In other words, if there is no surface density realizing the constant accretion rate, the disk goes unstable. We will investigate whether the disk can be stable or not at each position.

Simulation with the Real Nonlinear Ohm's Law

We will try to consider the real dependence of resistivity on E. In MHD equation system, the growth of electric field strength can not be explicitly treated. In addition, when $d\sigma/dE < 0$, electric field strength is unstable. The time scale is remarkably fast, i.e. $\sim 10^{-4}$–10^{-2} s^{-1}. Thus, the real nonlinear Ohm's law is not available without any idea.

We will develop the physically exact solution by focusing the existence of physics of more slower time. Actually, the nonlinear Ohm's law is obtained by assuming the charge equilibrium. However, in such the short time interval, the equilibrium is broken. Thus, we use typical time scale of charge reaction.

Simulation in Stratified Box

In this work, we perform MHD simulation with unstratified disk. Although density varies in the vertical direction in a hydrostatic equilibrium in reality, the unstratified disk is thought to be justified by assuming that the perturbation mode is limited in gas scale height H. Thus, if unstable mode is limited within typically scale hight even in the stratified simulation box, our results is reliable in the stratified case. However, our results would be controlled by the size of simulation box (see Figure 4.11). Thus, the our result will be modified. In order to investigate the stratified case, we will perform the similar MHD simulation again in the stratified simulation box.

Acknowledgement

First of all, I would like to express my gratitude to my advisor, Dr. Satoshi Okuzumi, for his constant encouragement and patient support since I have been thought from him. His guidance over the sea have always properly helped me in the current year. Dr. Shigeru Ida tolerantly accept me to go away from Titech as a visiting student, nevertheless he generously gives me financial support. Besides my advisors, I would like to also thank Dr. Shu-ichiro Inutsuka, Dr. Takeru Suzuki, and Dr. Hiroshi Kobayashi for their kindly accepting me as a visiting student at Nagoya University. I am grateful to Dr. Takayuki Muranushi for his kindly giving me the Athena code modified by my request and his friendly technical supports for it. I am also grateful to Dr. Neal Turner, Dr. Mario Flock and Dr. Yasuhiro Hasegawa for the very fruitful discussions and the kind support during my visiting JPL. I thank also my colleague in our laboratory, Takahiro Ueda and Yuhito Shibaike, for stimulating discussions and also my roommates in Ta laboratory of Nagoya University. Computations were performed on “maddux” at Ta laboratory of Nagoya University.

Bibliography

Adachi, I., Hayashi, C., & Nakazawa, K. 1976, Progress of Theoretical Physics, 56, 1756

ALMA Partnership, Brogan, C. L., Pérez, L. M., et al. 2015, ApJ, 808, L3

Bai, X.-N. 2014, ApJ, 791, 137

Bai, X.-N., & Goodman, J. 2009, ApJ, 701, 737

Bai, X.-N., & Stone, J. M. 2011, ApJ, 736, 144

Balbus, S. A., & Hawley, J. F. 1991, ApJ, 376, 214

Beck, T. L., Bary, J. S., & McGregor, P. J. 2010, ApJ, 722, 1360

Blaes, O. M., & Balbus, S. A. 1994, ApJ, 421, 163

Blum, J., & Wurm, G. 2008, ARA&A, 46, 21

Briceño, C., Luhman, K. L., Hartmann, L., Stauffer, J. R., & Kirkpatrick, J. D. 2002, ApJ, 580, 317

Carballido, A., Cuzzi, J. N., & Hogan, R. C. 2010, MNRAS, 405, 2339

Carballido, A., Stone, J. M., & Pringle, J. E. 2005, MNRAS, 358, 1055

Chen, F. F. 1977, INTRODUCTION TO PLASMA PHYSICS 『プラズマ物理入門』, ed. 内田岱二郎 (丸善株式会社)

Davydov, B. 1935, Sowjet.

Desch, S. J. 2004, ApJ, 608, 509

Dohnanyi, J. S. 1969, J. Geophys. Res., 74, 2531

Dzyurkevich, N., Turner, N. J., Henning, T., & Kley, W. 2013, The Astrophysical Journal, 765, 114

Ferguson, E. E. 1973, Atomic Data and Nuclear Data Tables, 12, 159

Flaherty, K. M., Hughes, A. M., Rosenfeld, K. A., et al. 2015, ApJ, 813, 99

Fleming, T., & Stone, J. M. 2003, ApJ, 585, 908

Flock, M., Dzyurkevich, N., Klahr, H., Turner, N. J., & Henning, T. 2011, ApJ, 735, 122

Fromang, S., & Nelson, R. P. 2006, A&A, 457, 343

Fromang, S., & Papaloizou, J. 2006, A&A, 452, 751

Gammie, C. F. 1996, ApJ, 457, 355

Ganguli, B., Biondi, M. A., Johnsen, R., & Dulaney, J. L. 1988, Phys. Rev. A, 37, 2543

Glassgold, A. E., Najita, J., & Igea, J. 1997, ApJ, 480, 344

Golant, V. E., Zhilinsky, A. P., & Sakharov, I. E. 1980, Fundamentals of plasma physics (Wiley New York)

Goldreich, P., & Ward, W. R. 1973, ApJ, 183, 1051

Gressel, O., Nelson, R. P., & Turner, N. J. 2011, MNRAS, 415, 3291

Hawley, J. F., Gammie, C. F., & Balbus, S. A. 1995, ApJ, 440, 742

Hawley, J. F., & Stone, J. M. 1998, ApJ, 501, 758

Hayashi, C. 1981, Progress of Theoretical Physics Supplement, 70, 35

Hershey, A. V. 1939, Physical Review, 56, 916

Inutsuka, S., & Sano, T. 2005, ApJ, 628, L155

Johansen, A. 2009, Lecture notes on the magnetorotational instability

Kataoka, A., Muto, T., Momose, M., Tsukagoshi, T., & Dullemond, C. P. 2015, ArXiv e-prints, arXiv:1507.08902

Kataoka, A., Muto, T., Momose, M., et al. 2015, 1504.04812

Kunz, M. W., & Balbus, S. A. 2004, MNRAS, 348, 355

Landau, L. D., & Lifshitz, E. M. 1953, Physical Kinetics (New York: Pergamon)

Lesur, G., Kunz, M. W., & Fromang, S. 2014, A&A, 566, A56

Lifshitz, E. M., & Pitaevskii, L. P. 1981, Physical Kinetics (Pergamon Press)

Martin, R. G., & Lubow, S. H. 2011, ApJ, 740, L6

Mathis, J. S., Rumpl, W., & Nordsieck, K. H. 1977, ApJ, 217, 425

Matthews, L. S., Land, V., & Hyde, T. W. 2012, ApJ, 744, 8

Mayor, M., & Queloz, D. 1995, Nature, 378, 355

Miller, K. A., & Stone, J. M. 2000, ApJ, 534, 398

Mori, S., & Okuzumi, S. 2016, ApJ, 817, 52

Muranushi, T., Okuzumi, S., & Inutsuka, S. 2012, ApJ, 760, 56

Nakano, T., Nishi, R., & Umebayashi, T. 2002, ApJ, 573, 199

Nakano, T., & Umebayashi, T. 1986, MNRAS, 218, 663

Natta, A., Testi, L., Neri, R., Shepherd, D. S., & Wilner, D. J. 2004, A&A, 416, 179

Okuzumi, S. 2009, ApJ, 698, 1122

Okuzumi, S., & Hirose, S. 2011, ApJ, 742, 65

Okuzumi, S., & Inutsuka, S. 2015, ApJ, 800, 47

Okuzumi, S., Momose, M., Sirono, S., Kobayashi, H., & Tanaka, H. 2015, ArXiv e-prints, arXiv:1510.03556

Okuzumi, S., Tanaka, H., & Sakagami, M. 2009, ApJ, 707, 1247

Okuzumi, S., Tanaka, H., Takeuchi, T., & Sakagami, M. 2011, ApJ, 731, 96

Ormel, C. W., & Cuzzi, J. N. 2007, A&A, 466, 413

Pinte, C., Dent, W. R. F., Ménard, F., et al. 2016, ApJ, 816, 25

Ricci, L., Testi, L., Natta, A., et al. 2010, A&A, 512, A15

Rodmann, J., Henning, T., Chandler, C. J., Mundy, L. G., & Wilner, D. J. 2006, A&A, 446, 211

Safronov, V. S. 1969, Evolution of the protoplanetary cloud and formation of the earth and planets.

Salmeron, R., & Wardle, M. 2003, MNRAS, 345, 992

Sano, T., Inutsuka, S., Turner, N. J., & Stone, J. M. 2004, ApJ, 605, 321

Sano, T., & Miyama, S. M. 1999, ApJ, 515, 776

Sano, T., Miyama, S. M., Umebayashi, T., & Nakano, T. 2000, ApJ, 543, 486

Shukla, P. K., & Mamun, A. A. 2002, Introduction to Dusty Plasma Physics (Institute of Physics Publishing Ltd., Bristol)

Simon, J. B., Bai, X.-N., Armitage, P. J., Stone, J. M., & Beckwith, K. 2013a, ApJ, 775, 73

Simon, J. B., Bai, X.-N., Stone, J. M., Armitage, P. J., & Beckwith, K. 2013b, ApJ, 764, 66

Simon, J. B., Hawley, J. F., & Beckwith, K. 2009, ApJ, 690, 974

Spitzer, Jr., L. 1941, ApJ, 93, 369

Suzuki, T. K., Muto, T., & Inutsuka, S. 2010, ApJ, 718, 1289

Takahashi, S. Z., & Inutsuka, S. 2014, ApJ, 794, 55

Testi, L., Natta, A., Shepherd, D. S., & Wilner, D. J. 2003, A&A, 403, 323

Turner, N. J., Carballido, A., & Sano, T. 2010, ApJ, 708, 188

Turner, N. J., Fromang, S., Gammie, C., et al. 2014, Protostars and Planets VI, 411

Turner, N. J., & Sano, T. 2008, ApJ, 679, L131

Turner, N. J., Sano, T., & Dziourkevitch, N. 2007, ApJ, 659, 729

Umebayashi, T. 1983, Progress of Theoretical Physics, 69, 480

Umebayashi, T., & Nakano, T. 1981, PASJ, 33, 617

—. 1990, MNRAS, 243, 103

—. 2009, ApJ, 690, 69

Velikhov, E. P. 1959, JETP

Wadehra, J. M. 1984, Phys. Rev. A, 29, 106

Wannier, G. H. 1953, Bell System Technical Journal, 32, 170

Wardle, M. 1999, MNRAS, 307, 849

Wardle, M., & Ng, C. 1999, MNRAS, 303, 239

Wardle, M., & Salmeron, R. 2012, MNRAS, 422, 2737

Weidenschilling, S. J. 1977, MNRAS, 180, 57

—. 1984, Icarus, 60, 553

Weidenschilling, S. J., & Cuzzi, J. N. 1993, in Protostars and Planets III, ed. E. H. Levy & J. I. Lunine, 1031–1060

Wolk, S. J., Harnden, Jr., F. R., Flaccomio, E., et al. 2005, ApJS, 160, 423

Yoon, J.-S., Song, M.-Y., Han, J.-M., et al. 2008, Journal of Physical and Chemical Reference Data, 37, 913

Youdin, A. N. 2005a, ArXiv Astrophysics e-prints, astro-ph/0508659

—. 2005b, ArXiv Astrophysics e-prints, astro-ph/0508662

—. 2011, ApJ, 731, 99

Youdin, A. N., & Lithwick, Y. 2007, Icarus, 192, 588

Zhang, K., Blake, G. A., & Bergin, E. A. 2015, ApJ, 806, L7

Zsom, A., Ormel, C. W., Güttler, C., Blum, J., & Dullemond, C. P. 2010, A&A, 513, A57

Appendix A

Appendix

A.1 Time Evolution of Simulation Results

We enumerate results of section 4.2 with respect to time-dependent value.

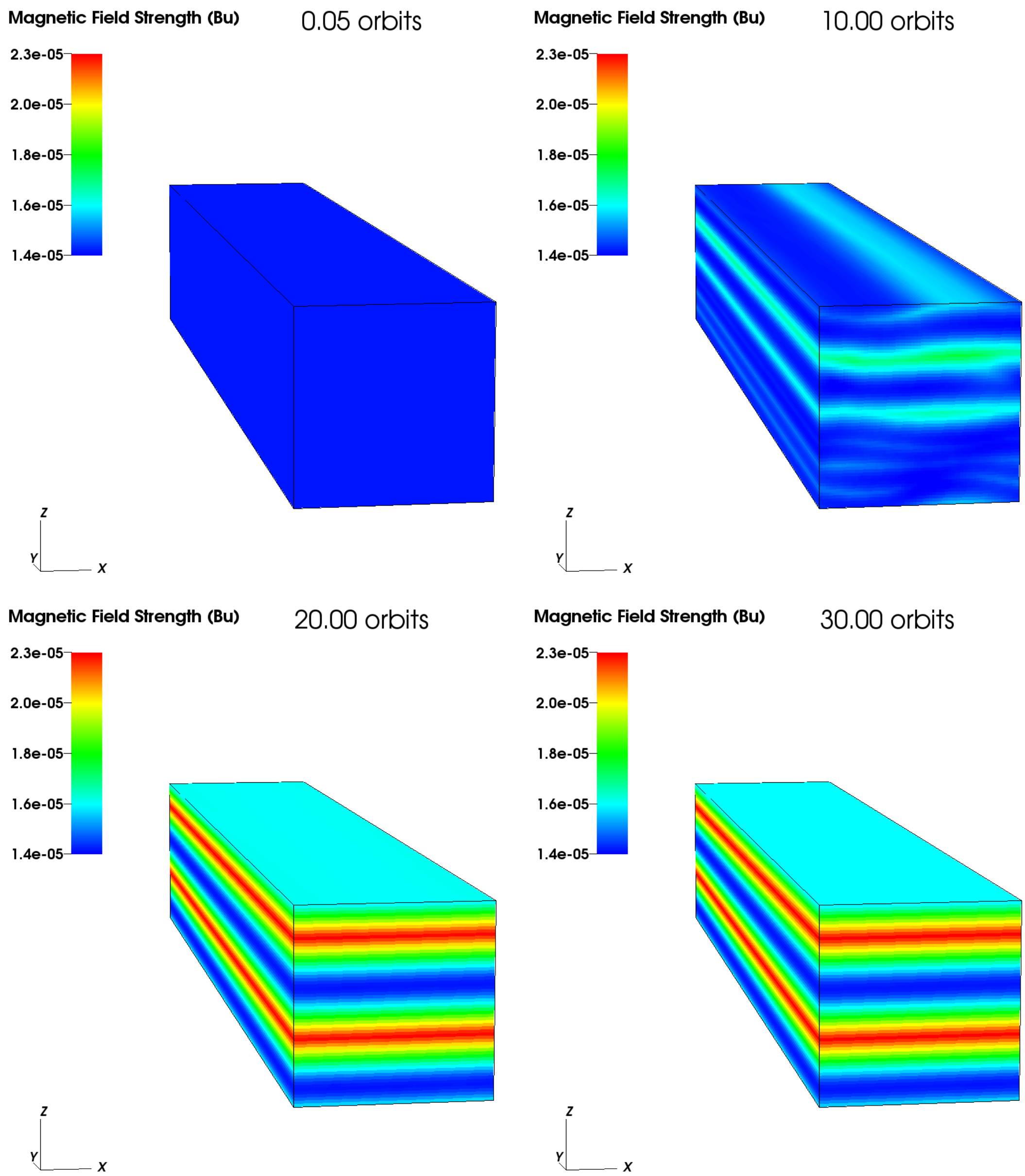

Figure A.1: Time evolution of magnetic field strength in the case of $J_{\mathrm{EH}}/J_{\mathrm{u}} = 0.03$. Each panel shows time, $t = 0$ (upper left), 10 (upper right), 20 (lower left), and 30 (lower right) orbits. The colors shows the magnetic fields strength $|\boldsymbol{B}|$ normalized by the maximum value.

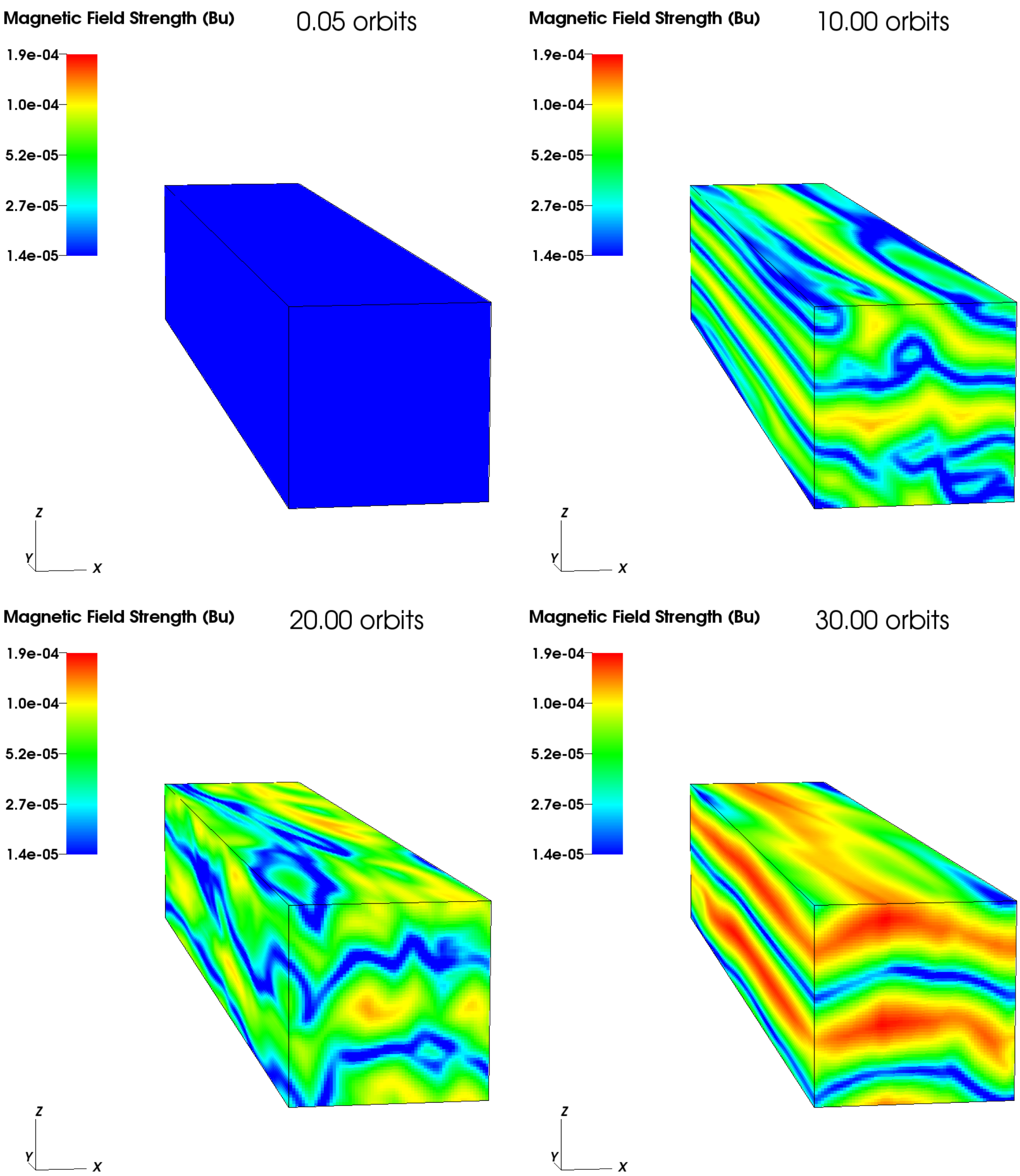

Figure A.2: Same as Figure A.1, but in the case of $J_{\rm EH}/J_{\rm u} = 0.3$.

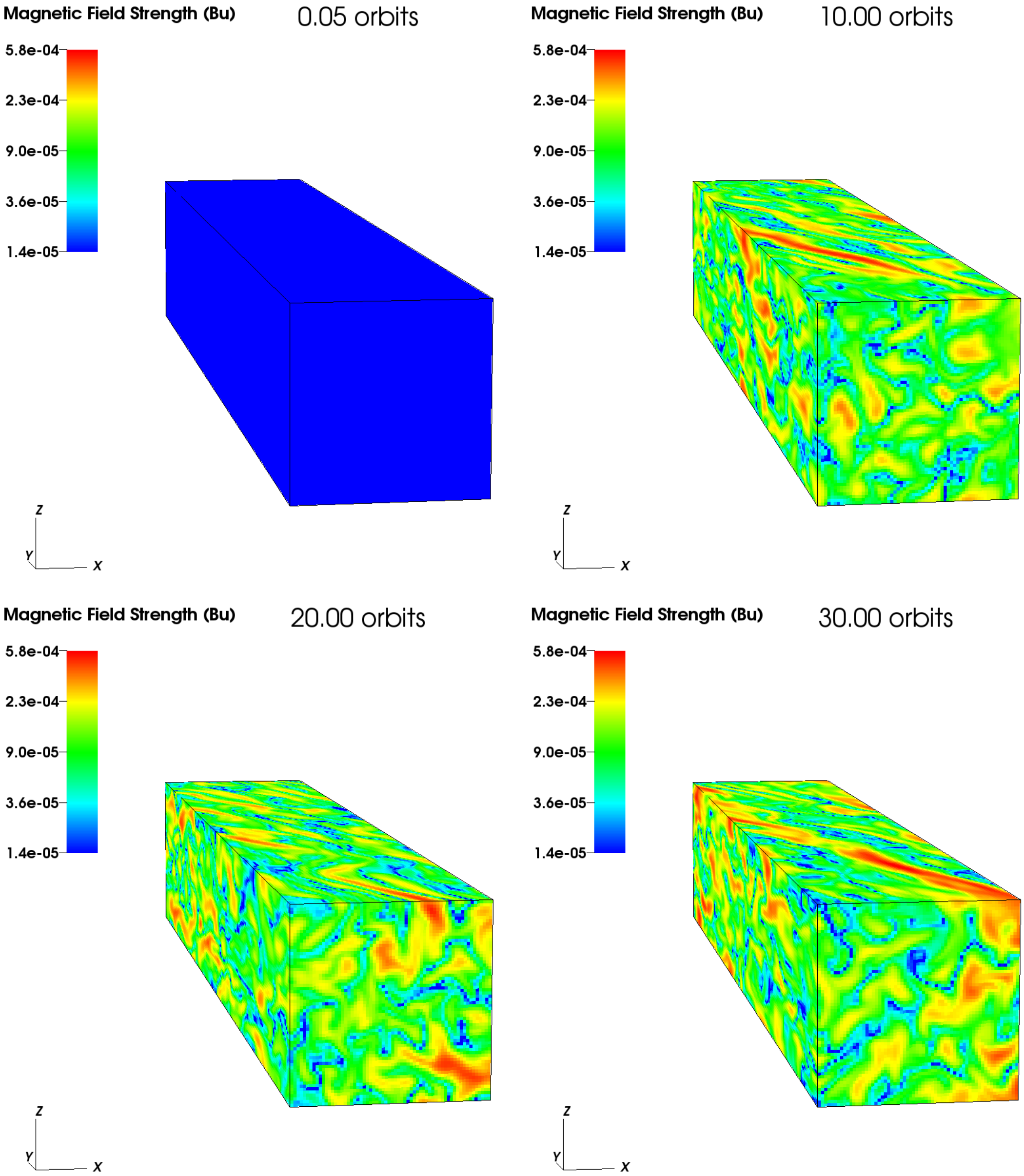

Figure A.3: Same as Figure A.1, but in the case of $J_{\mathrm{EH}}/J_{\mathrm{u}} = 3$.

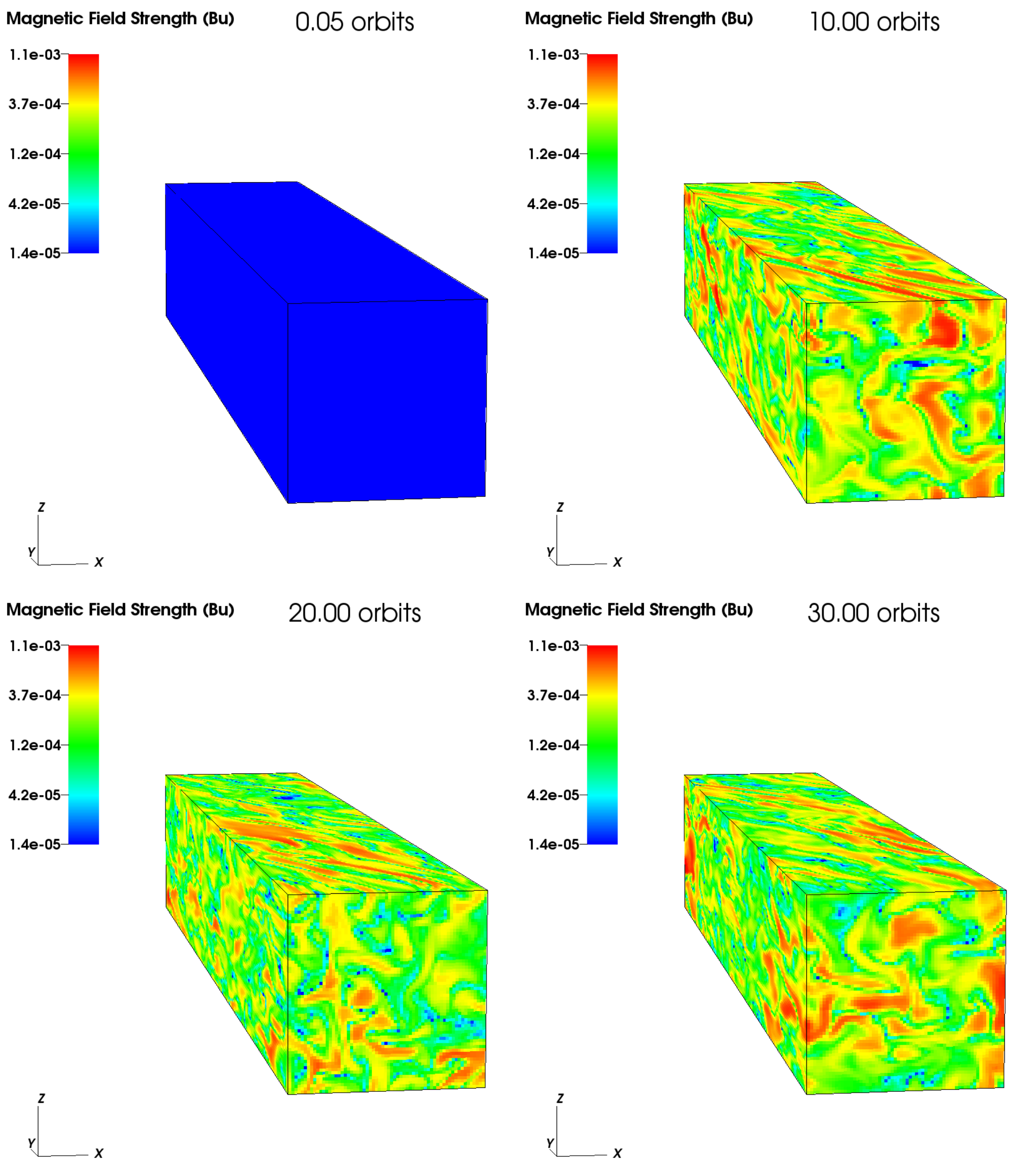

Figure A.4: Same as Figure A.1, but in the ideal MHD case.

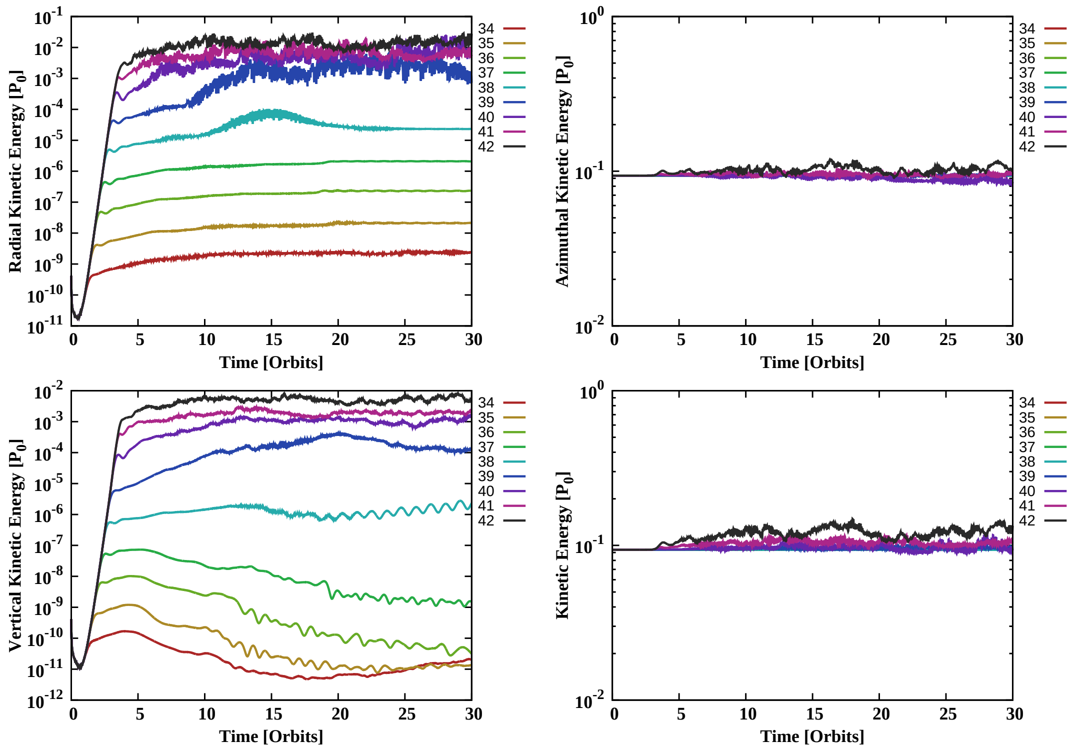

Figure A.5: Time-evolution of kinetic energy in x (upper left), y (upper right), z (lower left) and the total (lower right) direction. The colors show computational ID which means difference of J_{EH}.

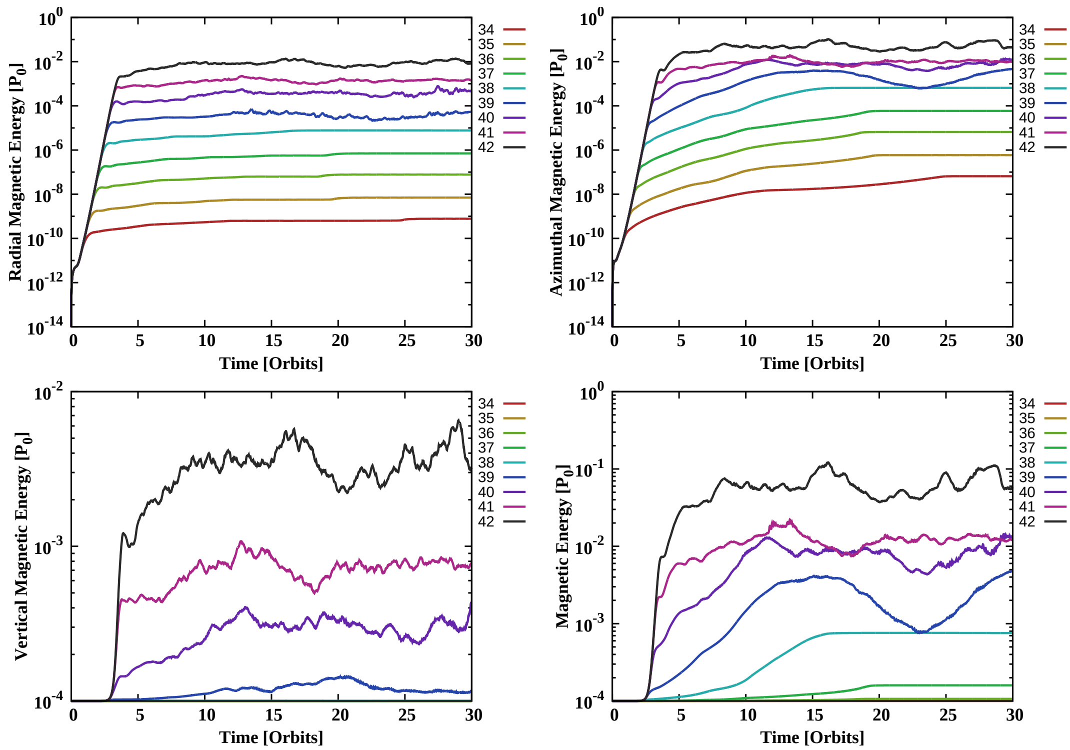

Figure A.6: Time-evolution of kinetic energy in x (upper left), y (upper right), z (lower left) and the total (lower right) direction. The colors show computational ID which means difference of J_{EH}.

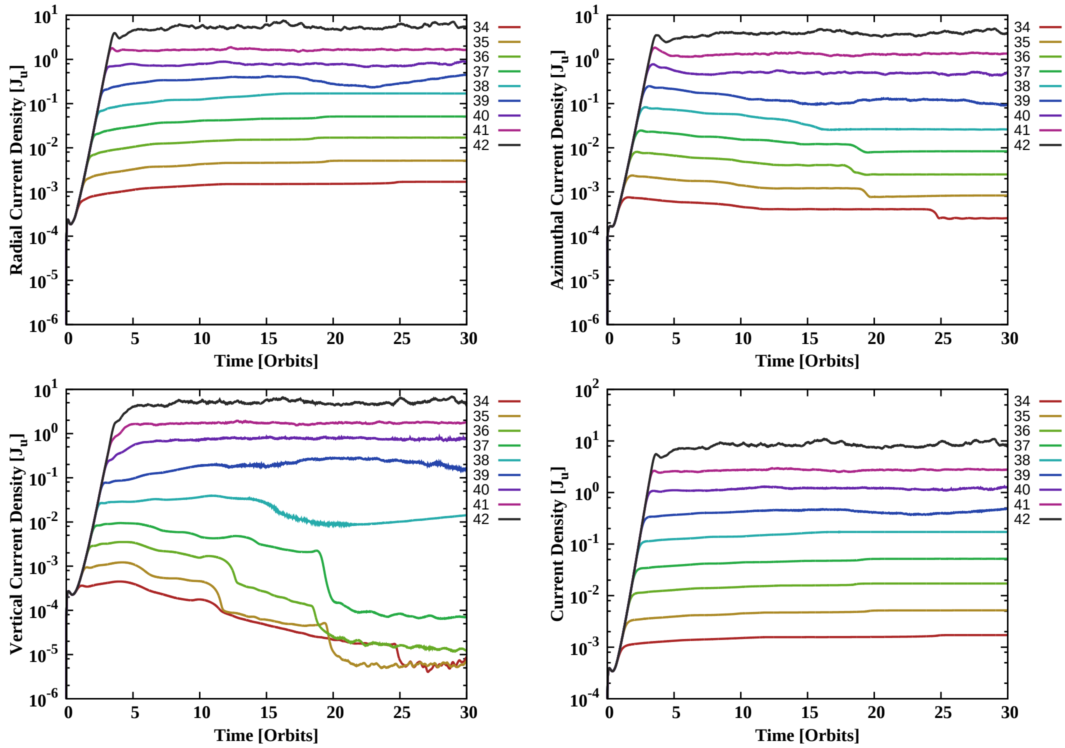

Figure A.7: Time-evolution of current density in x (upper left), y (upper right), z (lower left) and the total (lower right) direction. The colors show computational ID which means difference of J_{EH}.

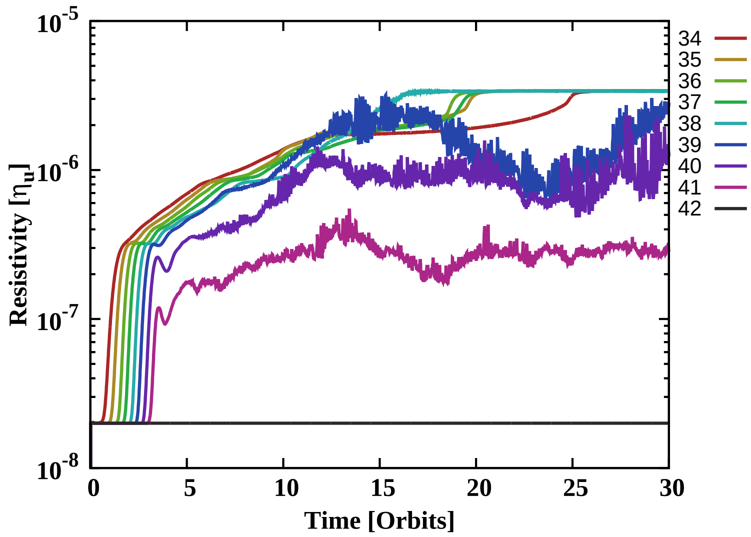

Figure A.8: Time variation of η. The colors shows the same as Figure A.5.

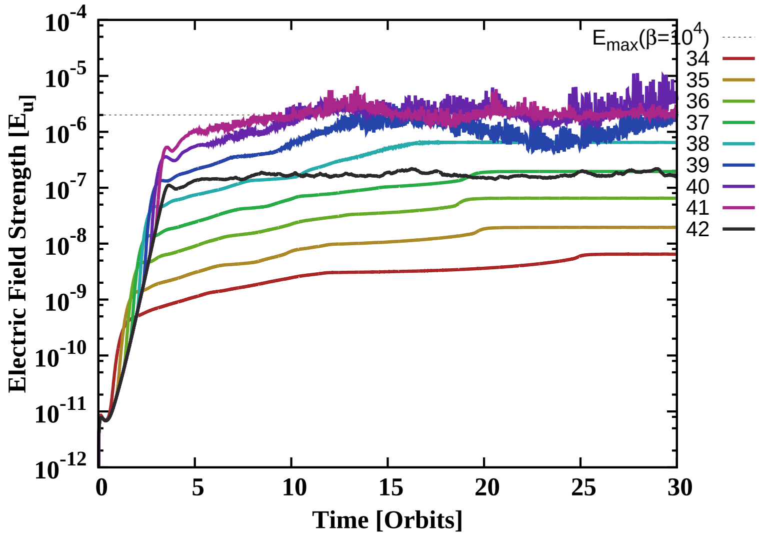

Figure A.9: Time variation of E. The colors shows the same as Figure A.5.

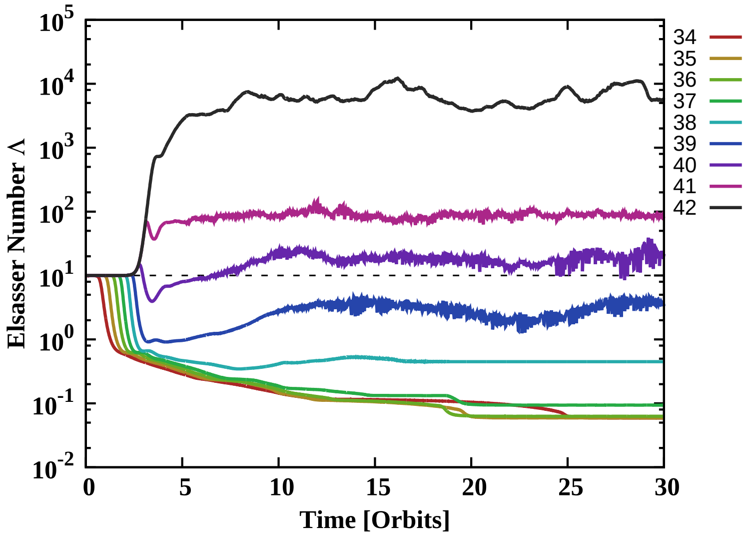

Figure A.10: Time variation of Λ. The colors shows the same as Figure A.5.

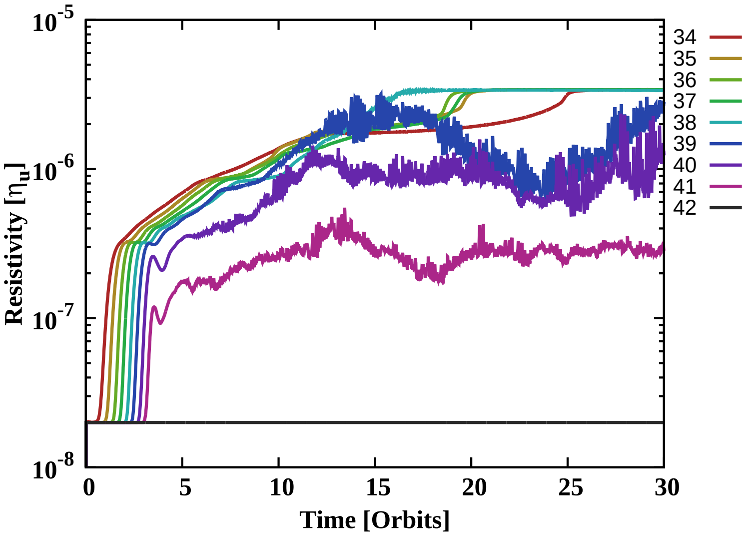

Figure A.11: Time variation of η. The colors shows the same as Figure A.5